BHAVSAR, K. 2016. *Investigations on the development of a novel hybrid sensor for environmental monitoring applications*. Robert Gordon University, PhD thesis. Hosted on OpenAIR [online]. Available from: https://doi.org/10.48526/rgu-wt-1677500

Investigations on the development of a novel hybrid sensor for environmental monitoring applications.

BHAVSAR, K.

2016

INVESTIGATIONS ON THE DEVELOPMENT OF A NOVEL HYBRID SENSOR FOR ENVIRONMENTAL MONITORING APPLICATIONS

KAUSHALKUMAR BHAVSAR

A thesis submitted in partial fulfilment of the
requirements of the
Robert Gordon University
for the degree of Doctor of Philosophy

June 2016

Declaration

I hereby declare that no portion of the work reported in this thesis has been submitted for the award of any other degree or qualification of this or other university.

This thesis has been compiled by the author.

Acknowledgement

I would like to thank my supervisors Dr Radhakrishna Prabhu and Prof Pat Pollard for their encouragement, guidance and valuable support during this work. Many thanks to Carlos, Morgan, Vivek, Emma, Duncan, administration staff and many other people from the school of Engineering for their support. I would also, like to thank the technicians Andy Ross and David Smith for their support. Very special thanks to my family for all their love, support and encouragement and finally, my heartiest “Pranam” to “Lord Shree Swaminarayan” for his blessings.

Publications

Papers Published

- **K. Bhavsar**, D. Ross, R. Prabhu and P. Pollard, LED controlled tuning of ZnO nanowires wettability for biosensing applications, Nano Reviews. 6 (2015) 26711
- **K. Bhavsar**, R. Prabhu and P. Pollard, Ultrasensitive graphene coated SPR sensor for biosensing applications, Proceedings of SPIE. 9506 (2015) 95060U
- **K. Bhavsar**, R. Prabhu and P. Pollard, Investigations on surface wettability of ZnO nanowires using UV LEDs for biosensing applications, IOP Conference Series: Materials Science and Engineering. 64 (2014) 012033
- **K. Bhavsar**, R. Prabhu and P. Pollard, Development of dithizone based fibre optic evanescent wave sensor for heavy metal ion detection in aqueous environments, Journal of Physics: Conference Series. 450 (2013) 012011

Conference/Symposium/Workshop

- **K. Bhavsar** and R. Prabhu, Large Size Free-Standing ZnO Nanowire Films for Multifunctional Applications, 2nd International Conference on Material Science and Technology (ICMST2016), Arunapuram, Kerala, India, Jun 5-8, 2016
- **K. Bhavsar**, E. Hourston, B. C. Mathews, P. Radhakrishnan and R. Prabhu, Development of U-bend Optical Probe to Detect Heavy Metal Ions, 4th EOS Topical Meeting on Blue Photonics - Optics in the Sea (Blue Photonics 4), Barcelona, Spain, May 11-13, 2015
- **K. Bhavsar** and R. Prabhu, Effect of wavelength and graphene layers on the SPR sensitivity, OWTNM 2015, London, UK, Apr 17-18, 2015
- **K. Bhavsar**, B. C. Mathews, R. Prabhu, P. Pollard and P. Radhakrishnan, U-bend based fibre optic evanescent wave sensor to detect copper ions using dithizone, Photon14, London, UK, Sep 1-4, 2014
- **K. Bhavsar**, R. Prabhu and P. Pollard, Investigations on surface wettability of ZnO nanowires using UV LEDs for biosensing applications, Nanostuc2014, Madrid, Spain, May 20-21, 2014
- **K. Bhavsar**, R. Prabhu and P. Pollard, ZnO nanowire hydrophobic-hydrophilic switch using UV light LEDs, ICAFM 2014, Thiruvananthapuram, Kerala, India, Feb 19-21, 2014
- **K. Bhavsar**, R. Prabhu and P. Pollard, Development of dithizone based fibre optic evanescent wave sensor for heavy metal ion detection in aqueous

environments, Sensors & their Applications XVII, Dubrovnik, Croatia, Sep 16-18, 2013

- **K. Bhavsar**, R. Prabhu and P. Pollard, Optical fibre based heavy metal ion sensor for monitoring crude oil contaminated wastewater, 4th Technical Meeting of Optoelectronic Technologies for the Oil and Gas Industry, Aberdeen, UK, Jun 6, 2013
- **K. Bhavsar**, R. Prabhu and P. Pollard, Optical fibre based mercury sensor for environmental monitoring applications, Fifth Scottish Postgraduate Symposium on Environmental Analytical Chemistry, Aberdeen, UK, Dec 18, 2012

Other Published Papers / Conference

- B. C. Mathews, **K. Bhavsar**, T. Thevar, P. Radhakrishnan and R. Prabhu, Preliminary investigations on materials/metal structures using laser induced breakdown spectroscopy (LIBS) for underwater structural health monitoring, 2nd International Conference on Material Science and Technology (ICMST2016), Arunapuram, Kerala, India, Jun 5-8, 2016
- B. C. Mathews, T. M. Libish, **K. Bhavsar**, V. Viswambaran, R. Prabhu and P. Radhakrishnan, A fiber optic biosensor for the detection of cholesterol levels based on chitosan coated long period grating, Optoelectronics Letters. 12 (2016), 23
- R. S. Sreedharan, V. Ganesan, C. P. Sudarsanakumar, **K. Bhavsar**, R. Prabhu et al., Highly textured and transparent RF sputtered Eu_2O_3 doped ZnO films, Nano Reviews. 6 (2015) 26759

Abstract

Heavy metal toxicity is a major environmental problem world-wide. Increased spreading and high concentration levels of the toxic heavy metals in water environments have posed a severe threat to human health and the ecosystem. Over the years, to improve the drinking water quality standards, safe threshold concentrations of these highly toxic pollutants are constantly being lowered by the governmental and environmental bodies. Current instrumental techniques used to detect these low levels of heavy metal ions are laboratory based, use sophisticated instruments, expensive, time consuming and require trained personnel. There is a constant need for the development of in-situ, rapid, highly sensitive and selective sensors to monitor the very low concentration levels. Various approaches for improving sensitivity and selectivity have been investigated over the years involving multiple detection techniques. In general, optical approaches provide higher sensitivity along with simplicity while electrochemical sensors provide better selectivity. In the last decade, nanomaterials have emerged as a key element in their sensitivity improvement. Combining all these advantages, a novel hybrid sensor has been envisaged integrating optical and electrical fields in addition to nanomaterials. This thesis reports investigations on enhancing the sensitivity/selectivity through optical, nanomaterials and electrochemical routes, and then integrating these to realise a hybrid sensor.

A novel optical sensor has been developed using the phenomena of evanescent waves in optical fibre with dithizone to detect heavy metal ions. A U-bent sensor geometry has been investigated to enhance the optical sensitivity of the sensor through higher evanescent field near the surface. Further, optical field confinement to the surface has been investigated through thin film coating to improve the sensitivity. A new inverted trench design based sensor has been developed, and sensitivity enhancement has been achieved through this novel design and confirmed using modelling work accompanied by experimental results.

Large surface to volume ratio of nanomaterials, such as ZnO nanowires, on the sensor surface can provide enhanced surface interactions leading to higher sensitivity. But, surfaces modified with ZnO nanostructures tend to be hydrophobic in nature. A new remote and non-contact method to tune the wettability of the ZnO nanostructures using LEDs has been developed. Higher sensitivity has been achieved by tuning the wettability of ZnO nanowires using the developed method.

Electrochemical sensor has been developed in order to understand the potential effects of the electric field on the near surface molecular dynamics and thereby, effects on the optical detection. Effects of parameters such as deposition time, scan frequency, concentration, electrode materials and their surface area have been investigated to improve the sensitivity and selectivity. Multi-ions selectivity has been achieved by simultaneous detection of copper, mercury and lead ions in buffer solution. Higher sensitivity has been obtained by modifying the gold electrode using graphene flakes.

Further, to integrate the optical field with this sensor to realize the hybrid sensor, thickness of the gold electrode has been optimised to allow the penetration of evanescent field onto the electrode surface. Under optimised conditions evanescent field resonantly couples to the surface plasmons of the gold electrode. Computational investigations have been carried out to study the effect of number of graphene layers on the sensitivity of the surface plasmon resonance (SPR) based optical sensor integrated with the electrochemical sensor. Preliminary investigations on the developed hybrid sensor show that the electric field complements the optical field. Investigations have shown that application of electric field enhances the sensitivity for optical detection by attracting more ions on the electrode and also, provides the multi-ion selectivity. These investigations have opened up new possibilities for the real-time monitoring of highly sensitive and selective molecular interactions, showing strong potential in a range of applications areas such as environmental sensing, biosensing and agricultural sensing.

Keywords: Fibre Optic Sensor, Surface Plasmon Resonance, Electrochemical Sensor, Heavy Metal ions, Graphene, Gold, ZnO nanowires, Wettability

Contents

List of abbreviations

2D	Two Dimensional
AAS	Atomic Absorption Spectroscopy
AFM	Atomic Force Microscopy
AFS	Atomic Fluorescence Spectrometry
ASR	Analyte Specific Reagent
ASV	Anodic Stripping Voltammetry
BF	Bare Silica Fibre
CV	Cyclic Voltammetry
DAQ	Data Acquisition System
EDX	Energy Dispersive X-Ray Spectroscopy
EM	Electromagnetic
EPA	Environmental Protection Agency
FRET	Fluorescence Resonance Energy Transfer
FWHM	Full Width Half Maximum
GC	Glassy Carbon
GNP	Gold Nanoparticles
HCF	Hard Clad Silica Fibre
HOMO	Highest Occupied Molecular Orbital
ICP-OES	Inductively Coupled Plasma Optical Emission Spectrometry
ITF	Inverted Trench Silica Fibre
LA-ICP-MS	Laser Ablation Inductively Coupled Plasma Mass Spectroscopy
LED	Light Emitting Diode

LOD	Limit Of Detection
LUMO	Lowest Unoccupied Molecular Orbital
MCL	Maximum Contaminant Level
NP	Nanoparticles
NSET	Nanometal Surface Energy Transfer
PCA	Principle Component Analysis
PPM	Parts per Million
QCM	Quartz Crystal Microbalance
SEM	Scanning Electron Microscopy
SERS	Surface Enhanced Raman Scattering
SPFS	Surface Plasmon field enhanced Fluorescence Spectroscopy
SPLS	Surface Plasmon field enhanced Light Scattering
SPP	Surface Plasmon Polariton
SPR	Surface Plasmon Resonance
SPRS	Surface Plasmon Resonance Spectroscopy
TEM	Transmission Electron Microscopy
TIR	Total Internal Reflection
UV	Ultraviolet
WCA	Water Contact Angle
WHO	World Health Organization

List of Figures

List of Tables

Chapter 1

Introduction

1 Introduction

1.1 Overview

Today, the maintenance and enhancement of conditions that will enable humans and other organisms to exist on earth, is the biggest challenge faced by humankind. Therefore, there is a need to monitor the quality of living environments and the influence of their activities thereon. This can be achieved through gathering information of various parameters and substances in the environment and the process is referred to as environmental monitoring. The emphasis in the environmental monitoring is to assess the level of harmful and potentially harmful substances/pollutants, their effects on humans and living organisms and their discharges in the environment.

There are several ways to classify the environmental pollutants based on their source, phase, toxicity and geographical availability [1]. Analysis of these pollutants depends on the factors such as their physical and chemical properties, temporal and spatial distribution, and environmental conditions. Broadly, environmental pollutants can be classified into atmospheric pollutants (such as sulphur dioxide, nitrogen oxides, carbon monoxide, trace metals, particulate matter, organic compounds, photochemical oxidants etc.), water pollutants (such as heavy metals, metalloids, volatile organic compounds, biological pollutants etc.) and soil pollutants such as (pesticides, heavy metals, petroleum hydrocarbons, chemicals etc.) [1-3]. Among all these pollutants, heavy metal ions form an important group of pollutants which can be found in air, water and soil.

1.2 Heavy Metal ions and Their Toxicity

Heavy metals are any metallic chemical element with a relatively high density and are found as natural components of the Earth’s crust. Heavy metals ions are non-biodegradable, have very low water solubility and tendency to accumulate in living organisms [4]. Some heavy metals such as mercury, copper, cadmium, lead, chromium, nickel, arsenic have severe harmful effects on humans and the ecosystem because of their toxicity [5]. Mercury can cause severe damage to brain, heart, kidney, lung, immune system and neurological system [6]. Lead can cause severe harmful effects on liver, brain, reproductive system, kidney and central nervous system. These toxic heavy metal ions are primary elements and hence cannot be destroyed. These heavy metal ions enter into the environment through direct or indirect discharge of industrial and consumer waste, mining operations, fossil fuels combustion and volcanoes [1,7]. Therefore, heavy metal ion pollution emerges as a serious environmental problem today due to their toxicity, volatility and mobility [8].

1.3 Overview on Heavy Metal ions Detection Techniques

Environmental and governmental bodies across the world set the limit of highest level of contaminants, referred to as maximum contaminant level (MCL), allowed in public water systems by enforcing strict laws and regulatory standards. Over the years, these limits of contaminant concentration levels of many environmental pollutants including heavy metal ions in drinking water have been lowered by United States Environmental Protection Agency (EPA) and World Health Organization (WHO) to protect public health [9,10].

Current instrumental techniques used to detect heavy metal ions includes laser ablation inductively coupled plasma mass spectrometry (LA-ICP-MS) [11], atomic fluorescence spectrometry (AFS) [12], inductively coupled plasma optical emission spectrometry (ICP-OES) [13] and atomic absorption spectroscopy (AAS) [14]. These techniques require laboratory-based highly sophisticated instruments and trained personnel to carry out the sample analysis. Although, these techniques are very sensitive and selective, they are time consuming and expensive. Considering the cost, time and efforts involved in evaluating the realistic information from the environmental samples, an obvious need exists for the development of in-situ, portable, rapid, highly sensitive and selective, and easy to use field sensors.

Over the years many heavy metal ion sensors have been developed for in situ application using different techniques. These sensors can be broadly divided into two categories such as optical sensors and electrochemical (EC) sensors based on the signal transduction mechanisms. The following section presents a very brief overview of optical and electrochemical sensors used to detect heavy metal ions.

1.3.1 Optical Sensors

1.3.1.1 Colorimetric and Fluorescent Sensors

Colorimetric sensors can be sub-classified based on the reagent used to detect the heavy metal ions such as calixarene-based, small molecule based, polymer based, DNA-based, nanoparticle based chemosensors [15-17]. Among these sensors especially nanoparticles based colorimetric sensor have reported higher sensitivity [15,16]. Surface plasmons of the metal nanoparticles are extremely sensitive to the surrounding environment and to the surface binding and adsorption events. An aggregation of nanoparticles induced by any such events cause the change in surface plasmon absorption band. This in turn leads to the change in the colour of the solution and therefore, forms the basis of colorimetric detection. Colorimetric sensors provide rapid, direct visual detection of various metal ions [15,18,19].

A basis of fluorescent based sensors is to detect the change in physiochemical properties of fluorophores induced by heavy metal ions. This can be in the form of fluorescent intensity or lifetime change and attributed to the charge transfer or energy transfer processes. Among the fluorescent sensors for heavy metal ions, fluorescence resonance energy transfer (FRET) based sensors are of prime focus for the researchers [20-22]. FRET is the mechanism of energy transfer between two molecules upon interaction with light. The process of FRET can be described as an excited donor molecule transfers the excitation energy to the acceptor molecule through the dipole-dipole interaction without emission of the photon. As stated, the process occurs through dipole-dipole coupling, it depends on the inverse sixth power of distance ($1/d^6$) between the molecules [20,23,24]. FRET requires the spectral overlap between the emission band of a donor molecule and the absorption band of acceptor molecule [21]. Gold nanoparticles (GNPs) are excellent quencher over broad wavelength range and in fluorophore-quencher based sensors, energy transfer strongly depends on the plasmonic nature of the GNPs [25,26]. If the GNPs show SPR, energy transfer mechanism follows the FRET effect and if no SPR, energy transfer mechanism follows the nanometal surface energy transfer (NSET) effect [25,27]. The NSET process occurs over a longer separation distance $1/d^4$, compared to the FRET effect [28].

DNA is a negatively charged biomolecule and, therefore, has a tendency to bind with the positively charged metal ions. A group of families developed from the combination of DNA and enzymes, referred to as DNAzymes, possesses catalytic activities. These DNAzymes offer several advantages such as inexpensive to produce, high specificity to metal ions, wide selection range, higher resistance to the hydrolysis process. Therefore, DNA and DNAzymes based biosensors are becoming attractive for metal ion detection applications [29]. DNA-based Hg^{2+} sensor has been developed by Ono [30] using FRET effect, where the binding of Hg^{2+} enables the FRET process amongst the quencher and fluorophore. The developed sensor has achieved a 40 nM detection limit for Hg^{2+} in buffer solution. Another candidate for fluorophore-quencher based sensors is graphene oxide (GO). Graphene oxide is also excellent fluorescence quencher. It is also, water soluble, inexpensive and easy to functionalize with various functional groups [22,31-34]. Recently, very few papers have reported fluorescent sensors for heavy metal ions using graphene/graphene oxide [35,36].

1.3.1.2 Surface Plasmon Resonance (SPR) Sensors

A surface plasmon is the collective oscillation of free electrons in the metal surface or in other words, it is a propagating electron density waves at the metal-dielectric interface and is very sensitive to the surrounding environment. In the past two decades, SPR has evolved as an optical tool to probe the molecular level interactions in real time. It has been used to investigate the physical, chemical and biological activities at the interface region. More than a decade ago, heavy metal ions detection using SPR has emerged. Wu and Lin have developed SPR sensor using metallothionein to detect cadmium (Cd), zinc (Zn) or nickel (Ni). The sensor has achieved a detection limit of less than 2μM within a small range but suffers from interfering metal ions and pH [37]. Moon et al. [38] have carried out the in situ adsorption study of Pt^{2+} using SPR spectroscopy. Their findings have revealed the role of wettability of the surface on adsorption property of metal ions using SPR. Their experimental results have indicated that the hydrophilic surface increases the adsorption rate of the metal ions on the surface. A problem with the SPR technique is to distinguish between the change in dielectric constant and thickness of the layer, change in refractive index of buffer solution and adsorption of metal ions and other interfering species [39]. Furthermore, SPR technique is not suitable to detect small molecules, especially metal ions because the SPR response is not sufficient to recognize them. The difference in refractive index of metal ions is very small and therefore, it is very hard to differentiate them [40]. Therefore, approaches where metal ion specific chromophores (such as calixarene and dithizone) have been attached on the SPR substrate which leads to enhanced SPR response have been reported [41,42].

1.3.1.3 Surface Enhanced Raman Scattering (SERS) Sensors

Raman scattering process occurs through the inelastic collision of photons with molecules and is a very weak effect. However, if the process takes place on the surface of metal nanoparticles, resonance between surface plasmons and optical fields leads to enhanced Raman scattering signal and is referred as surface-enhanced Raman scattering effect (SERS) [43,44]. SERS spectroscopy is a powerful technique to probe the biomolecular interactions at single molecule level and has been extensively exploited in the field of biosensing and medical diagnostics [45]. Although, SERS is a molecular level spectroscopy, it is unable to provide the signal for the heavy metal ions, unless the metallic particles are modified with the specific binding ligands [46]. Therefore, there are very few papers reported for heavy metal ion detection using SERS [47-50].

1.3.2 Electrochemical Sensors

Heavy metal ions have defined oxidation and reduction potentials. Therefore, even a bare electrode can provide the selective detection of heavy metal ions without the need of a recognition agent or surface modifications. Several electrochemical sensing methods have been used to detect heavy metal ions, including potentiometry, voltammetry, amperometry, impedemetry [51]. In particular, anodic stripping voltammetry (ASV) is the popular technique used for sensitive and selective detection of heavy metal ions [52-56]. However, the technique has several limitations such as the necessity of buffer solution and electro active species, problem of background currents and electroplating of the surface. Also, EC sensors are unable to detect intermetallic compounds.

Unique electronic properties and a large surface to volume ratio of nanomaterials such as carbon nanotubes, graphene and metal/metal oxide nanoparticles make them attractive for electrochemical sensing applications [57,58]. Nanomaterial modified electrode gives enhanced surface area and fast electron transfer rate compared to the bulk electrode materials. Therefore, electrodes modified with nanomaterials have shown increased sensitivity and lower detection limits towards the heavy metal ion detection [59].

1.4 Scope of Improvement

For the environmental monitoring applications, it is important to have information such as ionic state of the heavy metals and association with organic compounds because the chemical, biological and physical responses of these metals will vary based on their physio-chemical conditions [60]. For example, chromium (III) is an essential trace element, while chromium (VI) is carcinogenic [5]. Hg(0), Hg(II) and methyl mercury (CH_3Hg) have different temporal and spatial scales of transport, lifetime and toxicity [8]. Therefore, multiple analysis techniques/sensors have been used in the field to get additional information as stated. A hybrid sensor which includes multiple detection techniques can simplify this analysis process, reduce the time and costs involved and provide realistic information in the field. In general, optical approaches provide higher sensitivity along with simplicity while electrochemical sensors provide better selectivity. In the last decade, nanomaterials have emerged as a key element in their sensitivity improvement.

There are several novel approaches being developed over the time in order to improve the sensitivity and selectivity of the existing techniques and to gain more insight into the detection/monitoring/reaction of the species by interrogating their different properties simultaneously. These approaches are based on combining multiple/hybrid sensing techniques to utilize their advantages and try to overcome the respective drawbacks as discussed in section 1.3.

Analysis of co-polymerization behaviour between terthiophene and a carbazole moiety has been carried out by combining electrochemical quartz crystal microbalance (EC-QCM) techniques and electrochemical surface plasmon resonance spectroscopy (EC-SPR). Each technique represents the unique aspect of interaction going on between the species and therefore, provides more insight into reaction among them in a single measurement [61]. Glucose detection has been carried out using N-alkylaminated polypyrrole/glucose oxidase multi-layers, by combining electrochemical surface plasmon resonance (EC-SPRS) technique [39]. Electropolymerization of aniline and then the doping-dedoping process of polyaniline film have been investigated by Baba et al. [62]. Investigations have been carried out by combining surface plasmon resonance spectroscopy (SPRS) and surface plasmon field-enhanced light scattering (SPLS) with electrochemical (EC) method [62]. The reaction of hydroquinone-benzoquinone and their intermediate products have been studied by combining electrochemical surface plasmon resonance spectroscopy (EC-SPRS) [63]. Movement of fluorophore labelled antibody has been studied by combining surface plasmon resonance (SPR) and surface plasmon field-enhanced fluorescence spectroscopy (SPFS) [64]. In situ optical, electrochemical and morphological studies of the conjugated polymer electropolymerization process have been reported by Baba et al. [65] using a novel combined electrochemical, surface plasmon resonance spectroscopy and atomic force microscopy (EC-SPRS-AFM).

Among all such novel approaches the combination of electrochemistry and the surface plasmon resonance have emerged as an exciting development for characterizing surface interactions and sensing applications. Application of this technique has been well exploited in the field of biosensing, but limited in the field of environmental sensing, especially on heavy metal ions. There are very few reports on heavy metal detection using such hybrid techniques and has a huge potential for environmental monitoring applications [42,66,67]. Panta et al. [68] have developed Hg^{2+} sensor combining the SPR and electrochemical sensing techniques. They have reported sensitivity enhancement by incorporating the magneto hydrodynamic convection along with the SPR and ASV. Robert et al. [69] have reported ion adsorption study by simultaneous electrical and plasmonic monitoring of applied potential. Mirkhalaf and Schiffrin have developed metal ion sensor combining SPR and anodic stripping voltammetry and studied the effect of applied potential on the SPR response in situ [42].

A hybrid EC-SPR technique offers several advantages in detecting heavy metal ions. Electrochemical sensing in combination with the SPR acts as a complementary to enhance the response time, to improve detection limit and to regenerate the sensor surface. Also, it provides the additional information about the ionic state of the metal ions which is necessary for the environmental applications. Intermetallic compounds can also, be detected using SPR but not with ASV [42,66,67].

In this work, various investigations on the development of a novel hybrid sensor to detect heavy metal ions which combine the integrated effect of optical, electric field and surface modified with nanomaterials to achieve higher sensitivity and selectivity have been carried out. The hybrid sensor mainly consists of three layers as shown in Figure 1.1. The optical layer not only allows optical detection for a suitable approach, but also facilitates an interface with the second material layer. The second layer consists of thin coating of conductive/semi-conductive materials to perform the electrochemical detection. The third layer includes a coating of suitable nanomaterials such as graphene and ZnO to further enhance the sensitivity by utilizing their special structural, electrical and optical properties. The coating includes nanomaterial or composite nanomaterials and may be used for immobilization of absorption or fluorescence based analyte specific reagents (ASR).

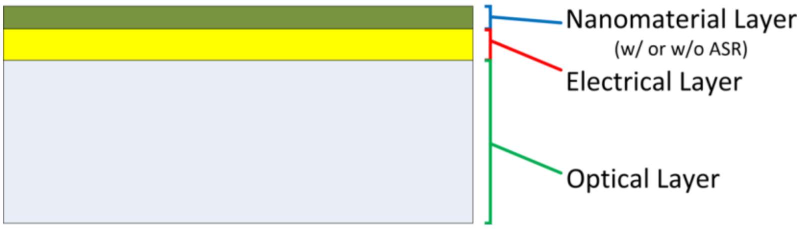

Figure 1.1 A schematic of the layered design of hybrid sensor.

Figure 1.2 shows the schematic representation of the research work carried out and various investigations in order to develop the novel hybrid sensor.

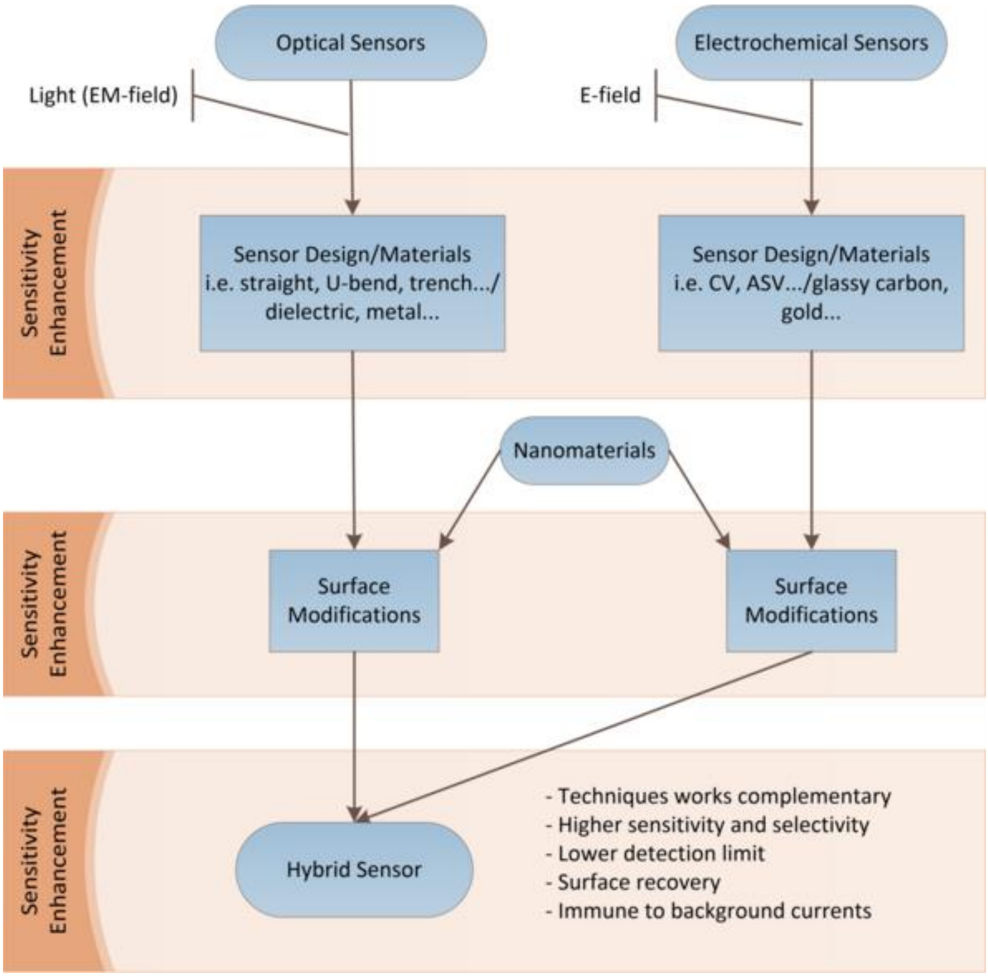

Figure 1.2 A schematic of the research work to investigate various parameters on the development of a novel hybrid sensor.

1.5 Summary

The discussion in this chapter has provided the need for the development of a novel hybrid sensor to detect heavy metal ions for environmental monitoring applications. Various optical detection approaches to detect heavy metal ions including chromophore-based, fluorophore-based, surface plasmon resonance based, surface enhanced Raman spectroscopy based have been discussed and the limitations have been identified. Electrochemical sensors for heavy metal ions have been discussed and the problems associated with the anodic stripping voltammetry have been identified. A scope for sensitivity and selectivity improvement through the development of a novel hybrid sensor has been presented.

1.6 Research Aim and Objectives

This thesis aims to report various investigations on enhancing the sensitivity/selectivity through optical, nanomaterials and electrochemical routes, and then integrating these to realise a hybrid sensor. This goal is further divided into separate objectives as follows:

- Identification of suitable chromophore and fluorophore for the detection of heavy metal ions and their interaction study
- Synthesis of suitable materials for the development of sensor surface.
- Development of absorption and fluorescence-based sensors to detect heavy metal ions
- Develop an optical sensor using suitable approach, and investigate effect of various environmental parameters, materials parameters and sensor design configurations to enhance the sensitivity and selectivity
- Surface modifications using nanomaterials to improve the sensitivity and investigate the effects of surface modifications on sensitivity
- Investigate the effect of the electric field in the near surface region by the development of electrochemical sensor and investigations of various parameters to achieve higher sensitivity and selectivity
- Investigate the development of integrated hybrid sensing combining optical and electrical detection along with surface modification with nanomaterials, and various parameters to enhance the sensitivity

1.7 Thesis Organisation

The thesis consists of seven chapters with detailed results and discussion on the set objectives of the research work. Chapter 1 gives an overview of the research work, scope and objectives of the research work. A very brief review on environmental monitoring and the necessity for monitoring concentration levels of heavy metal ions in water, review on existing methods and sensors have been included. The chapter summarises with the objectives and methodology of the research work to be carried out.

Chapter 2 includes the investigations on materials suitable for developing the hybrid sensor. Absorption and fluorescence based approaches for the detection of heavy metal ions and their interactions with dithizone and rhodamine B have been investigated. Synthesis of materials and coatings has been presented, various parameters have been analysed and their effects on properties of the material have been discussed.

Chapter 3 includes the various investigations on optical sensor development. Optical fibre based sensor have been developed based on evanescent waves to detect heavy metal ions in water. Investigations have been carried out to study the effect of factors such as pH, concentration range, optical fibre parameters, and geometrical configuration of the fibre. Various parameters have been evaluated using modelling and experimental work in order to enhance the sensitivity. The possibility of multi-ion detection has been demonstrated through multi-ion detection experiment. A novel inverted trench configuration has been developed to enhance the sensitivity of the developed evanescent wave sensor.

In order to enhance the sensitivity using nanomaterials and for developing the required sensor surface, various investigations have been carried out, and are discussed in chapter 4. Surface modification with ZnO nanostructures, gold thin films and graphene have been carried out. Wettability tuning using LEDs has been carried out and control parameters have been identified in order to enhance the sensitivity.

Chapter 5 reports investigations on the development of electrochemical sensor for heavy metal ions detection. Techniques such as cyclic voltammetry and anodic stripping voltammetry have been investigated. Parameters such as electrode materials and their surface area, buffer solution, deposition time, scan rate and scan frequency have been investigated in terms of their probable effects on the optical sensing. Multi-ions selectivity has been exploited through simultaneous detection of mercury, copper and lead ions. Sensitivity enhancement has been carried out through surface modification using graphene. Developed electrochemical sensor has been exploited to integrate the optical detection in order to develop the novel hybrid sensor. The hybrid sensor has been developed and various investigations on the development have been discussed in chapter 6. A study on various parameters affecting the sensitivity has been carried out and their optimization has been carried out through computational work. Investigations have been carried out using experimental and theoretical work and initial results on the hybrid sensing have been discussed.

1.8 References

[1] S. Manahan, Fundamentals of Environmental Chemistry, 3rd ed., CRC Press, New York, 2008.

[2] R.M. Harrison, Understanding our Environment - an Introduction to Environmental Chemistry and Pollution, 3rd ed., Royal Society of Chemistry, Cambridge, 1999.

[3] J. Namiesnik, Trends in environmental analytics and monitoring, Crit. Rev. Anal. Chem. 30 (2000) 221-269.

[4] A. Tessier, D.R. Turner, Metal Speciation and Bioavailability in Aquatic Systems, John Wiley & Sons, Chichester, 1995.

[5] B.A. Fowler, G.F. Nordberg, M. Nordberg, L. Friberg, Handbook on the Toxicology of Metals, 3rd ed., Academic Press, San Diego, 2007.

[6] P.B. Tchounwou, W.K. Ayensu, N. Ninashvili, D. Sutton, Environmental exposure to mercury and its toxicopathologic implications for public health, Environ. Toxicol. 18 (2003) 149-175.

[7] F. Fu, Q. Wang, Removal of heavy metal ions from wastewaters: A review, J. Environ. Manage. 92 (2011) 407-418.

[8] C.T. Driscoll, R.P. Mason, H.M. Chan, D.J. Jacob, N. Pirrone, Mercury as a global pollutant: Sources, pathways, and effects, Environ. Sci. Technol. 47 (2013) 4967-4983.

[9] World Health Organization, Guidelines for drinking-water quality, 2015 (2011) 564.

[10] United States Environmental Protection Agency, Drinking Water Contaminants – Standards and Regulations, 2015 (2015).

[11] M. Legrand, R. Lam, M. Jensen-Fontaine, E.D. Salin, H.M. Chan, Direct detection of mercury in single human hair strands by laser ablation inductively

coupled plasma mass spectrometry (LA-ICP-MS), J. Anal. At. Spectrom. 19 (2004) 1287-1288.

[12] D. Sanchez-Rodas, W.T. Corns, B. Chen, P.B. Stockwell, Atomic Fluorescence Spectrometry: a suitable detection technique in speciation studies for arsenic, selenium, antimony and mercury, J. Anal. At. Spectrom. 25 (2010) 933-946.

[13] X. Wu, W. Yang, M. Liu, X. Hou, C. Zheng, Vapor generation in dielectric barrier discharge for sensitive detection of mercury by inductively coupled plasma optical emission spectrometry, J. Anal. At. Spectrom. 26 (2011) 1204-1209.

[14] R. Puk, J.H. Weber, Determination of Mercury(ii), Monomethylmercury Cation, Dimethylmercury and Diethylmercury by Hydride Generation, Cryogenic Trapping and Atomic-Absorption Spectrometric Detection, Anal. Chim. Acta. 292 (1994) 175-183.

[15] H.N. Kim, W.X. Ren, J.S. Kim, J. Yoon, Fluorescent and colorimetric sensors for detection of lead, cadmium, and mercury ions, Chem. Soc. Rev. 41 (2012) 3210-3244.

[16] Y. Hung, T. Hsiung, Y. Chen, Y. Huang, C. Huang, Colorimetric Detection of Heavy Metal Ions Using Label-Free Gold Nanoparticles and Alkanethiols, Journal of Physical Chemistry C. 114 (2010) 16329-16334.

[17] M. Benounis, N. Jaffrezic-Renault, H. Halouani, R. Lamartine, I. Dumazet-Bonnamour, Detection of heavy metals by an optical fiber sensor with a sensitive cladding including a new chromogenic calix[4]arene molecule, Mat. Sci. Eng. C-Bio. S. 26 (2006) 364-368.

[18] X. Xu, W.L. Daniel, W. Wei, C.A. Mirkin, Colorimetric Cu2+ Detection Using DNA-Modified Gold-Nanoparticle Aggregates as Probes and Click Chemistry, Small. 6 (2010) 623-626.

[19] Y.J. Kim, R.C. Johnson, J.T. Hupp, Gold nanoparticle-based sensing of "spectroscopically silent" heavy metal ions, Nano Letters. 1 (2001) 165-167.

[20] B. Liu, F. Zeng, Y. Liu, S. Wu, A FRET system built on quartz plate as a ratiometric fluorescence sensor for mercury ions in water, Analyst. 137 (2012) 1698-1705.

[21] R. Roy, S. Hohng, T. Ha, A practical guide to single-molecule FRET, Nature Methods. 5 (2008) 507-516.

[22] J.S. Lee, H. Joung, M. Kim, C.B. Park, Graphene-Based Chemiluminescence Resonance Energy Transfer for Homogeneous Immunoassay, ACS Nano. 6 (2012) 2978-2983.

[23] D.J. Zhou, J.D. Piper, C. Abell, D. Klenerman, D.J. Kang, L.M. Ying, Fluorescence resonance energy transfer between a quantum dot donor and a dye acceptor attached to DNA, Chemical Communications. (2005) 4807-4809.

[24] E.A. Jares-Erijman, T.M. Jovin, FRET imaging, Nat. Biotechnol. 21 (2003) 1387-1395.

[25] M. Li, S.K. Cushing, Q. Wang, X. Shi, L.A. Hornak, Z. Hong, N. Wu, Size-Dependent Energy Transfer between CdSe/ZnS Quantum Dots and Gold Nanoparticles, Journal of Physical Chemistry Letters. 2 (2011) 2125-2129.

[26] B.N.J. Persson, N.D. Lang, Electron-Hole-Pair Quenching of Excited-States Near a Metal, Physical Review B. 26 (1982) 5409-5415.

[27] C.S. Yun, A. Javier, T. Jennings, M. Fisher, S. Hira, S. Peterson, B. Hopkins, N.O. Reich, G.F. Strouse, Nanometal surface energy transfer in optical rulers, breaking the FRET barrier, J. Am. Chem. Soc. 127 (2005) 3115-3119.

[28] T.L. Jennings, M.P. Singh, G.F. Strouse, Fluorescent lifetime quenching near d=1.5 nm gold nanoparticles: Probing NSET validity, J. Am. Chem. Soc. 128 (2006) 5462-5467.

[29] X. Zhang, R. Kong, Y. Lu, Metal Ion Sensors Based on DNAzymes and Related DNA Molecules, Annual Review of Analytical Chemistry, Vol 4. 4 (2011) 105-128.

[30] A. Ono, H. Togashi, Highly selective oligonucleotide-based sensor for mercury(II) in aqueous solutions, Angewandte Chemie-International Edition. 43 (2004) 4300-4302.

[31] T. Kuila, S. Bose, A.K. Mishra, P. Khanra, N.H. Kim, J.H. Lee, Chemical functionalization of graphene and its applications, Progress in Materials Science. 57 (2012) 1061-1105.

[32] Y. Zhu, S. Murali, W. Cai, X. Li, J.W. Suk, J.R. Potts, R.S. Ruoff, Graphene and Graphene Oxide: Synthesis, Properties, and Applications, Adv Mater. 22 (2010) 3906-3924.

[33] W. Choi, I. Lahiri, R. Seelaboyina, Y.S. Kang, Synthesis of Graphene and Its Applications: A Review, Critical Reviews in Solid State and Materials Sciences. 35 (2010) 52-71.

[34] Q. Bao, K.P. Loh, Graphene Photonics, Plasmonics, and Broadband Optoelectronic Devices, ACS Nano. 6 (2012) 3677-3694.

[35] M. Li, X. Zhou, S. Guo, N. Wu, Detection of lead (II) with a "turn-on" fluorescent biosensor based on energy transfer from CdSe/ZnS quantum dots to graphene oxide, Biosens. Bioelectron. 43 (2013) 69-74.

[36] Y. Wen, F. Xing, S. He, S. Song, L. Wang, Y. Long, D. Li, C. Fan, A graphene-based fluorescent nanoprobe for silver(I) ions detection by using graphene oxide and a silver-specific oligonucleotide, Chemical Communications. 46 (2010) 2596-2598.

[37] C.M. Wu, L.Y. Lin, Immobilization of metallothionein as a sensitive biosensor chip for the detection of metal ions by surface plasmon resonance, Biosens. Bioelectron. 20 (2004) 864-871.

[38] J. Moon, T. Kang, S. Oh, S. Hong, J. Yi, In situ sensing of metal ion adsorption to a thiolated surface using surface plasmon resonance spectroscopy, J. Colloid Interface Sci. 298 (2006) 543-549.

[39] A. Baba, P. Taranekar, R.R. Ponnapati, W. Knoll, R.C. Advincula, Electrochemical Surface Plasmon Resonance and Waveguide-Enhanced Glucose Biosensing with N-Alkylaminated Polypyrrole/Glucose Oxidase Multilayers, ACS Applied Materials & Interfaces. 2 (2010) 2347-2354.

[40] S. Chah, J. Yi, R.N. Zare, Surface plasmon resonance analysis of aqueous mercuric ions, Sensors Actuators B: Chem. 99 (2004) 216-222.

[41] Z. Wang, Q.Y. Zheng, Y. Chen, Detection of metal ions using a wavelength interrogation surface plasmon resonance sensor with calix[4]arene derivatives as sensing films, Anal. Lett. 34 (2001) 2609-2619.

[42] F. Mirkhalaf, D.J. Schiffrin, Metal-ion sensing by surface plasmon resonance on film electrodes, J Electroanal Chem. 484 (2000) 182-188.

[43] K. Kneipp, Y. Wang, H. Kneipp, L.T. Perelman, I. Itzkan, R. Dasari, M.S. Feld, Single molecule detection using surface-enhanced Raman scattering (SERS), Phys. Rev. Lett. 78 (1997) 1667-1670.

[44] M. Kerker, D.S. Wang, H. Chew, Surface Enhanced Raman-Scattering (SERS) by Molecules Adsorbed at Spherical-Particles, Appl. Opt. 19 (1980) 4159-4174.

[45] J. Kneipp, H. Kneipp, K. Kneipp, SERS - a single-molecule and nanoscale tool for bioanalytics, Chem. Soc. Rev. 37 (2008) 1052-1060.

[46] M. Li, H. Gou, I. Al-Ogaidi, N. Wu, Nanostructured Sensors for Detection of Heavy Metals: A Review, ACS Sustainable Chemistry & Engineering. 1 (2013) 713-723.

[47] K. Carron, K. Mullen, M. Lanouette, H. Angersbach, Selective-Ultratrace Detection of Metal-Ions with SERS, Appl. Spectrosc. 45 (1991) 420-423.

[48] X. Ding, L. Kong, J. Wang, F. Fang, D. Li, J. Liu, Highly Sensitive SERS Detection of Hg2+ Ions in Aqueous Media Using Gold Nanoparticles/Graphene Heterojunctions, ACS Applied Materials & Interfaces. 5 (2013) 7072-7078.

[49] Y. Ye, H. Liu, L. Yang, J. Liu, Sensitive and selective SERS probe for trivalent chromium detection using citrate attached gold nanoparticles, Nanoscale. 4 (2012) 6442-6448.

[50] V.M. Zamarion, R.A. Timm, K. Araki, H.E. Toma, Ultrasensitive SERS nanoprobes for hazardous metal ions based on trimercaptotriazine-modified gold nanoparticles, Inorg. Chem. 47 (2008) 2934-2936.

[51] M.D. Tutulea, I. Cretescu, D. Sibiescu, C. Stan, Electrochemical Sensors for Heavy Metal Ions Detection from Aqueous Solutions, Environmental Engineering and Management Journal. 11 (2012) 463-470.

[52] A. Afkhami, T. Madrakian, S.J. Sabounchei, M. Rezaei, S. Samiee, M. Pourshahbaz, Construction of a modified carbon paste electrode for the highly selective simultaneous electrochemical determination of trace amounts of mercury(II) and cadmium(II), Sensor Actuat. B-Chem. 161 (2012) 542-548.

[53] X.H. Gao, W.Z. Wei, L. Yang, T.J. Yin, Y. Wang, Simultaneous determination of lead, copper, and mercury free from macromolecule contaminants by square wave stripping voltammetry, Anal. Lett. 38 (2005) 2327-2343.

[54] B. Ogorevc, X.H. Cai, I. Grabec, Determination of Traces of Copper by Anodic-Stripping Voltammetry After its Preconcentration Via an Ion-Exchange Route at Carbon-Paste Electrodes Modified with Vermiculite, Anal. Chim. Acta. 305 (1995) 176-182.

[55] E. Saito, E.F. Antunes, H. Zanin, F.R. Marciano, A.O. Lobo, V.J. Trava-Airoldi, E.J. Corat, Oxygen Plasma Exfoliated Vertically-Aligned Carbon Nanotubes as Electrodes for Ultrasensitive Stripping Detection of Pb2+, J. Electrochem. Soc. 161 (2014) H321-H325.

[56] O. Abollino, A. Giacomino, M. Malandrino, G. Piscionieri, E. Mentasti, Determination of mercury by anodic stripping voltammetry with a gold nanoparticle-modified glassy carbon electrode, Electroanalysis. 20 (2008) 75-83.

[57] M. Govindhan, B. Adhikari, A. Chen, Nanomaterials-based electrochemical detection of chemical contaminants, RSC Advances. 4 (2014) 63741-63760.

[58] S. Su, W. Wu, J. Gao, J. Lu, C. Fan, Nanomaterials-based sensors for applications in environmental monitoring, Journal of Materials Chemistry. 22 (2012) 18101-18110.

[59] G. Aragay, A. Merkoci, Nanomaterials application in electrochemical detection of heavy metals, Electrochim. Acta. 84 (2012) 49-61.

[60] R. Bogue, Environmental sensing: strategies, technologies and applications, Sens Rev. 28 (2008) 275-282.

[61] E. Simsek, Improving Tuning Range and Sensitivity of Localized SPR Sensors With Graphene, IEEE Photonics Technology Letters. 25 (2013) 867-870.

[62] A. Baba, R.C. Advincula, W. Knoll, In situ investigations on the electrochemical polymerization and properties of polyaniline thin films by surface plasmon optical techniques, J Phys Chem B. 106 (2002) 1581-1587.

[63] X. Huang, S. Wang, X. Shan, X. Chang, N. Tao, Flow-through Electrochemical Surface Plasmon Resonance Detection of intermediate reaction products, J Electroanal Chem. 649 (2010) 37-41.

[64] S. Ekgasit, F. Yu, W. Knoll, Displacement of molecules near a metal surface as seen by an SPR-SPFS biosensor, Langmuir. 21 (2005) 4077-4082.

[65] A. Baba, W. Knoll, R. Advincula, Simultaneous in situ electrochemical, surface plasmon optical, and atomic force microscopy measurements: Investigation of conjugated polymer electropolymerization, Rev. Sci. Instrum. 77 (2006) 064101.

[66] S. Wang, E.S. Forzani, N. Tao, Detection of heavy metal ions in water by high-resolution surface plasmon resonance spectroscopy combined with anodic stripping voltammetry, Anal. Chem. 79 (2007) 4427-4432.

[67] E.S. Forzani, H.Q. Zhang, W. Chen, N.J. Tao, Detection of heavy metal ions in drinking water using a high-resolution differential surface plasmon resonance sensor, Environ. Sci. Technol. 39 (2005) 1257-1262.

[68] Y.M. Panta, J. Liu, M.A. Cheney, S.W. Joo, S. Qian, Ultrasensitive detection of mercury (II) ions using electrochemical surface plasmon resonance with magneto hydrodynamic convection, J. Colloid Interface Sci. 333 (2009) 485-490.

[69] R. MacKenzie, C. Fraschina, B. Dielacher, T. Sannomiya, A.B. Dahlin, J. Voeroes, Simultaneous electrical and plasmonic monitoring of potential induced ion adsorption on metal nanowire arrays, Nanoscale. 5 (2013) 4966-4975.

Chapter 2

Materials, Synthesis and Characterization

2 Materials, Synthesis and Characterization

2.1 Introduction

Detection of any gas molecules, biomolecules, or any other chemical species depends on their interaction with the molecules/atoms present on the sensor surface and therefore, chemical and physical properties of the surfaces become very important in sensor designs. Nanomaterials such as carbon nanotubes, graphene, metal and metal oxide nanostructures are the most favourable for the new generations of sensors with "bottom-up" approach. Their simple and scalable synthesis, dispersion properties in common solvents (i.e. methanol, ethanol, isopropanol), size and shape dependent special electrical and optical properties, density of states, high aspect ratio (of nanowire and CNT) and high surface to volume ratio makes them a candidate of research [1]. Despite their different characteristics, their structures are still closely related to their parent bulk material which enables the prediction of their electrical and optical properties. These unique properties make them highly suitable candidates for sensing applications. Sensors based on these nanomaterials are emerging as a powerful tool for ultrasensitive detection of chemical and biological species [2-4]. As discussed in chapter 1, this chapter presents investigations on selection of materials, their synthesis process, and characterizing their interactions with suitable heavy metal ion receptors for the development of the hybrid sensor. Absorption and fluorescence-based detection methods have been used to detect heavy metal ions based on suitable chromophore and fluorophore. Various interactions among the selected chromophore, fluorophore with metal ions have been analysed using absorption and fluorescence spectroscopy, respectively.

Gold is a biocompatible and chemically stable metal used in various areas of physics, chemistry, pharmacy, biology for a wide range of applications. Gold nanoparticles, first synthesized more than 150 years ago, have been extensively researched to enhance their applicability in diverse fields, especially in sensing applications [5-9]. Unique electronic and optical properties of gold nanoparticles have been explored in a range of areas in last few decades [10-12]. Gold nanoparticles enhance the sensitivity of electrochemical sensors by increasing the surface area of the electrode [6,8]. Several papers on gold nanoparticle modified electrodes for sensing drug such as Fluorouracil [13], bacteria such as Escherichia coli O157:H7 [14], heavy metal ions such as mercury, lead and copper [15,16] have been reported. Gold nanoparticles have been used in various optical sensing applications based on surface plasmon resonance [17-19] and fluorescence resonance energy transfer [20-22]. Different nanostructures of gold can be created with low-cost chemical reduction method [23-25]. Therefore, gold has been identified as suitable material for the development of proposed sensor based on its compatibility with optical and electrochemical sensing methods. Simple electroless chemical reduction method [26] has been utilized to develop gold nanoparticles and gold thin films which will be elaborated in the synthesis section 2.2 and section 2.3.

Another material that can be used in these applications is ZnO. It is a semiconducting, biocompatible and transparent material [27,28]. ZnO nanostructures are amongst the extensively researched material in the last decade for a range of applications such as solar cells, lasers, transparent conducting materials/coatings/electrodes, field emitters, surface acoustic wave devices and various sensors [29-31]. ZnO nanostructures have been widely investigated for sensing applications due to their properties such as biocompatibility, high electron mobility, chemical stability, electrochemical activity and ease of developing nanostructures through diverse methods at low-cost [29,30]. The above properties of ZnO nanostructures provide enhanced sensing characteristics and therefore, have been used to develop chemical sensors, UV sensors, gas sensors, biosensors, pH sensors and many others based on different sensing mechanisms [32,33]. ZnO and their composites have been used to modify the electrode for electrochemical sensing of metal ions [34], toxic gases [35], glucose [36] and antigen [37] to enhance their sensitivity.

Recently, there have been few reports on the ZnO based SPR sensors. Liang et al. [38] have developed SPR biosensor to detect the presence of tumour marker carbohydrate antigen CA15-3 in human saliva using Au/ZnO thin film and results have shown higher sensitivity over conventional SPR. Wang et al. [39] have developed SPR biosensor to detect rabit IgG using ZnO-Au composites and achieved a 16 fold lower detection limit over the conventional SPR. DNA hybridization has been detected by incorporating ZnO nanorod arrays on SPR by Byun et al. [40] and reported sensitivity improvement of more than three times.

Therefore, ZnO has been identified as the second material for modifying the sensor surface in order to enhance the sensitivity of the proposed hybrid sensor.

Sample/material characterization has been carried out based on techniques such as absorption spectroscopy, fluorescence spectroscopy, optical microscopy, scanning electron microscopy (SEM) and transmission electron microscopy (TEM). UV/Vis Spectrometer (Lambda 950) from Perking Elmer, Luminescence Spectrometer (LS50B) from Perking Elmer, Transmission Electron Microscope (JEM-1400) from JEOL and Scanning Electron Microscope (EVO LS10) from ZEISS have been used to characterize the samples. The material composition has been investigated using energy dispersive X-ray spectroscopy (EDX).

2.2 Gold Nanoparticle Synthesis

2.2.1 Chemicals

All the chemicals used in the experiments were analytical grade. Sodium citrate, sodium borohydride ($NaBH_4$), hydroxylamine hydrochloride and 3-aminopropyl trimethoxysilane (APTMS) were purchased from Sigma-Aldrich, UK. Hydrogen tetrachloroaurate (III) hydrate ($HAuCl_4 \cdot H_2O$) was purchased from Fisher Scientific, UK. All glassware was cleaned in deionized water prior to the experiment.

2.2.2 Synthesis Method

Gold nanoparticles (GNPs) were synthesized from gold chloride using sodium citrate reduction method [26]. Briefly, 0.2 ml 1% aqueous sodium citrate was added into 10 ml of 0.01% aqueous $HAuCl_4$ with vigorous stirring. After 1 min, 0.2 ml of 0.075% (w/v) $NaBH_4$ in sodium citrate was added. Thereafter, the solution was stirred for 5 min and the synthesized gold nanoparticles (referred as GNP1) were characterized by UV-Vis absorption spectra. The same process was repeated by increasing the amount of reducing agent (1% sodium citrate) to 1 ml and the synthesized particles were referred as GNP2.

Figure 2.1 shows the absorption spectrum of synthesized gold nanoparticles in water. GNP1 and GNP2 show the absorption peak, λ_{max}, at 513 nm and 532 nm respectively. Observed red shift in λ_{max} and increased absorption of GNP2 indicates an increase in the average particles size [41]. The reason behind the observed increase in particle size was due to the increased citrate (reducing agent) concentration [42]. GNP2 shows a strong plasmonic peak with reduced FWHM and increased falling edge slope. These results can be attributed to the increase in particle size with a reduction in their polydispersity [42].

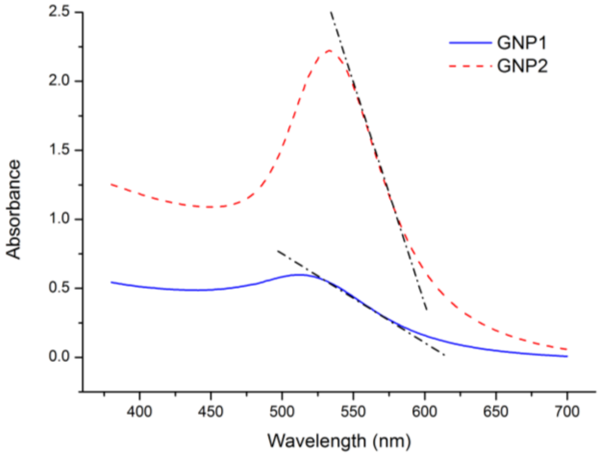

Figure 2.1 Absorption spectra of synthesized gold nanoparticles suspended in water.

The size of the synthesized gold nanoparticles was calculated from the UV-Vis absorption spectra. Gold particle size was calculated using the method by Haiss and team [43]. Particle size calculation was carried out for the GNP1 and GNP2 dispersed in water at 20°C without any surface modifications. In these calculations, the refractive index of water (n=1.3330) was assumed as wavelength independent.

Particle diameter, d (in nanometer) can be given by [43],

$$\mathrm{d} = \exp(B_1 \frac{\mathrm{A_{spr}}}{\mathrm{A_{450}}} - B_2) \qquad \ldots (2.1)$$

where, $B_1 = 3.55$ and $B_2 = 3.11$ derived from the calculations based on gold particles' absorption spectra, A_{spr} and A_{450} was absorption at plasmon resonance peak and at 450 nm wavelength respectively [43]. Substituting the corresponding values into equation (2.1), gives $d_1 = 3.39$ nm and $d_2 = 61$ nm which are in agreement with the literature [26,41,44].

Figure 2.2 shows TEM images of the synthesized GNP2 at different magnifications. From the images, it can be seen that the particles are polydispersed and <100 nm in diameter. Also, the calculated value of average diameter (61 nm) of GNP2 based on absorption spectra is in agreement with the observed TEM image data.

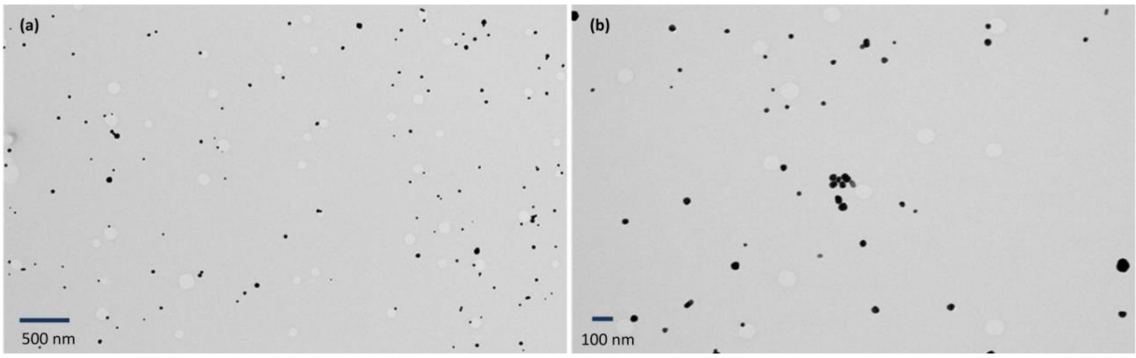

Figure 2.2 TEM images of the synthesized GNP2 at a scale of (a) 500 nm and (b) 100 nm.

2.3 Gold Thin Film Development

2.3.1 Synthesis Method

Gold thin films have been developed on a glass slide in order to prepare the electrode of the sensor using electroless plating method [26,45,46]. The chemicals used during this process are same as mentioned in section 2.2.1. The process was suitable for developing thin film on non-flat, non-uniform surfaces made of most widely used fibre materials and the developed coatings have been used as electrode of the sensor. Figure 2.3 shows the process flow diagram of developing the gold thin film on a glass slide using the electroless method. Broadly, the glass substrates were cleaned and silanated using APTMS and thereafter, GNPs were allowed to attach on the substrate. Furthermore, the GNP coated substrates were soaked in gold chloride solution and agitated on a shaker to form the film. Finally, substrates were annealed on the hotplate.

Glass substrates were cleaned using the ultrasonic bath in isopropanol, acetone and deionized water for 10 min each. Thereafter, substrates were soaked in 20% HCl solution for 30 min to remove the particulate materials from the surface. Substrates were immersed into a dilute solution of APTMS (0.26 ml of APTMS in 6 ml methanol) for 24 hours. Thereafter, the substrates were rinsed with methanol and annealed at 120° C for 30 min.

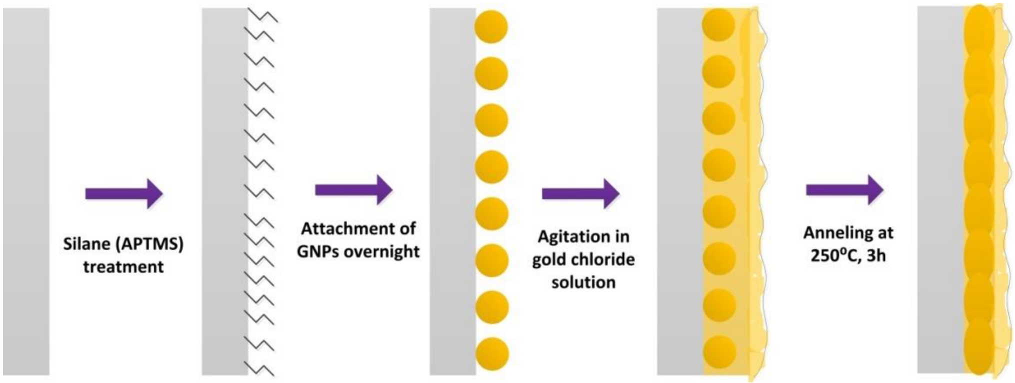

Figure 2.3 Process diagram of gold thin film development using electroless plating method.

The ultra-thin film of gold particles was developed by immersing the APTMS-coated substrates into the synthesized gold colloid solution for 24 hours. Thereafter, substrates were soaked in an aqueous mixture of 0.4 mM hydroxylamine hydrochloride and 0.1% (w/v) $HAuCl_4$ and were kept for agitation on shaker (120 rev/s) for 5 to 20 min. During the agitation process, substrate changes the colour from pink to purple to the gold cluster. Gold plated substrates were rinsed with water and annealed at 250°C for 3 hours.

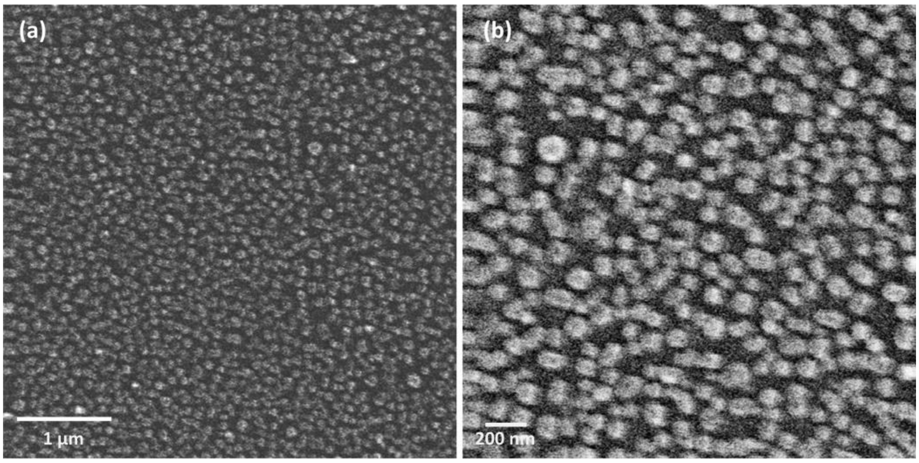

Figure 2.4 SEM images of GNPs deposited on glass slide after silane treatment at (a) 25Kx and (b) 50Kx magnification.

Figure 2.4(a) and (b) shows SEM images of GNPs coated on the glass substrate at different magnifications. As can be observed in the SEM images, particles were polydispersed and not exactly spherical in shape. The spatial distribution of the GNPs attached on the glass substrate seems to be nearly uniform at a larger scale. Extended magnification, (Figure 2.4(b)) shows that there are some patches of void areas at the nanometer scale (or spatial non-uniformity at the nanoscale).

Figure 2.5(a) shows the absorption spectra of developed gold thin films on glass substrates at different coating/agitation times. Three characteristic features have been observed in the spectra: red shift, broadening and increased absorption of plasmon peak. An increase in agitation/coating time results in an increase in the film thickness [26]. Increase in film thickness results in the red shift of the plasmon peak [47] from 537 to 567 nm in 5-20 mins as shown in Figure 2.5(b). Also, the increased film thickness has caused the broadening of plasmon peak and increase in the overall absorption.

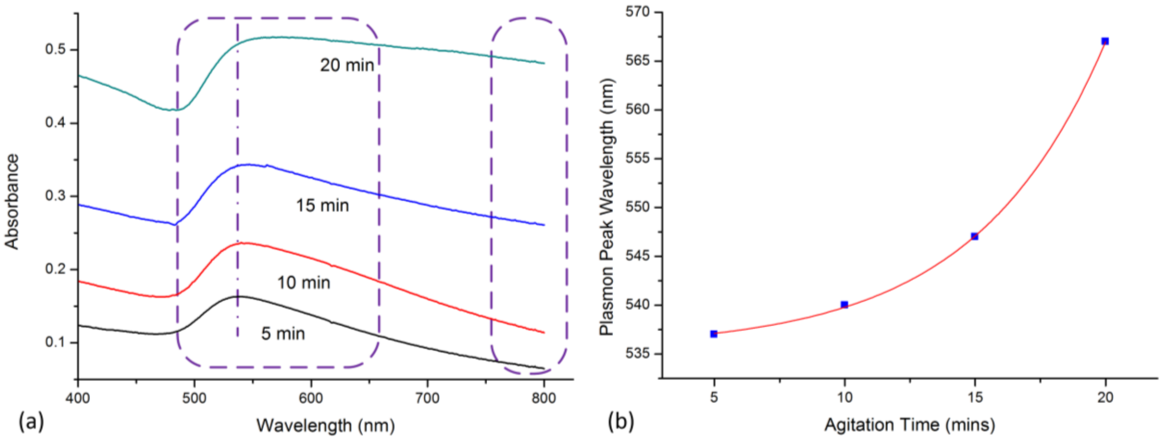

Figure 2.5 (a) Absorption spectra of developed gold thin film on glass slide for different agitation times of 5, 10, 15 and 20 mins and (b) variation of plasmon peak wavelength vs agitation time. The trend line shows an exponential fit to the data.

Figure 2.6(a) and (b) shows SEM images of the developed gold thin film (coating time 20 mins) on a glass substrate. At a larger scale, the film seems to be uniform with some patches of void areas. Furthermore, the magnified image (Figure 2.6(b)) reveals that the developed thin film is porous in nature with randomly distributed pores (<1 µm pore size). The observed nanoscale porous nature of the developed gold film can be ascribed to the observed non-uniform spatial distribution of the polydispersed GNPs seen in the previous step of the coating process. This has affected the homogeneity of the developed thin film.

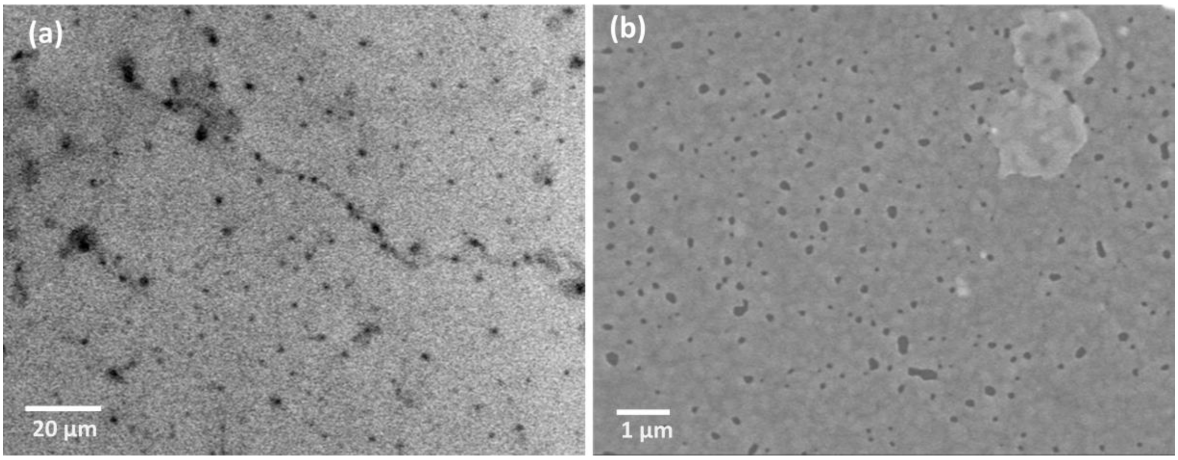

Figure 2.6 SEM images of the gold thin film deposited on a glass substrate using electroless deposition method at (a) 700x and (b) 10Kx magnification.

EDX spectrum was collected of the developed gold thin film and is shown in Figure 2.7. Strong characteristic peaks of gold along with the elements of glass such as silicon, calcium, oxygen, magnesium, sodium indicate the presence of gold thin film on a glass slide.

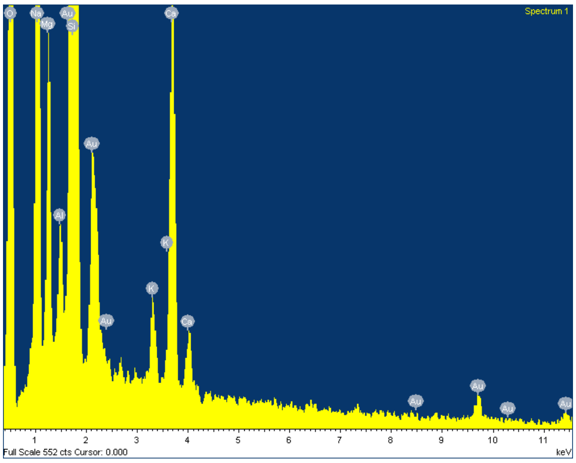

Figure 2.7 EDX spectrum of the developed gold thin film on a glass substrate.

Synthesis of gold nanoparticles and thin film has been carried out and the parameters affecting the process have been identified. Synthesized gold nanoparticles and thin films is used to study and characterize the chromophore and fluorophore, and as a metal coating for the electrochemical sensor development.

2.4 ZnO Nanoparticle Synthesis

As discussed, another material suitable for the hybrid sensor is ZnO. Therefore, synthesis of the ZnO nanostructures is carried out and discussed in this section. A higher yield of product and reaction rate can be achieved through rapid heating for shorter times using microwave irradiation. Therefore, microwave based synthesis method has been selected to synthesize the ZnO nanoparticles [48-50].

2.4.1 Chemicals

All the materials used in the experiments were analytical grade. Zinc acetate ($Zn(Ac)_2$), zinc nitrate hexahydrate ($Zn(NO_3)_2 \cdot 6H_2O$), ammonium hydroxide (NH_4OH), and hexamethylenetetraamine (HMTA) were purchased from the Sigma-Aldrich, UK. All glassware was cleaned in deionized water prior to the experiment.

2.4.2 Synthesis Method

In a 50 ml 10 mM zinc acetate solution, NH_4OH was added dropwise to adjust the pH to 10 while stirring the solution. After 20 min of stirring the solution at moderate speed, white precipitates were observed. Thereafter, the solution was kept in a domestic microwave oven (2.45 GHz) for 30 sec at 700 W and allowed to cool down at room temperature. A yellowish white solution of ZnO particles was observed after the microwave irradiation. The particles were separated by centrifugation and washed three times with methanol to remove the unreacted precipitate. The synthesis process was repeated for different microwave irradiation times such as 40, 60 and 70 seconds.

Synthesis process of ZnO nanoparticles was analyzed by taking the absorption spectra of samples before and after the microwave irradiation, as shown in Figure 2.8(a) and (b). The absorption spectrum of zincate precipitates (Figure 2.8(a)) shows a broad absorption peak at 590 nm and gradually increasing absorption towards the UV region. After 30 seconds of microwave irradiation, the excitonic peak of ZnO at 365 nm was observed [51]. Also, a broad absorption peak at 590 nm indicates the presence of unreacted precipitates. Thereafter, particles were separated using centrifugation and washed with methanol. The filtered particles were suspended in methanol and their absorption spectrum was measured as shown in Figure 2.8(c).

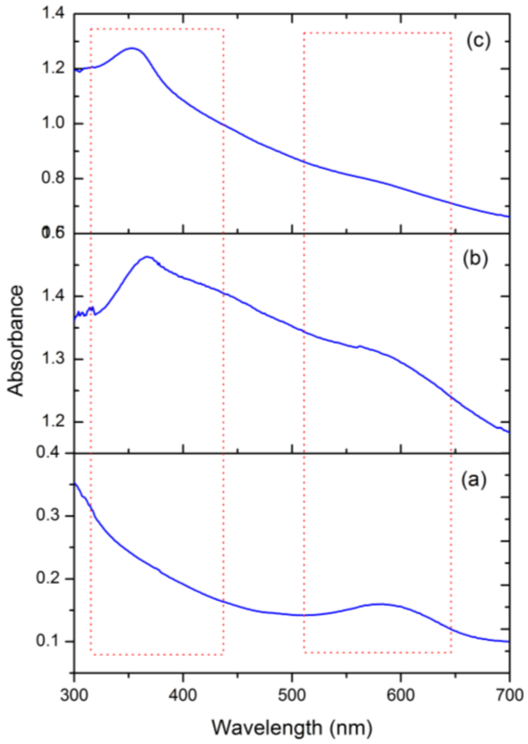

Figure 2.8 Absorption spectra of zincate precipitates before (a) and after (30 sec) microwave irradiation (b), and filtered ZnO nanoparticles (c).

Furthermore, the effect of microwave irradiation time on the particle was analysed by repeating the synthesis process for 40, 60 and 70 seconds and corresponding absorption spectra (normalized) were recorded (as shown in Figure 2.9). Three characteristic features were observed in the spectra: the blue shift of the excitonic peak, increase in the absorbance band edge slope and reduced absorption/scattering in the visible range. A longer irradiation time allows consumption of almost all the zincate precipitates, which may lead to the observed reduction in the visible absorption [52]. Also, the increase in the absorbance band edge slope and blue shift of the excitonic peak under the longer irradiation time can be attributed to the reduction in polydispersity of the particles [53]. The observed blue shift of the excitonic peak can be attributed to the change in particle size and/or shape [51,53].

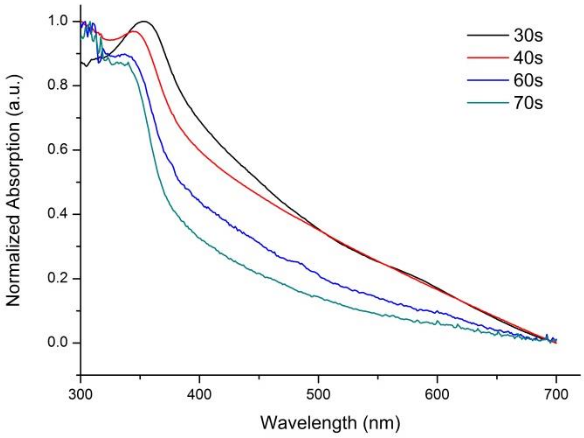

Figure 2.9 Absorption spectra of synthesized ZnO nanoparticles at different microwave irradiation time.

As per the effective mass approximation model, the bandgap of the ZnO nanoparticles (assumed spherical with radius *R*) can be represented by [54,55],

$$E_g = E_{g,bulk} + \frac{h^2}{8R^2 m_0}\left(\frac{1}{m_e} + \frac{1}{m_h}\right) \qquad \text{… (2.2)}$$

where, E_g and $E_{g,bulk}$ (=3.37 eV) are the bandgap of particles and bulk material, R is the radius of particle, m_0 is the mass of electron, m_e and m_h are the effective mass of electron and hole in ZnO. Calculated values of particle diameter (using equation (2.2)) for different microwave irradiation times were presented in Table 2.1. Following values were used for the calculation: m_e = 0.24, m_h = 0.45, m_0=9.11 x 10^{-31} kg, h=4.136 x 10^{-15} eV·s, 1 eV = 1.6 x 10^{-19} J and $E_g = 1240/\lambda_p$ [55]. Calculated values were similar to the ones reported in the literature [51,55].

Table 2.1 ZnO particle size and excitonic peak wavelength with microwave irradiation time

Microwave irradiation time (s)	Peak wavelength (nm)	Diameter (nm)
30	354	4.25
40	344	3.20
60	342	3.06
70	340	2.94

SEM images of the synthesized ZnO particles were taken at different magnifications (as shown in Figure 2.10) which shows that the particles were polydispersed (<100 nm) and seems to be nearly spherical in shape.

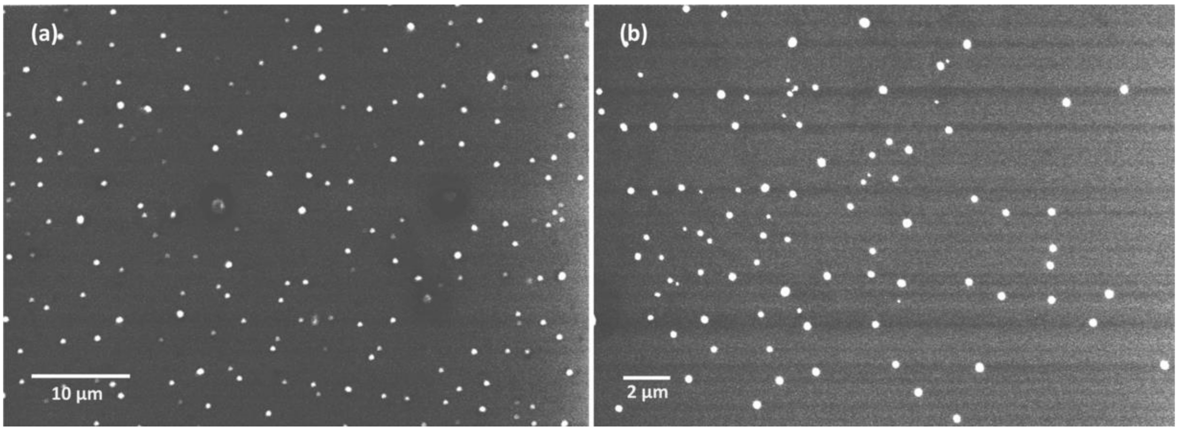

Figure 2.10 SEM images of ZnO nanoparticles synthesised using microwave synthesis method at (a) 3Kx and (b) 10Kx magnification.

Figure 2.11 shows the fluorescence spectrum of ZnO nanoparticles dispersed in ethanol. The spectrum shows four peaks at 387, 423, 481 and 528 nm. The strong peak at 387 nm corresponds to the near band edge emission, resulting from the recombination of excitons. The weak emission observed at 423, 481 and 528 nm can be attributed to the native lattice defects such as zinc and oxygen interstitials, zinc and oxygen vacancies [56].

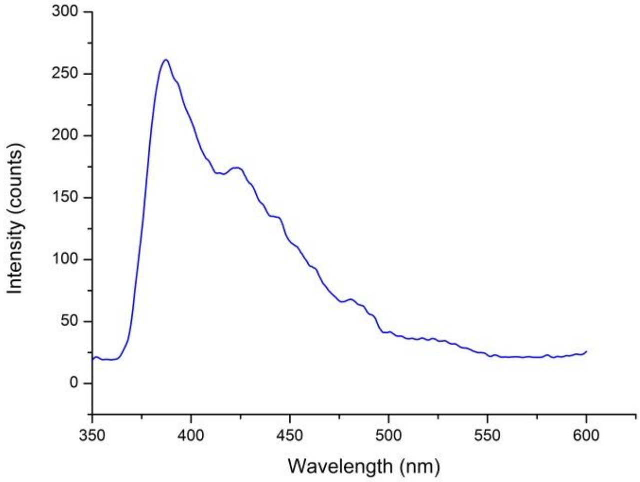

Figure 2.11 Fluorescence spectrum of the synthesized ZnO nanoparticles dispersed in ethanol excited at 315 nm.

2.5 ZnO Nanowire Synthesis

ZnO can be synthesized into different nanostructures like nanowire, nanorod, nanoring, nanoflakes, needles shape, flower shape, whiskers shape by various synthesis methods such as thermal evaporation [57], sonochemical [58], vapour liquid solid (VLS) growth [59], pulsed laser deposition (PLD) [60], hydrothermal

[61] and microwave [62]. In this work, simple and low-cost microwave and hydrothermal synthesis methods have been used to develop ZnO nanostructures for the sensor surface.

2.5.1 Synthesis Method

ZnO nanowires were grown on a glass substrate using hydrothermal seedless growth method [61]. The chemicals used during this process are same as mentioned in section 2.4.1. ZnO nanowires were grown by immersing the glass substrates into the mixture of 125 ml 20 mM zinc nitrate and 7 ml 28-30% ammonium hydroxide and annealed on a hotplate at 95°C for 5 hours. Thereafter, substrates were removed from the growth solution and rinsed with deionized water for several times. The substrates were allowed to dry at room temperature and atmospheric pressure before characterization.

Figure 2.12 shows SEM images of the synthesized ZnO nanostructures at different magnifications. A high magnification SEM image reveals that their structure looks like bundles of nanowires. Results could be explained by the fact that in case of no seed layer, a nucleation site must be formed before the growth process. Consumption of Zn^{2+} ions is very high in the areas where crystal starts to build. Therefore, the availability of Zn^{2+} ions near the nucleation site is low which leads to the formation of branches in the crystal (as seen in Figure 2.12). Overall, non-availability of the seed has caused the growth rate to slow down and bulk crystal formation with less density.

To reduce the bulk crystal formation and improve the density, the seed layer has to be deposited first. Therefore, using a drop casting approach, a seed layer was formed as follows: 10 mM zinc acetate was drop casted on the glass substrates and annealed on hotplate for 1 min at 100 °C for better adhesion. The process was repeated 5 times to get the uniform thick seed layer. Thereafter, substrates were immersed in the growth solution and allowed to grow for 5 hours at 95 °C. Thereafter, substrates were removed from the growth solution and rinsed with deionized water for several times. The substrates were allowed to dry at room temperature and atmospheric pressure before characterization.

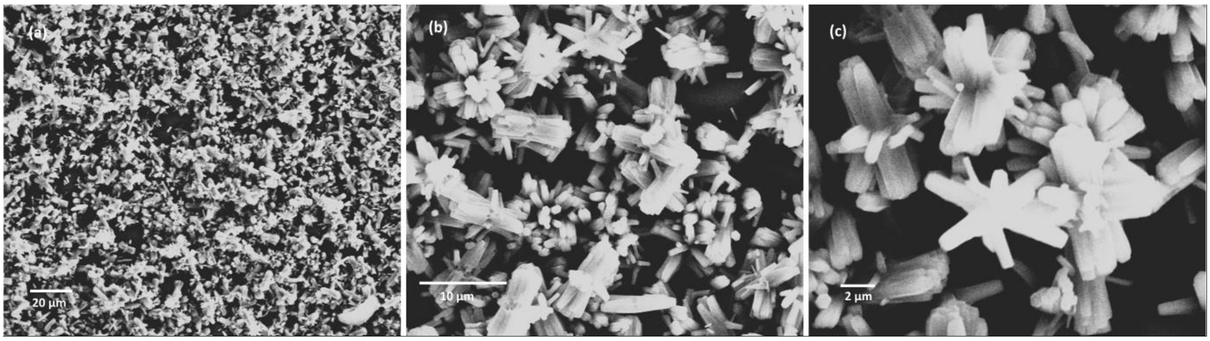

Figure 2.12 SEM images of the synthesized ZnO nanowires at (a) 800x (b) 3Kx and (c) 6Kx magnification.

Figure 2.13 shows the SEM images of synthesized ZnO nanowires at different magnifications. Dense and c-axis oriented growths with hexagonal facets of the ZnO nanowires can be observed in the images. Most of the nanowires were randomly oriented and seems to be uniform in diameter (~950 nm). The availability of nucleation sites, lead to the immediate growth of a crystal in c-axis direction [63]. Growth of ZnO nanowires over the thick seed layer was highly dense, uniform in diameter with random orientation.

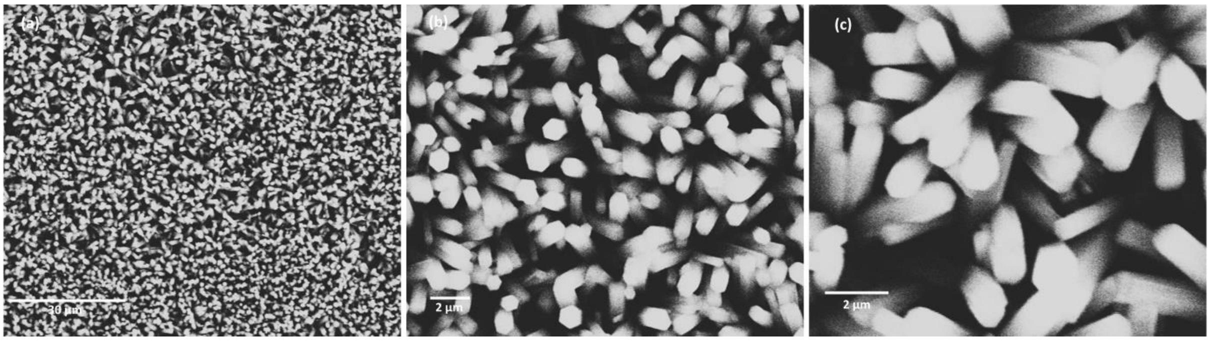

Figure 2.13 SEM images of synthesized ZnO nanowires at (a) 1Kx, (b) 7Kx and (c) 12Kx magnification.

To understand the effect of seed layer and concentration of Zn^{2+} ions on the shape and size of ZnO nanowires, experiments were carried out with different concentrations. The seed layer was formed with increased concentration of zinc acetate (20 mM) and same growth process was repeated. Figure 2.14 shows the SEM images of the synthesized ZnO nanowires at different magnifications. It was observed that grown nanowires have a random orientation with preferential c-axis growth and hexagonal facets. It was also observed that the diameter of the nanowires was reduced and the density increased, which can be attributed to the increased concentration of zinc acetate in the formation of the seed layer. The observed effect can be explained as follows: the increase in the concentration of zinc acetate resulted in an increase in the nucleation sites. As the concentration of species in the growth solution was kept same, the increased nucleation sites and the limited concentration of zinc ions in the growth solution led to the increased density and reduced nanowire diameter [53,63].

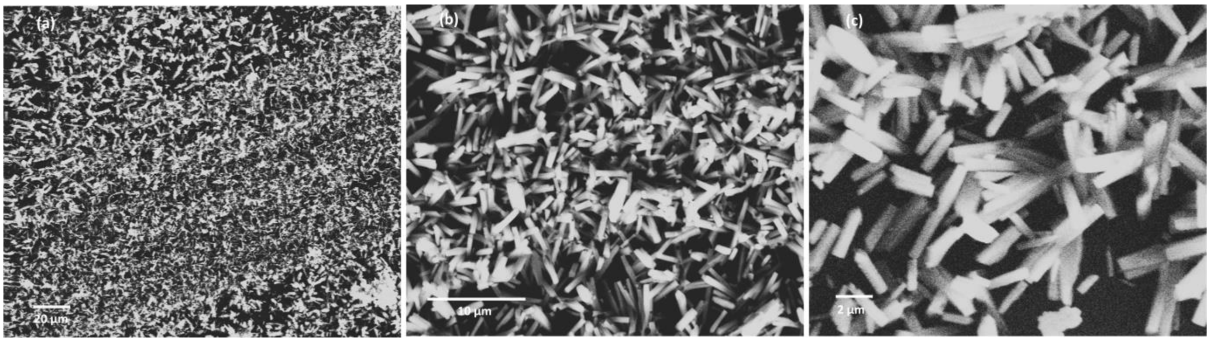

Figure 2.14 SEM images of synthesized ZnO nanowires at (a) 700x, (b) 4Kx and (c) 7KX magnification.

A second experiment was carried out with increased concentration of zinc nitrate (50 mM) in the growth solution. Figure 2.15 shows the SEM images of the synthesized ZnO nanowires at different magnifications. Results indicate that the nanowires were randomly oriented towards the c-axis with hexagonal facets. But instead of the flat tip end, pointed tip were observed. ZnO has preferential growth along the [0001] direction and also higher growth rate. Increased concentration of zinc nitrate in the growth solution has increased the availability of Zn^{2+} ions at the nucleation sites. This led to the increased growth rate along the [0001] direction compared to the other directions which caused the nanowires tip to be pointed [49].

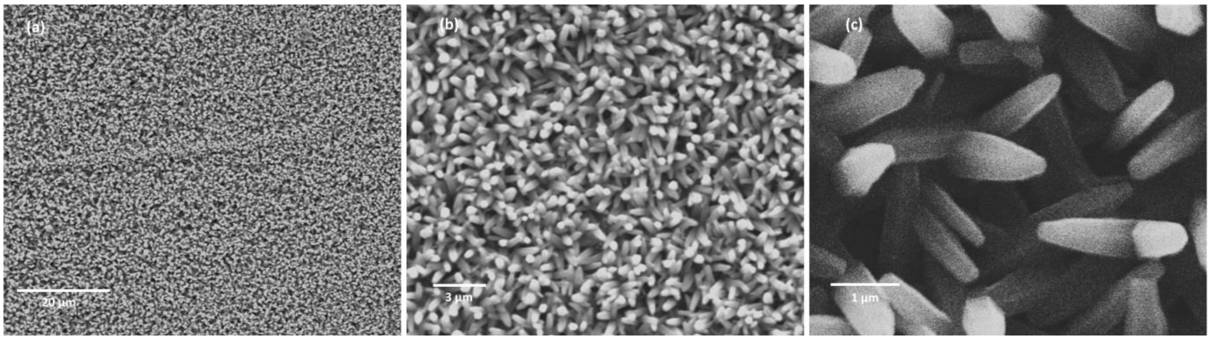

Figure 2.15 SEM images of synthesized ZnO nanowires at (a) 2Kx, (b) 6Kx and (c) 25Kx magnification.

EDX spectrum was measured of the synthesized ZnO nanowires as shown in Figure 2.16. A strong characteristic peak of zinc and oxygen and a weak peak of silicon and calcium indicate the presence of ZnO on the glass slide.

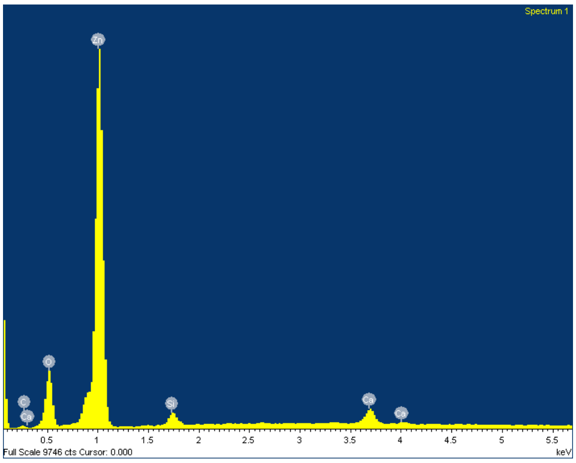

Figure 2.16 EDX spectrum of the synthesized ZnO nanowires grown on a glass substrate.

Synthesis of ZnO nanostructures has been carried out and the effect of various parameters affecting the synthesized ZnO nanostructures have been analysed and discussed. Developed ZnO nanostructures will be used to modify the sensor surface.

2.6 Dithizone

Dithizone has been used for many years as an extractor or pre-concentration sorbent prior to the atomic absorption spectrometry [64,65], GC-MS [66] and ICP-OES [67] for metal ion detection. Dithizone has also been used in potentiometric [68], optodes [69] and spectrophotometric [70] determination of metal ions. Dithizone produces distinct absorption spectra in the presence of metal ions in aqueous solutions [71]. Therefore, dithizone has been selected and investigated for heavy metal sensing in this work.

Chemical structure of the dithizone (diphenylthiocarbazone) is shown in Figure 2.17. As seen in the structure, it consists of many donor groups such as –NH and –SH which are specific for metal ions. Typically, S-C-N-N group usually forms the complex with metal ions by the removal of hydrogen atom [72]. Dithizone is insoluble in water, but dissolves in solvents such as ethanol, methanol, acetonitrile, toluene, carbon tetrachloride, chloroform and acetone [73]. But, it has been reported that dithizone is not stable in most solvents and exists in two tautomeric forms [74]. Therefore, prior test were conducted on the stability of the dithizone in different solvents over a month. It was found that dithizone is stable in isopropanol even after 30 days. Isopropanol (IPA) and dithizone are both hydrogen donor molecules and therefore, intermolecular charge transfer possibility was forbidden amongst them [75]. This could be the reason behind the observed stability of dithizone in IPA. Therefore, for the characterization and other analysis, isopropanol has been used as a solvent to dissolve the dithizone. Normalized absorption spectra of the dithizone in different solvents have been shown in appendix – I.

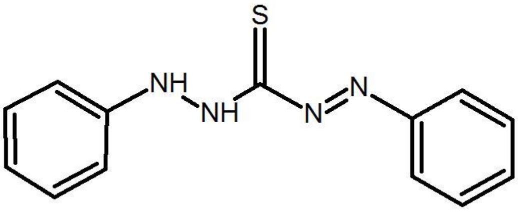

Figure 2.17 Chemical structure of dithizone.

Figure 2.18(a) shows the UV/Vis absorption spectra of the dithizone at various concentrations in isopropanol. Two absorption peaks observed in the visible spectrum at 445 nm and 598 nm were ascribed to the π-π^* and n-π^* transition [73,76]. Also, there is a blue shift of λ_{max} observed in the shorter visible absorption band at higher concentrations. A calibration spectrum of the dithizone is plotted at 598 nm as shown in Figure 2.18(b).

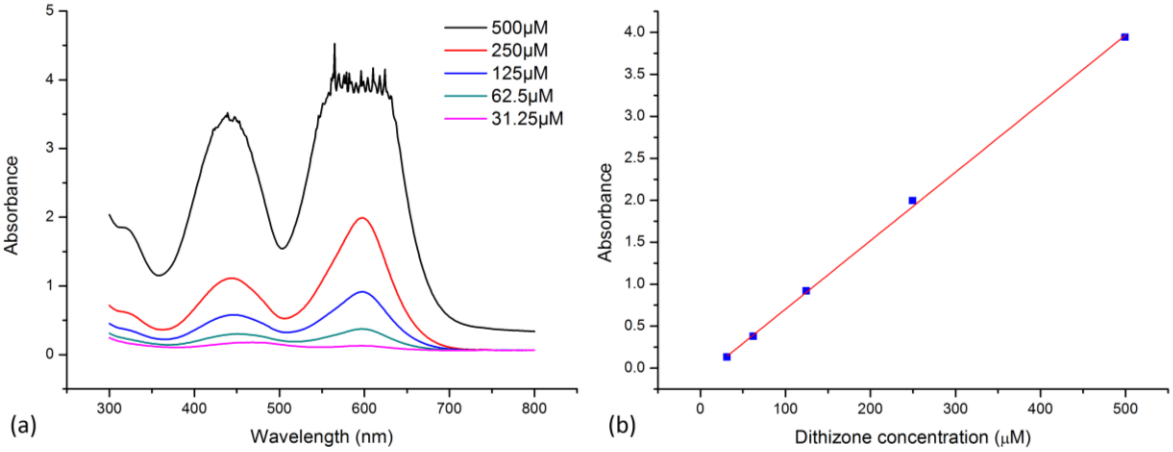

Figure 2.18 Dithizone UV/Vis absorbance spectra (a) and calibration curve plotted at 598 nm (b). The red line shows the linear fit to the data.

2.6.1 Dithizone-Metal ions Interaction Study

Metal ions were adsorbed on the binding site formed by apex S and N atoms of the dithizone as shown in Figure 2.19(a). Dithizone forms the complex with the mercury ions by the removal of hydrogen atom [72] and is called mercury dithizonate. Figure 2.19(b) shows the absorption spectra of the dithizone and mercury dithizonate. The spectra show that due to this metal ion complexation process, the absorption band of the dithizone at longer wavelengths diminishes and absorption band at shorter wavelengths undergoes a red shift. These two phenomena is further explored in the following paragraph.

When the metal ions chelate with dithizone, due to the electrostatic interaction among them, electrons in the S-C-N-N group of dithizone move towards the metal ion [77]. This movement causes the deformation in the highest occupied molecular orbital (HOMO) of the dithizone [78]. The deformation in HOMO causes the alteration in the electron energy levels and consequently, is responsible for the shift in shorter wavelength absorption band of dithizone. While, as stated earlier, the binding of metal ions cause the removal of a hydrogen atom and therefore, is the reason for the disappearance of longer absorption wavelength band [73].

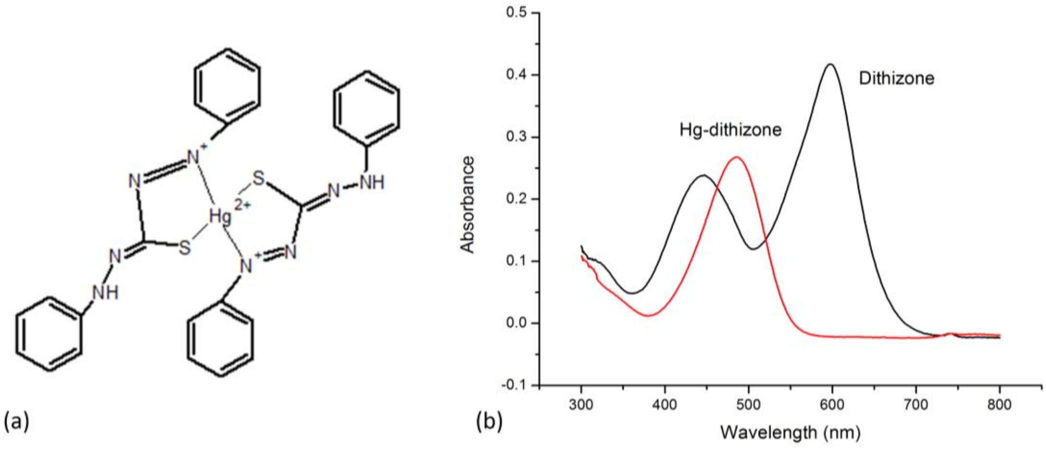

Figure 2.19 (a) Chemical structure of mercury dithizonate and (b) the absorbance spectrum of dithizone and mercury dithizonate.

As discussed, to understand the event of binding and adsorption, different metal ions (50 ppm each) were mixed with dithizone (78 µM) solution. Solutions were mixed by shaking and absorption spectra were collected after allowing 30 s of settling time, as shown in Figure 2.20. Mercury and copper ions have absorption peaks at 488 and 433 nm respectively. Shorter wavelength absorption band of cadmium, zinc and nickel ions were observed at 478, 525 and 442 nm respectively while the longer wavelength absorption band was around 592 nm.

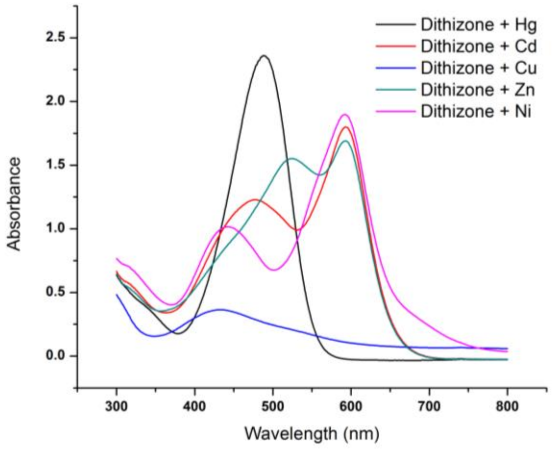

Figure 2.20 Absorbance spectra of dithizone with different metal ions (50 ppm).

Absorbance spectra indicate that the absorption band at longer wavelengths diminishes in the case of mercury and copper ions only, which indicates that mercury and copper bind to the dithizone by the removal of hydrogen [73]. Adsorption of the cadmium, zinc and nickel ions cause the alteration in electron energy levels of dithizone resulting in the observed shift in shorter wavelength absorption band, and therefore, the colour difference in the solutions. This investigation reveals the possibility of selectively detecting the metal ions and also, the possible interference from other metal ions. This possibility is further explored in the final design of the sensor for selective determination of metal ions using electrochemical sensing as a complementary technique.

2.6.2 Dithizone-GNP Interaction Study

A combination of GNPs with dithizone further enhances the selectivity and sensitivity in the detection of heavy metal ions [79]. Possible reasons for that enhancement include, electronic transitions, formation of different bonds, metal ion complexation assisted aggregation of GNPs and π – interactions which led to broadening or shifting of plasmon peak or appearance of new absorption peaks. It has been reported that dithizone improves the sensitivity in electrochemical sensing by using dithizone modified gold electrode to detect copper ions [68].

A strong affinity between gold and thiol is well known. Therefore, dithizone is likely to bind the GNP with thiol bond. To investigate this binding effect on the optical spectrum, absorption spectra of GNP (0.01 w/v), dithizone (78 µM) and a mixture of them were collected. Figure 2.21 shows the normalized absorption spectra of dithizone, GNPs and GNPs with dithizone. Characteristic plasmon peak of GNPs appears at 530 nm and the absorption peaks of dithizone appear at 435 and 590 nm respectively. Mixing the gold NP with dithizone results in broadening of the plasmon peak due to the binding of dithizone on the gold NP surface and a new peak appears around 700 nm due to the dithizone-gold interaction [79].

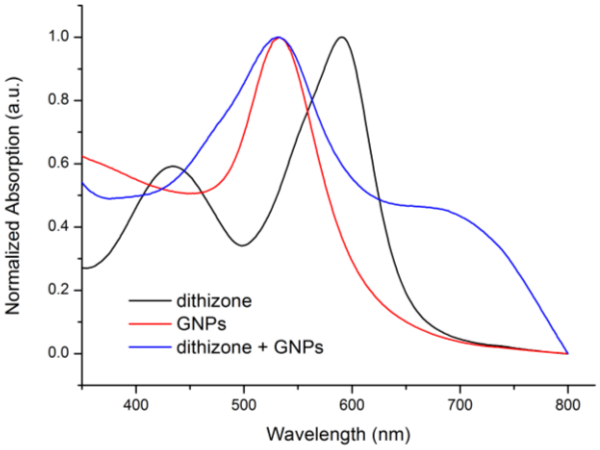

Figure 2.21 Normalized absorption spectra of dithizone, GNPs and GNPs + dithizone.

To further investigate the effect of dithizone modified GNPs for metal ion sensing, copper ions were used as model metal ions. Figure 2.22 shows the absorption spectra of dithizone modified gold nanoparticles with and without copper ions (50 ppm). In order to avoid direct contact between copper ions and dithizone, high concentration of dithizone (250 µM) was used and also, the concentration of GNPs was reduced from 0.01 to 0.005% w/v. The solution was kept overnight to allow the binding of maximum dithizone on GNPs surface and the same solution was used to check the copper ion binding effect. Therefore, there is a possibility that leftover dithizone may contribute to the observed absorption spectrum. This results in the integration of the shorter and longer wavelength absorption bands of dithizone with the GNPs spectrum. The addition of copper ions, results in the blue shift of the plasmon peak which was evaluated based on slope change (0.0142 to 0.0214) of the leading edge of plasmon peak. The integrated effect leads to a shift of peak wavelength from 590 to 561 nm.

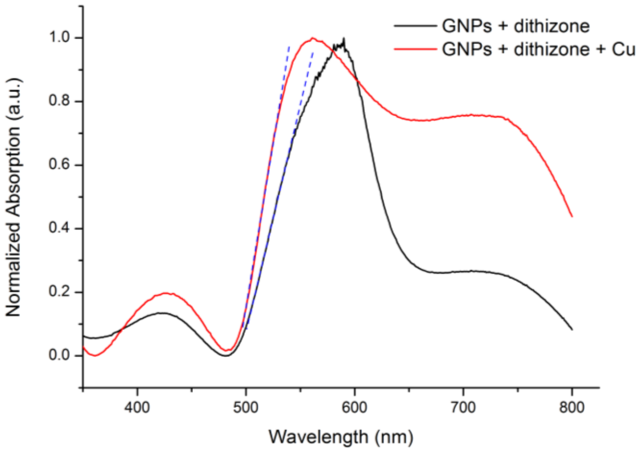

Figure 2.22 Normalized absorption spectra of dithizone + GNPs with and without copper ions.

2.6.3 Dithizone-ZnO Interaction Study

ZnO is a wide bandgap (~3.37 eV) semi-conducting biocompatible material. Dithizone and ZnO interaction has been investigated in order to design a sensor, where ZnO works as an electrode or immobilizing agent for dithizone and their integrated effect will be exploited to detect heavy metal ions using complementary optical and electrochemical methods. Effect on the optical spectrum has been studied using ZnO nanoparticles and dithizone absorbance spectrum as shown in Figure 2.23 (a). ZnO NP excitonic absorption peak was observed at 360 nm while the dithizone absorption peaks at 460 and 596 nm respectively. ZnO NPs were suspended in the ethanol and dithizone was dissolved into ethanol. Both solutions were mixed by handshaking and absorption spectra were measured over 30 min period.

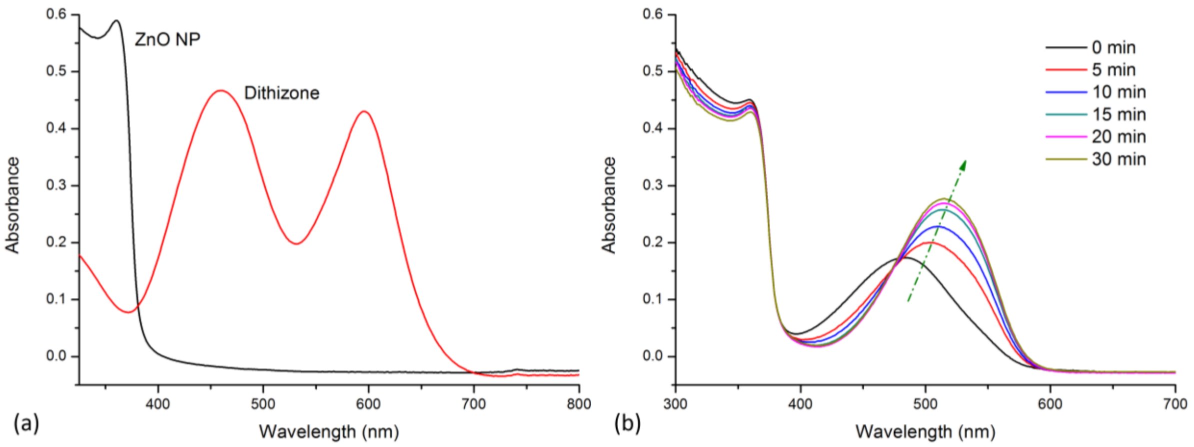

Figure 2.23 (a) Absorbance spectrum of ZnO NP (0.04% w/v) and dithizone (78 μM) in ethanol and (b) time lapse absorbance spectra of dithizone-ZnO NP over 30 min.

The absorbance spectrum of dithizone-ZnO NP in Figure 2.23 (b) at 0 min shows the ZnO excitonic absorption peak at 360 nm and only shorter wavelength absorption band shifted to 484 nm. The disappearance of the longer wavelength band of the dithizone clearly indicates their binding on the ZnO NP surface [73]. Over a period of 30 min, more and more dithizone molecules bind to the surface of ZnO NP which led to the red shift in absorption band peak wavelength from 484 to 515 nm and an increase in absorption. Binding process of dithizone on the ZnO NPs surface is further studied in isopropanol to avoid instability issues of dithizone. The process was characterized over a period of 3 hours using absorption spectroscopy (results shown in appendix - II) and the same results have been found as in the case of ethanol.

2.6.4 Dithizone-ZnO-Metal ions Interaction Study

A study has been carried out to understand the capability of dithizone to detect metal ions after binding/immobilizing on ZnO NP surface. Figure 2.24 shows the normalized absorption spectra of dithizone immobilized ZnO particles (0.04% w/v) with different metal ions (5 ppm each). Exciton peak of ZnO and dithizone peak after immobilization on ZnO were observed at 365 and 515 nm in the absorption spectrum. The second absorption band of dithizone at a higher wavelength (~600 nm) disappears because of the immobilization. It was observed that the short wavelength absorption peak of dithizone shifts 5 nm (shifted to 510 nm) for Hg, Cd, Zn, Ni and Cu each. This effect can be attributed to the electrostatic interactions between metal ions and dithizone [77]. On the other side, ZnO absorption peak did not show any change to Hg, Cd, and Cu, but absorption reduced in the case of Zn and Ni. The observed effect on ZnO absorption peak requires further investigations.

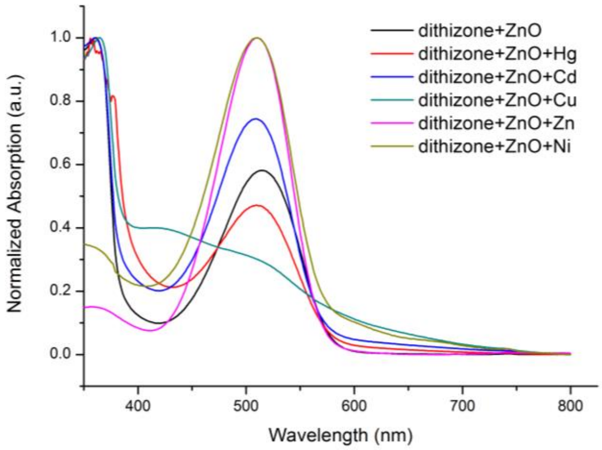

Figure 2.24 Normalized absorption spectra of dithizone-ZnO NP with different heavy metal ions.

2.7 Rhodamine B

Rhodamine and its derivatives are widely used in a variety of fields such as environmental sensing, biological sensing, laser dyes etc [80,81]. Rhodamine derivatives have been used as chemosensors/optical probes/fluorophores to detect heavy metal ions such as mercury, copper, iron, chromium etc [82-86]. As discussed, in chapter 1, FRET-based sensors using rhodamine derivatives and gold nanoparticles are becoming popular over the last decade. Recently, sensors have been developed based on GNP-RhB FRET mechanism for the detection of melamine in milk [87], detection of drug like clenbuterol widely used for the asthma patients [88] and detection of antioxidant like glutathione [89]. There are reports on FRET mechanism based fluorescence sensors to detect Hg^{2+} using rhodamine derivatives and gold nanoparticles [20-22]. Also, the sensor has been developed to detect Zn^{2+} in water using RhB and GNPs FRET mechanism [90]. But, so far to my knowledge, there has been no study carried out to detect copper ions using GNP-RhB FRET mechanism. Therefore, initial investigations have been carried out to study various interactions among RhB, GNP and copper ions using absorption and fluorescence spectroscopy.

Figure 2.25 shows the chemical structure of Rhodamine B (RhB). A structure indicates the zwitterion structure, therefore, can exist in a different form under different pH and solvent conditions [91]. Also, two alkyl substituents attached with each nitrogen atom indicate that the fluorescence lifetime and quantum yield can vary with temperature due to the activation of internal conversion process [80]. Therefore, RhB can be used in temperature sensing applications.

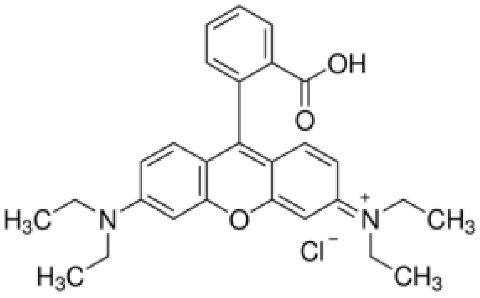

Figure 2.25 Chemical structure of RhodamineB.

Absorbance study of RhB in water was carried out by collecting absorption spectra at different concentrations as shown in Figure 2.26(a). It has been observed that RhB has strong absorption at 554 nm and weak absorption bands at 520, 400 and 354 nm corresponding to different molecular transitions. A curve of concentration vs peak absorption measured at 554 nm is shown in Figure 2.26(b).

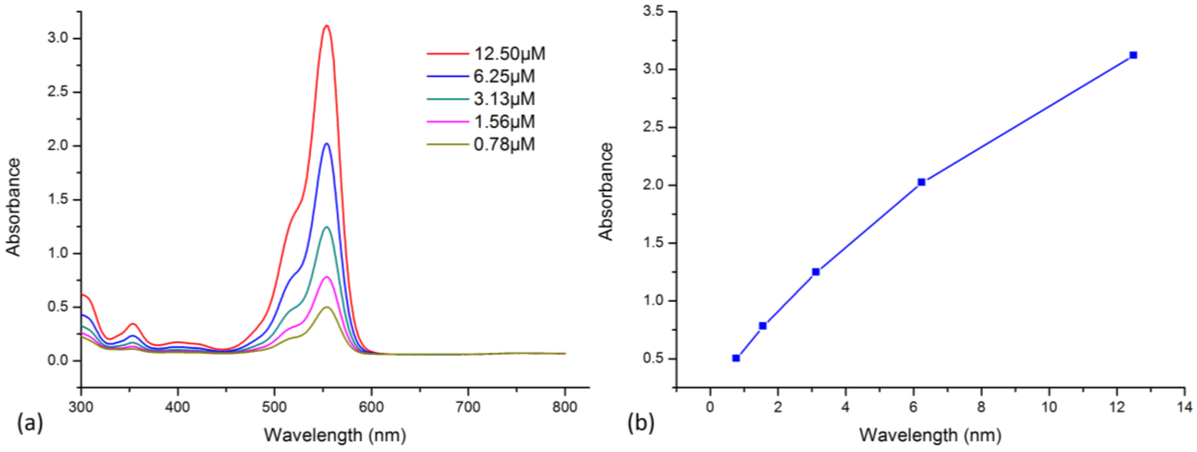

Figure 2.26 (a) Absorbance spectra of RhB at various concentrations and (b) the peak absorbance vs concentrations curve.

It was observed that the rate of increase in the intensity reduces at high concentration of RhB which might be related to the fact that at high concentration, RhB molecules starts to arrange themselves in the form of dimers or large aggregates [92,93].

Fluorescence spectra of different RhB concentrations have been recorded as shown in Figure 2.27(a). Self-quenching of fluorescence occurs at high concentrations of RhB, which can be seen as a decrease in the slope of intensity vs concentration trend (shown in Figure 2.27(b)). This self-quenching fluorescence effect can be attributed to the dipole-dipole interactions of RhB where excited monomer transfers the energy to the aggregates [93]. With lowering concentration, RhB molecules start to isolate completely from each other and results in the blue shift in the emission peak. The observed effect can be attributed to the molecule orientation and intermolecular interactions [92,94].

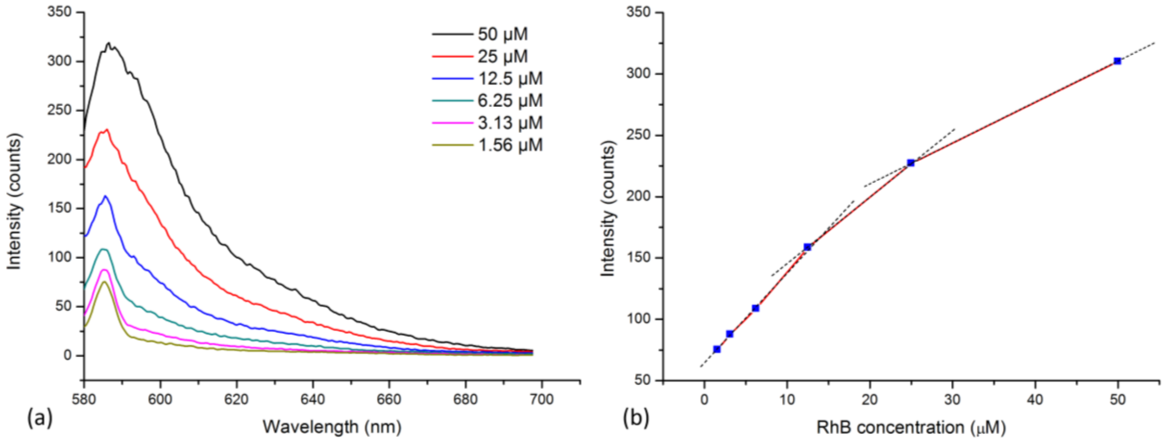

Figure 2.27 (a) Fluorescence spectra of RhB at various concentrations excited at 570 nm and (b) the plot of peak intensity vs concentration.

2.7.1 RhB–GNP Interactions Study

Absorbance spectra of RhB (12.5 μM) with various concentrations of GNPs have been collected as shown in Figure 2.28(a). The spectrum indicates a reduction in absorption after the addition of GNP solution into RhB solution due to the dilution. Also, addition of GNPs in RhB solution results in the appearance of other absorption band near 750 nm. Increased absorption and the red shift have been observed in this absorption band with increased GNPs concentration. An increase in the GNPs concentration has caused the increase in the baseline of the spectrum. Plasmon peak of GNPs has been integrated into the RhB peak, therefore, no clear change can be observed. To understand the adsorption process of RhB on GNP, a time-lapse study was carried out over a period of 10 mins and corresponding absorption spectra were recorded (as shown in Figure 2.28(b)). Reduction in the absorption was observed in both the peaks. Also, the shorter wavelength absorption band starts blue shifting (from 554 to 549 nm), while the longer wavelength absorption band starts red shifting (from 733 to 755 nm). The observed effect can be attributed to the adsorption of RhB on GNPs surface [95].

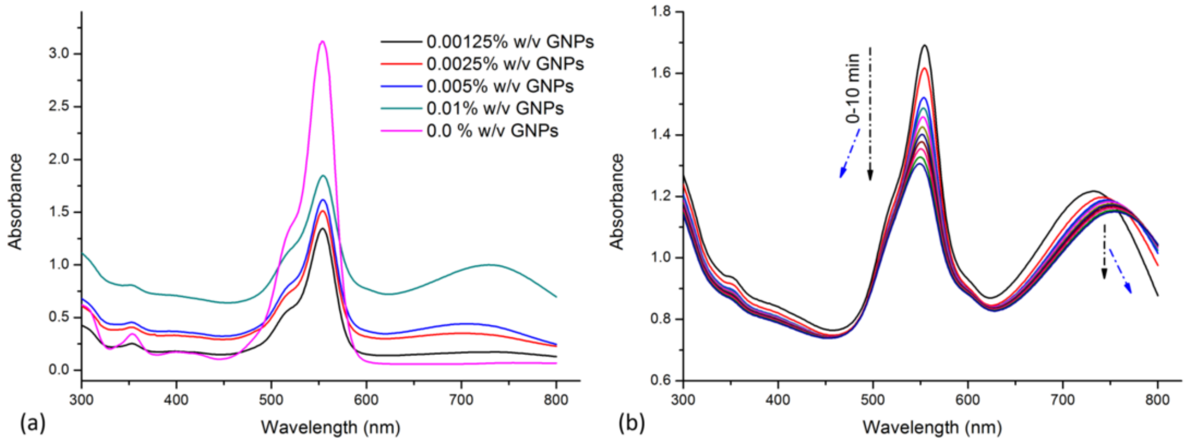

Figure 2.28 Absorbance spectra of 12.5 μM RhB (a) with various concentrations of GNPs and (b) with 0.01% w/v GNP over a period of 10 mins.

Effect of GNPs on the RhB fluorescence is evaluated in Figure 2.29 for 25 μM RhB with and without GNPs with varying concentrations of GNPs. The excitation wavelength used was 570 nm. It was observed that the addition of 0.00125% w/v GNPs in RhB solution enhances the fluorescence of RhB. The observed RhB fluorescence enhancement can be attributed to the coupling of RhB fluorescence with the local field enhancement of GNPs surface plasmon [96]. The observed coupling effect (fluorescence enhancement) strongly depends on the distance between RhB and GNPs surface. Also, it is notable that the RhB emission spectrum overlaps with the GNPs absorption spectrum, a primary required condition for efficient fluorescence resonance energy transfer (FRET), provided that the RhB molecules are sufficiently in close proximity to GNP surface. Further increase in the GNPs concentration forces the RhB molecules closer to the GNPs surface. This reduced distance allows the non-radiative energy transfer from RhB molecules to GNPs which leads to the observed fluorescence quenching [96].

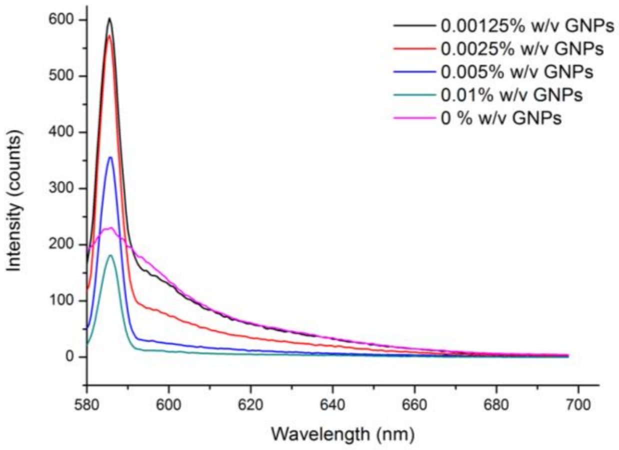

Figure 2.29 Fluorescence spectra of RhB-GNPs with varying concentrations of GNPs at 570 nm excitation wavelength.

2.7.2 RhB–GNP–Copper ions Interaction Study

A study was carried out using GNP-RhB in order to detect the copper ions based on the FRET effect. Two excitation wavelengths were used 570 and 500 nm as shown in Figure 2.30.

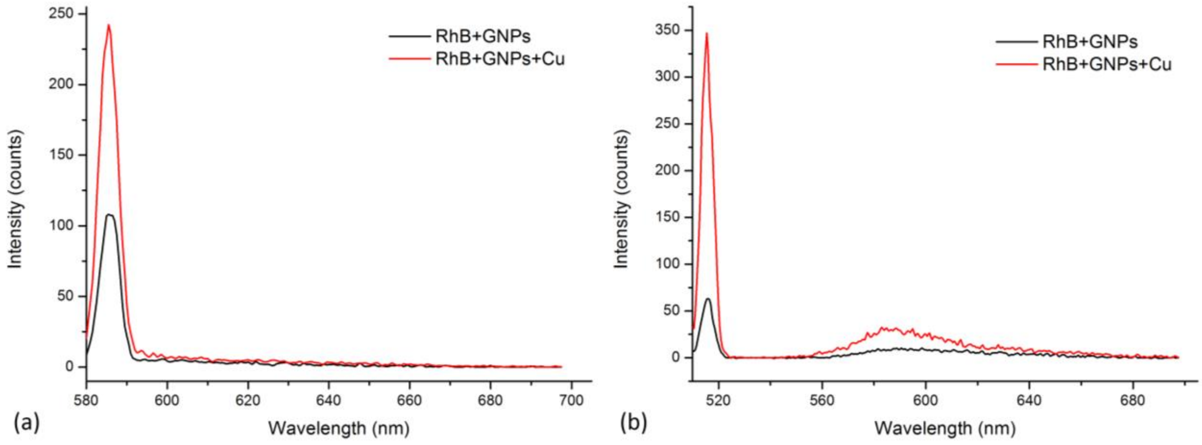

Figure 2.30 Fluorescence spectra of RhB+GNPs with and without Copper (Cu) ions at the excitation wavelength of (a) 570 and (b) 500 nm.

As discussed earlier, 0.01% w/v GNPs in 25 μM RhB solution quenches the RhB fluorescence as shown in Figure 2.30(a) and (b). An addition of 50 ppm copper ions increases the intensity of RhB fluorescence signal. The effect has been observed at both excitation wavelengths. Copper ions penetrate through the shell of RhB and reach the GNPs surface. The process led to an increase in GNP to RhB molecules distance. The increased distance reduces the non-radiative energy transfer from RhB to GNPs surface, but still in a close proximity to allow the coupling with local field enhancement. Therefore, addition of 50 ppm copper ions converts fluorescence quenching effect of RhB into fluorescence enhancement effect. When the RhB+GNPs solution was excited at 500 nm (as shown in Figure 2.30(b)), apart from the strong main fluorescence peak at 515 nm, second broad and weak fluorescence peak was observed at 585 nm. The observed weak fluorescence signal was due to the reabsorption and emission of strong emission observed at 515 nm by the RhB molecules which are beyond the distance of localized GNPs surface field effect. In order to confirm that there is no influence of copper ions in the above sensing mechanism, copper ions, and RhB fluorescence interaction study was carried out.

2.7.3 RhB–Copper ions Interaction Study

Effect of copper ions on RhB fluorescence was studied as shown in Figure 2.31. A solution of 25 µM RhB was excited at 570 nm and corresponding fluorescence spectra were recorded at various copper ions concentrations. Fluorescence results indicate that copper ions do not cause an enhancement or quenching in the RhB fluorescence. This result supports the investigated FRET based copper ion sensing mechanism using RhB-GNPs.

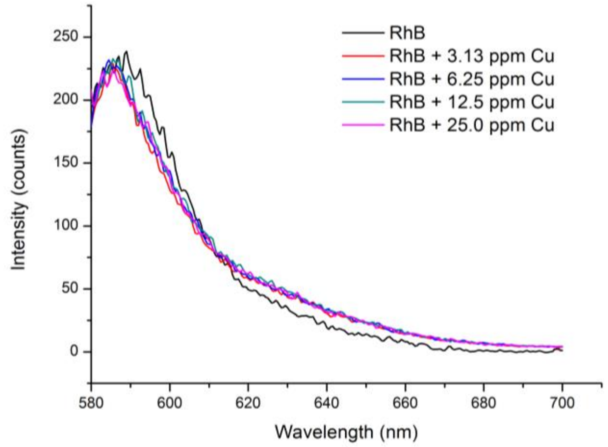

Figure 2.31 Fluorescence spectra of RhB with various concentrations of copper ions.

2.8 Summary

Materials such as Gold and ZnO have been identified for the development of proposed hybrid sensor surface. Gold nanoparticles have been synthesized and the gold thin film has been developed on the glass in order to develop sensor surface for optical and electrochemical sensing. Synthesis of ZnO nanoparticles and ZnO nanowires has been carried out in order to modify the sensor surface to enhance the surface area of the electrode and increase the sensitivity. Dithizone has been identified as suitable chromophore and its interactions with metal ions have been studied using absorption spectroscopy. Results have indicated that it can be used for sensitive and selective detection of heavy metal ions. RhodamineB has been identified as the fluorophore for copper ion detection and its fluorescence study have been carried out using fluorescence spectroscopy. FRET mechanism based copper ions detection has been investigated. Obtained results indicated that copper ions can be detected using RhB-GNP based FRET mechanism. Further investigations will be required to optimize the parameters such as particle size and concentration range in order to develop the sensor based on GNP-RhB FRET based copper ion detection study.

Heavy metal ions detection using dithizone will be exploited in the chapter 3 for the development of an optical fibre based heavy metal ions sensor. RhB fluorescence is temperature dependent. Recently, micro temperature sensor has been reported using RhB [97], nano-thermometer have been reported using RhB derivative [98]. Therefore, RhB can be integrated along with the proposed hybrid sensor in order to incorporate the temperature effects on the measurements. Heavy metal ions sensing using RhB will be exploited in the future work.

2.9 References

[1] A. Navrotsky, C. Ma, K. Lilova, N. Birkner, Nanophase Transition Metal Oxides Show Large Thermodynamically Driven Shifts in Oxidation-Reduction Equilibria, Science. 330 (2010) 199-201.

[2] A.N. Shipway, E. Katz, I. Willner, Nanoparticle arrays on surfaces for electronic, optical, and sensor applications, Chemphyschem. 1 (2000) 18-52.

[3] L. Rassaei, M. Amiri, C.M. Cirtiu, M. Sillanpaeae, F. Marken, M. Sillanpaeae, Nanoparticles in electrochemical sensors for environmental monitoring, Trac-Trends in Analytical Chemistry. 30 (2011) 1704-1715.

[4] I. Capek, Dispersions, novel nanomaterial sensors and nanoconjugates based on carbon nanotubes, Adv. Colloid Interface Sci. 150 (2009) 63-89.

[5] R. Sardar, A.M. Funston, P. Mulvaney, R.W. Murray, Gold Nanoparticles: Past, Present, and Future, Langmuir. 25 (2009) 13840-13851.

[6] J.M. Pingarron, P. Yanez-Sedeno, A. Gonzalez-Cortes, Gold nanoparticle-based electrochemical biosensors, Electrochim. Acta. 53 (2008) 5848-5866.

[7] D. Liu, Z. Wang, X. Jiang, Gold nanoparticles for the colorimetric and fluorescent detection of ions and small organic molecules, Nanoscale. 3 (2011) 1421-1433.

[8] S. Guo, E. Wang, Synthesis and electrochemical applications of gold nanoparticles, Anal. Chim. Acta. 598 (2007) 181-192.

[9] H. Jans, Q. Huo, Gold nanoparticle-enabled biological and chemical detection and analysis, Chem. Soc. Rev. 41 (2012) 2849-2866.

[10] M. Hu, J. Chen, Z. Li, L. Au, G.V. Hartland, X. Li, M. Marquez, Y. Xia, Gold nanostructures: engineering their plasmonic properties for biomedical applications, Chem. Soc. Rev. 35 (2006) 1084-1094.

[11] X. Huang, P.K. Jain, I.H. El-Sayed, M.A. El-Sayed, Gold nanoparticles: interesting optical properties and recent applications in cancer diagnostic and therapy, Nanomedicine. 2 (2007) 681-693.

[12] S. Link, M.A. El-Sayed, Shape and size dependence of radiative, non-radiative and photothermal properties of gold nanocrystals, International Reviews in Physical Chemistry. 19 (2000) 409-453.

[13] S. Wang, S. Fu, H. Ding, Determination of 5-Fluorouracil Using Disposable Gold Nanoparticles Modified Screen-Printed Electrode, Sensor Letters. 10 (2012) 974-978.

[14] Y. Lin, S. Chen, Y. Chuang, Y. Lu, T.Y. Shen, C.A. Chang, C. Lin, Disposable amperometric immunosensing strips fabricated by Au nanoparticles-modified screen-printed carbon electrodes for the detection of foodborne pathogen Escherichia coli O157 : H7, Biosens. Bioelectron. 23 (2008) 1832-1837.

[15] E. Bernalte, C.M. Sanchez, E.P. Gil, Gold nanoparticles-modified screen-printed carbon electrodes for anodic stripping voltammetric determination of

mercury in ambient water samples, Sensors and Actuators B-Chemical. 161 (2012) 669-674.

[16] X.H. Gao, W.Z. Wei, L. Yang, T.J. Yin, Y. Wang, Simultaneous determination of lead, copper, and mercury free from macromolecule contaminants by square wave stripping voltammetry, Anal. Lett. 38 (2005) 2327-2343.

[17] J.Z. James, D. Lucas, C.P. Koshland, Gold nanoparticle films as sensitive and reusable elemental mercury sensors, Environmental Science and Technology. 46 (2012) 9557-9562.

[18] E.C. Heider, K. Trieu, A.F.T. Moore, A.D. Campiglia, Portable mercury sensor for tap water using surface plasmon resonance of immobilized gold nanorods, Talanta. 99 (2012) 180-185.

[19] J. Homola, S.S. Yee, G. Gauglitz, Surface plasmon resonance sensors: review, Sensors and Actuators B-Chemical. 54 (1999) 3-15.

[20] Jinlong Chen, AiFang Zheng, AiHong Chen, Yingchun Gao, Chiyang He, Xiaoming Kai, Genhua Wu, Youcun Chen, A functionalized gold nanoparticles and Rhodamine 6G based fluorescent sensor for high sensitive and selective detection of mercury(II) in environmental water samples, Anal. Chim. Acta. 599 (2007) 134-142.

[21] S. Pyne, G.P. Sahoo, D.K. Bhui, H. Bar, P. Sarkar, A. Maity, A. Misra, FRET based ultra sensor for detection of Hg (II) in water: A comparative study using citrate and marcapto propanoic acid as stabilizer of AuNPs, Sensors and Actuators B-Chemical. 160 (2011) 1141-1148.

[22] A. Zheng, J. Chen, G. Wu, H. Wei, C. He, X. Kai, G. Wu, Y. Chen, Optimization of a sensitive method for the "switch-on" determination of mercury(II) in waters using Rhodamine B capped gold nanoparticles as a fluorescence sensor, Microchimica Acta. 164 (2009) 17-27.

[23] J. Polte, T.T. Ahner, F. Delissen, S. Sokolov, F. Emmerling, A.F. Thunemann, R. Kraehnert, Mechanism of gold nanoparticle formation in the classical citrate synthesis method derived from coupled in situ XANES and SAXS evaluation, J. Am. Chem. Soc. 132 (2010) 1296-1301.

[24] S.M. Reilly, T. Krick, A. Dass, Surfactant-free synthesis of ultrasmall gold nanoclusters, Journal of Physical Chemistry C. 114 (2010) 741-745.

[25] C. Li, D. Li, G. Wan, J. Xu, W. Hou, Facile synthesis of concentrated gold nanoparticles with low size-distribution in water: Temperature and pH controls, Nanoscale Research Letters. 6 (2011) 1-10.

[26] Y. Lei, H. Chen, H. Dai, Z. Zeng, Y. Lin, F. Zhou, D. Pang, Electroless-plated gold films for sensitive surface plasmon resonance detection of white spot syndrome virus, Biosens. Bioelectron. 23 (2008) 1200-1207.

[27] C. Klingshirn, ZnO: From basics towards applications, Physica Status Solidi B-Basic Solid State Physics. 244 (2007) 3027-3073.

[28] U. Ozgur, Y.I. Alivov, C. Liu, A. Teke, M.A. Reshchikov, S. Dogan, V. Avrutin, S.J. Cho, H. Morkoc, A comprehensive review of ZnO materials and devices, J. Appl. Phys. 98 (2005) 041301.

[29] M. Ahmad, J. Zhu, ZnO based advanced functional nanostructures: synthesis, properties and applications, Journal of Materials Chemistry. 21 (2011) 599-614.

[30] A.B. Djurisic, X. Chen, Y.H. Leung, A.M.C. Ng, ZnO nanostructures: growth, properties and applications, Journal of Materials Chemistry. 22 (2012) 6526-6535.

[31] D. Vanmaekelbergh, L.K. van Vugt, ZnO nanowire lasers, Nanoscale. 3 (2011) 2783-2800.

[32] S.K. Arya, S. Saha, J.E. Ramirez-Vick, V. Gupta, S. Bhansali, S.P. Singh, Recent advances in ZnO nanostructures and thin films for biosensor applications: Review, Anal. Chim. Acta. 737 (2012) 1-21.

[33] A. Wei, L. Pan, W. Huang, Recent progress in the ZnO nanostructure-based sensors, Materials Science and Engineering B-Advanced Functional Solid-State Materials. 176 (2011) 1409-1421.

[34] Zhou Xin, Yang Jian-Mao, Xin Meng, Chen Meng-Ni, Wang Xing, Liu Jian-Yun, Preparation of Electrospun ZnO-Carbon Composite Nanofiber Modified

Electrodes for the Detection of Trace Lead, Chinese Journal of Analytical Chemistry. 42 (2014) 985-990.

[35] N.Q. Wu, M.H. Zhao, J.G. Zheng, C.B. Jiang, B. Myers, S.X. Li, M. Chyu, S.X. Mao, Porous CuO-ZnO nanocomposite for sensing electrode of high-temperature CO solid-state electrochemical sensor, Nanotechnology. 16 (2005) 2878-2881.

[36] M.H. Asif, S.M.U. Ali, O. Nur, M. Willander, C. Brannmark, P. Stralfors, U.H. Englund, F. Elinder, B. Danielsson, Functionalised ZnO-nanorod-based selective electrochemical sensor for intracellular glucose, Biosens. Bioelectron. 25 (2010) 2205-2211.

[37] B. Gu, C. Xu, C. Yang, S. Liu, M. Wang, ZnO quantum dot labeled immunosensor for carbohydrate antigen 19-9, Biosens. Bioelectron. 26 (2011) 2720-2723.

[38] Y. Liang, C. Chang, C. Chen, Y. Chu-Su, C. Lin, Development of an Au/ZnO thin film surface plasmon resonance-based biosensor immunoassay for the detection of carbohydrate antigen 15-3 in human saliva, Clin. Biochem. 45 (2012) 1689-1693.

[39] L. Wang, Y. Sun, J. Wang, J. Wang, A. Yu, H. Zhang, D. Song, Water-soluble ZnO-Au nanocomposite-based probe for enhanced protein detection in a SPR biosensor system, J. Colloid Interface Sci. 351 (2010) 392-397.

[40] K.M. Byun, N. Kim, Y.H. Ko, J.S. Yu, Enhanced surface plasmon resonance detection of DNA hybridization based on ZnO nanorod arrays, Sensors and Actuators B-Chemical. 155 (2011) 375-379.

[41] V. Amendola, M. Meneghetti, Size evaluation of gold nanoparticles by UV-vis spectroscopy, Journal of Physical Chemistry C. 113 (2009) 4277-4285.

[42] K. Zabetakis, W.E. Ghann, S. Kumar, M. Daniel, Effect of high gold salt concentrations on the size and polydispersity of gold nanoparticles prepared by an extended Turkevich-Frens method, Gold Bulletin. 45 (2012) 203-211.

[43] W. Haiss, N.T.K. Thanh, J. Aveyard, D.G. Fernig, Determination of size and concentration of gold nanoparticles from UV-Vis spectra, Anal. Chem. 79 (2007) 4215-4221.

[44] S. Link, M. El-Sayed, Spectral Properties and Relaxation Dynamics of Surface Plasmon Electronic Oscillations in Gold and Silver Nanodots and Nanorods, J Phys Chem B. 103 (1999) 8410-8426.

[45] Y. Jin, X. Kang, Y. Song, B. Zhang, G. Cheng, S. Dong, Controlled nucleation and growth of surface-confined gold nanoparticles on a (3-aminopropyl)trimethoxysilane-modified glass slide: A strategy for SPR substrates, Anal. Chem. 73 (2001) 2843-2849.

[46] K.C. Grabar, K.J. Allison, B.E. Baker, R.M. Bright, K.R. Brown, R.G. Freeman, A.P. Fox, C.D. Keating, M.D. Musick, M.J. Natan, Two-dimensional arrays of colloidal gold particles: A flexible approach to macroscopic metal surfaces, Langmuir. 12 (1996) 2353-2361.

[47] J. Siegel, O. Lyutakov, V. Rybka, Z. Kolska, V. vorcik, Properties of gold nanostructures sputtered on glass, Nanoscale Research Letters. 6 (2011) 1-9.

[48] S.C. Padmanabhan, D. Ledwith, S.C. Pillai, D.E. McCormack, J.M. Kelly, Microwave-assisted synthesis of ZnO micro-javelins, Journal of Materials Chemistry. 19 (2009).

[49] S. Cho, S. Jung, K. Lee, Morphology-controlled growth of ZnO nanostructures using microwave irradiation: From basic to complex structures, Journal of Physical Chemistry C. 112 (2008) 12769-12776.

[50] S M Mahpeykar and J Koohsorkhi and,H.Ghafoori, Ultra-fast microwave-assisted hydrothermal synthesis of long vertically aligned ZnO nanowires for dye-sensitized solar cell application, Nanotechnology. 23 (2012) 165602.

[51] T.J. Jacobsson, T. Edvinsson, Absorption and Fluorescence Spectroscopy of Growing ZnO Quantum Dots: Size and Band Gap Correlation and Evidence of Mobile Trap States, Inorg. Chem. 50 (2011) 9578-9586.

[52] I. Bilecka, P. Elser, M. Niederberger, Kinetic and Thermodynamic Aspects in the Microwave-Assisted Synthesis of ZnO Nanoparticles in Benzyl Alcohol, ACS Nano. 3 (2009) 467-477.

[53] N. Shojaee, T. Ebadzadeh, A. Aghaei, Effect of concentration and heating conditions on microwave-assisted hydrothermal synthesis of ZnO nanorods, Mater Charact. 61 (2010) 1418-1423.

[54] S. Baset, H. Akbari, H. Zeynali, M. Shafie, Size measurement of metal and semiconductor nanoparticles via uv-vis absorption spectra, Dig. J. Nanomater. Biostruct. 6 (2011) 709-716.

[55] A. Wood, M. Giersig, M. Hilgendorff, A. Vilas-Campos, L. Liz-Marzan, P. Mulvaney, Size Effects in Zno: The Cluster to Quantum Dot Transition, 56 (2003) 1051-1057.

[56] H. Zeng, G. Duan, Y. Li, S. Yang, X. Xu, W. Cai, Blue luminescence of ZnO nanoparticles based on non-equilibrium processes: Defect origins and emission controls, Advanced Functional Materials. 20 (2010) 561-572.

[57] J.Q. Hu, X.L. Ma, Z.Y. Xie, N.B. Wong, C.S. Lee, S.T. Lee, Characterization of zinc oxide crystal whiskers grown by thermal evaporation, Chemical Physics Letters. 344 (2001) 97-100.

[58] S. Zhang, B. Cho, D. Lee, J. Lim, J. Huh, ZnO Nanorods, Nanotubes and Nanorings: Controlled Synthesis and Structural Properties, Journal of Nanoscience and Nanotechnology. 12 (2012) 1521-1525.

[59] X. Sun, H. Zhang, J. Xu, Q. Zhao, R. Wang, D. Yu, Shape controllable synthesis of ZnO nanorod arrays via vapor phase growth, Solid State Commun. 129 (2004) 803-807.

[60] B.J. Jin, S.H. Bae, S.Y. Lee, S. Im, Effects of native defects on optical and electrical properties of ZnO prepared by pulsed laser deposition, Materials Science and Engineering B-Solid State Materials for Advanced Technology. 71 (2000) 301-305.

[61] X. Wen, W. Wu, Y. Ding, Z.L. Wang, Seedless synthesis of patterned ZnO nanowire arrays on metal thin films (Au, Ag, Cu, Sn) and their application for flexible electromechanical sensing, J Mater Chem. 22 (2012) 9469-9476.

[62] H.E. Unalan, P. Hiralal, N. Rupesinghe, S. Dalal, W.I. Milne, G.A.J. Amaratunga, Rapid synthesis of aligned zinc oxide nanowires, Nanotechnology. 19 (2008) 255608.

[63] J. Liu, J. She, S. Deng, J. Chen, N. Xu, Ultrathin seed-layer for tuning density of ZnO nanowire arrays and their field emission characteristics, J. Phys. Chem. C. 112 (2008) 11685-11690.

[64] H. Armannsson, Use of Dithizone Extraction and Atomic-Absorption Spectrometry for Determination of Cadmium, Zinc, Copper, Nickel and Cobalt in Rocks and Sediments, Anal. Chim. Acta. 88 (1977) 89-95.

[65] J. Chwastowska, W. Skwara, E. Sterlinska, L. Pszonicki, Determination of platinum and palladium in environmental samples by graphite furnace atomic absorption spectrometry after separation on dithizone sorbent, Talanta. 64 (2004) 224-229.

[66] J. Lee, Y. Ryu, J. Park, S. Jeon, S. Kim, Y. Kim, Determination of methylmercury in biological samples using dithizone extraction method followed by purge trap GC-MS, B. Kor. Chem. Soc. 28 (2007) 2293-2298.

[67] G. Cheng, M. He, H. Peng, B. Hu, Dithizone modified magnetic nanoparticles for fast and selective solid phase extraction of trace elements in environmental and biological samples prior to their determination by ICP-OES, Talanta. 88 (2012) 507-515.

[68] E. Woznica, M.M. Wojcik, M. Wojciechowski, J. Mieczkowski, E. Bulska, K. Maksymiuk, A. Michalska, Dithizone modified gold nanoparticles films for potentiometric sensing, Anal. Chem. 84 (2012) 4437-4442.

[69] A. Safavi, M. Bagheri, Design and characteristics of a mercury (II) optode based on immobilization of dithizone on a triacetylcellulose membrane, Sensor Actuat. B-Chem. 99 (2004) 608-612.

[70] B.D. Ozturk, H. Filik, E. Tutem, R. Apak, Simultaneous derivative spectrophotometric determination of cobalt(II) and nickel(II) by dithizone without extraction, Talanta. 53 (2000) 263-269.

[71] R. Litman, E.T. Williams, H.L. Finston, Extraction of Mercury by Dithizone and Stability of Extracted Complex, Anal. Chem. 49 (1977) 983-987.

[72] W.E. White, Dithizone as an analytical reagent, J. Chem. Educ. 13 (1936) 369.

[73] M. Mahmoud, A. Elgaber, A. Elroudi, E. Soliman, More Light on the Low Electronic-Transition Energy-Bands of Dithizone, Spectroc. Acta Pt. A-Molec. Biomolec. Spectr. 43 (1987) 1281-1285.

[74] J. Fabian, G. Roebisch, R. Noeske,
MO-LCAO calculations on polymethines: XXIII-the origin of the absorption colour of dithizone and related compounds, Dyes and Pigments. 8 (1987) 165-177.

[75] G. Vasiyarov, S. Ananchenko, Isopropyl-Alcohol as a Hydrogen Donor in Catalytic Reduction of Unsaturated Steroid Compounds, B. Acad. Sci. Ussr Ch+. 23 (1974) 2571-2572.

[76] M. Fadly, M. Dawy, Effect of gamma radiation on the electronic spectra of poly(methylmethacrylate) doped with some divalent nd10-cation dithizone, Phys. Scripta. 51 (1995) 126-126.

[77] T. Schönherr, V. Schmid, R. Linder, M.F.R. Fouda, R.S. Amin, S.A. Mostafa, Synthesis, absorption spectra and semiempiric calculations on the photochromism of arylmercuric dithizonate complexes, Int. J. Photoenergy. 1 (1999) 197-202.

[78] M.S. Searle, G.J. Sharman, P. Groves, B. Benhamu, Enthalpic (electrostatic) contribution to the chelate effect: a correlation between ligand binding constant and a specific hydrogen bond strength in complexes of glycopeptide antibiotics with cell wall analogues, J. Chem. Soc. , Perkin Trans. 1. (1996) 2781-2786.

[79] Y. Leng, Y. Li, A. Gong, Z. Shen, L. Chen, A. Wu, Colorimetric response of dithizone product and hexadecyl trimethyl ammonium bromide modified gold nanoparticle dispersion to 10 types of heavy metal ions: Understanding the

involved molecules from experiment to simulation, Langmuir. 29 (2013) 7591-7599.

[80] M. Beija, C.A.M. Afonso, J.M.G. Martinho, Synthesis and applications of Rhodamine derivatives as fluorescent probes, Chem. Soc. Rev. 38 (2009) 2410-2433.

[81] H.N. Kim, M.H. Lee, H.J. Kim, J.S. Kim, J. Yoon, A new trend in rhodamine-based chemosensors: application of spirolactam ring-opening to sensing ions, Chem. Soc. Rev. 37 (2008) 1465-1472.

[82] J. Ni, Q. Li, B. Li, L. Zhang, A novel fluorescent probe based on rhodamine B derivative for highly selective and sensitive detection of mercury(II) ion in aqueous solution, Sensors and Actuators B-Chemical. 186 (2013) 278-285.

[83] S. Saha, P. Mahato, U.G. Reddy, E. Suresh, A. Chakrabarty, M. Baidya, S.K. Ghosh, A. Das, Recognition of Hg2+ and Cr3+ in Physiological Conditions by a Rhodamine Derivative and Its Application as a Reagent for Cell-Imaging Studies, Inorg. Chem. 51 (2012) 336-345.

[84] Y. Xiang, A. Tong, P. Jin, Y. Ju, New fluorescent rhodamine hydrazone chemosensor for Cu(II) with high selectivity and sensitivity, Org. Lett. 8 (2006) 2863-2866.

[85] Z. Yang, M. She, B. Yin, J. Cuo, Y. Zhang, W. Sun, J. Li, Z. Shi, Three Rhodamine-Based "Off-On" Chemosensors with High Selectivity and Sensitivity for Fe3+ Imaging in Living Cells, J. Org. Chem. 77 (2012) 1143-1147.

[86] Y. Zhou, J. Zhang, L. Zhang, Q. Zhang, T. Ma, J. Niu, A rhodamine-based fluorescent enhancement chemosensor for the detection of Cr3+ in aqueous media, Dyes and Pigments. 97 (2013) 148-154.

[87] X. Cao, F. Shen, M. Zhang, J. Guo, Y.L. Luo, J. Xu, Y. Li, C. Sun, Highly sensitive detection of melamine based on fluorescence resonance energy transfer between rhodamine B and gold nanoparticles, Dyes and Pigments. 111 (2014) 99-107.

[88] J. Xu, Y. Li, J. Guo, F. Shen, Y. Luo, C. Sun, Fluorescent detection of clenbuterol using fluorophore functionalized gold nanoparticles based on fluorescence resonance energy transfer, Food Control. 46 (2014) 67-74.

[89] H. Cai, H. Wang, J. Wang, W. Wei, P. Yang, J. Cai, Naked eye detection of glutathione in living cells using rhodamine B-functionalized gold nanoparticles coupled with FRET, Dyes and Pigments. 92 (2012) 778-782.

[90] D.S. Tira, M. Focsan, S. Ulinici, D. Maniu, S. Astilean, Rhodamine B-Coated Gold Nanoparticles as Effective "Turn-on'' Fluorescent Sensors for Detection of Zinc II Ions in Water, Spectroscopy Letters. 47 (2014) 153-159.

[91] F.L. Arbeloa, T.L. Arbeloa, M.J.T. Estevez, I.L. Arbeloa, Photophysics of Rhodamines - Molecular-Structure and Solvent Effects, J. Phys. Chem. 95 (1991) 2203-2208.

[92] F.M. Zehentbauer, C. Moretto, R. Stephen, T. Thevar, J.R. Gilchrist, D. Pokrajac, K.L. Richard, J. Kiefer, Fluorescence spectroscopy of Rhodamine 6G: Concentration and solvent effects, Spectrochimica Acta Part A-Molecular and Biomolecular Spectroscopy. 121 (2014) 147-151.

[93] F.L. Arbeloa, P.R. Ojeda, I.L. Arbeloa, Fluorescence Self-Quenching of the Molecular-Forms of Rhodamine-B in Aqueous and Ethanolic Solutions, J Lumin. 44 (1989) 105-112.

[94] M.J. Snare, F.E. Treloar, K.P. Ghiggino, P.J. Thistlethwaite, The Photophysics of Rhodamine-B, Journal of Photochemistry. 18 (1982) 335-346.

[95] M. Stobiecka, M. Hepel, Multimodal coupling of optical transitions and plasmonic oscillations in rhodamine B modified gold nanoparticles, Physical Chemistry Chemical Physics. 13 (2011) 1131-1139.

[96] J. Zhu, K. Zhu, L. Huang, Using gold colloid nanoparticles to modulate the surface enhanced fluorescence of Rhodamine B, Physics Letters a. 372 (2008) 3283-3288.

[97] H. Liu, H. Maruyama, T. Masuda, A. Honda, F. Arai, Multi-fluorescent micro-sensor for accurate measurement of pH and temperature variations in micro-environments, Sensors and Actuators B-Chemical. 203 (2014) 54-62.

[98] Z. Wang, X. Ma, S. Zong, Y. Wang, H. Chen, Y. Cui, Preparation of a magnetofluorescent nano-thermometer and its targeted temperature sensing applications in living cells, Talanta. 131 (2015) 259-265.

Chapter 3

Investigations on Optical Sensor Development

3 Investigations on Optical Sensor Development

3.1 Introduction

Several novel approaches have been reported for the field detection of heavy metal ions such as label-free colorimetric detection [1], fluorescent probe [2], fluorescent resonance energy transfer based ratiometric sensor [3], electrochemical [4], surface plasmon resonance [5], chronocoulometry [6], protein-directed fluorescent Ag cluster [7], magnetic oligonucleotide probes [8] and fibre optic biosensor [9]. Among these novel detection approaches, in particular, fibre optic sensors are of interest for this research. Optical fibre sensors offer a number of distinct and unique advantages such as they are immune to electromagnetic interference, small in size, usually made from chemically inert materials, allows real-time, remote, continuous and multi-point detection, and are suitable do deploy in harsh environments. These inherent properties make them suitable for environmental monitoring applications.

Recent developments on fibre optic sensors to detect heavy metal ions include modal interferometer [10], surface plasmon resonance [11,12], calix(4)rene-based [13], fluorescence based [9,14], DNA-based [15], Al_2O_3 nanoparticles based [16] and enzyme based [17] sensors. Most of these sensors have been reported to detect sub-micromolar concentrations with fast response times but lack in procedural simplicity and selectivity. Among these sensors, use of a single wavelength for detecting multiple metal ions, especially, based on absorption are known to be highly susceptible to interference and lacks selectivity [13]. Fibre optic sensors based on refractive index changes also lacks in specificity with metal ions [10-13].

One of the optical fibre sensing methods is based on evanescent waves, where light propagating along the fibre generates the evanescent waves at the near surface region of the fibre core [18]. These waves are highly susceptible to the changes in the surrounding medium [13]. This chapter reports investigations on the development of an evanescent wave based optical fibre sensor using dithizone to detect heavy metal ions in the aqueous environment. First part of the chapter discusses the basic theory of an optical fibre and the study of various fibre optic parameters relevant to the evanescent wave based sensor development, suitability of dithizone as a sensitive and selective reagent for evanescent wave based heavy metal ion detection, investigations on environmental parameters such as pH and concentrations and their effects on the detection, dithizone immobilization on the fibre surface and sensor development. Second part reports various investigations on sensitivity enhancement using new geometric design through simulation and experimental work.

3.2 Theoretical Background

Optical fibre is a physical medium through which light can propagate, analogous to the current flowing through a conductor (electrical wire). Figure 3.1 illustrates the light propagation through an optical fibre via total internal reflections. The refractive index of core and cladding are n_1 and n_2 respectively, where $n_1>n_2$.

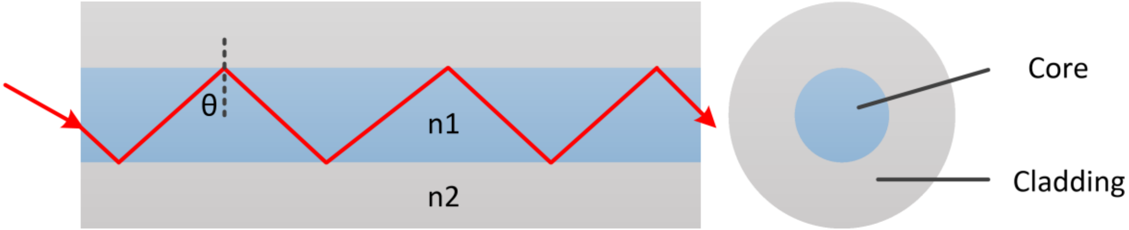

Figure 3.1 Schematic of light propagation through an optical fibre.

The refraction and reflection phenomena of the light at a core-cladding interface in an optical fibre are illustrated in Figure 3.2. When the angle of incidence of light at the core-cladding interface is greater than the critical angle (defined by the Snell's law), light is reflected else refracted. Snell's law relating the refractive indices of core and cladding (n_1 and n_2 respectively) with critical angle (θ_c) is defined as (eq. (3.1)) [19]:

$$\sin\theta_c = \frac{n_2}{n_1} \qquad \text{...eq. (3.1)}$$

The critical angle is the required minimum angle of incidence for the total internal reflection (TIR) to occur and hence, to guide the light in the core. Light propagates in the fibre through TIR and undergoes many reflections before arriving at the other end.

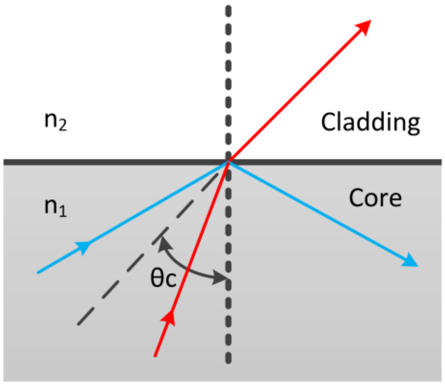

Figure 3.2 Light refraction and total internal reflection at the core-cladding interface.

An EM planar wave travelling in a medium with refractive index *n* can be expressed as (eq. (3.2)) [20],

$$E = E_0 exp(j\omega t - jk \cdot r) = E_0 exp\left(j\omega t - jk_x x - jk_y y - jk_z z\right) \qquad \text{... eq. (3.2)}$$

where, E_0 is the magnitude of EM field, ω is the angular frequency, *j* is the complex number; *k* and *r*, are wave and position vector, respectively.

The wave vector *k* can be expressed as (eq. (3.3)) [20],

$$k = \sqrt{{k_x}^2 + {k_y}^2 + {k_z}^2} = \frac{2\pi n}{\lambda} = \frac{n\omega}{c} \qquad \text{... eq. (3.3)}$$

Where, λ and *c* are the wavelength and velocity of propagating light in the vacuum, n is the refractive index and k_x, k_y and k_z are the wave vectors in the *x*, *y* and *z* directions respectively.

Now, consider the case, where this travelling wave approaches the interface of two materials with refractive index n_1 and n_2 as shown in Figure 3.3, where the angle of incidence and refraction are α and β respectively. Applying the Snell's law, we have (eq. (3.4)) [20]:

$$n_1 \sin\alpha = n_2 \sin\beta \qquad \text{... eq. (3.4)}$$

Here, considering the 2D interface, where, $k_z = 0$ and $k_{1x} = k_{2x} = k_x$

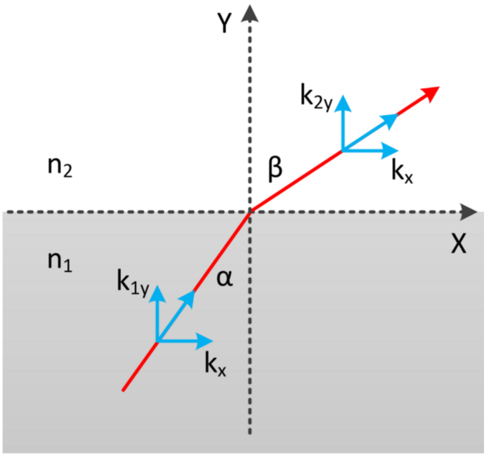

Figure 3.3 Light refraction at the interface of two materials.

Substituting and equating equation (3.2) and (3.3), the k_{2y} component of the propagation vector can be given by (eq. (3.5)) [20],

$$k_{2y}{}^2 = n_1{}^2 \left(\frac{2\pi}{\lambda}\right)^2 \left(\frac{n_2{}^2}{n_1{}^2} - sin^2\alpha\right) \qquad \text{… eq. (3.5)}$$

Assume that $n_1 > n_2$, k_{2y} becomes imaginary when sin$\alpha > n_2/n_1$. This indicates that the EM field becomes evanescent. Substituting these conditions into the equation (3.2), the EM field in the medium 2 can be expressed as (eq. (3.6)) [20],

$$E_2 = E_0 e^{-\kappa_{2y} y} exp(j\omega t - jk_x x) \qquad \text{… eq. (3.6)}$$

The expression means that electric field decays exponentially in the medium 2 perpendicular to the interface but a travelling wave exists in x direction bound to the interface. The magnitude of decaying electric field is given by $1/\kappa_{2y} \Xi 1/jk_{2y}$ and is referred to as an evanescent field.

The penetration depth dp, $(=1/jk_{2y})$ of the evanescent field is defined as the distance at which the strength of electric field decays to its "1/e" value and is given by (eq. (3.7)) [18],

$$dp = \frac{\lambda}{2\pi n_1 \sqrt{sin^2\alpha - \frac{n_2{}^2}{n_1{}^2}}} \qquad \text{… eq. (3.7)}$$

where, n_1 and n_2 are the refractive indices of the core and cladding, α is the internal incidence angle normal to the core-cladding interface and λ is the wavelength of light. Figure 3.4 shows the variation of evanescent field penetration depth (*dp*) calculated at 485 nm for n_1 = 1.46, n_2 =1.33 for a range of incidence angles. Calculated critical angle was 65.64 degree. Penetration depth obtained with the above parameters was about 2 μm near the critical angle. It was observed that the *dp* increases sharply in less than a degree change of incidence angle just above the critical angle. This result suggests that in a single mode fibre, higher sensitivity can be achieved by carefully launching the light at an incidence angle close to the critical angle. The calculated results were based on the assumption that refractive indices of the materials are constant in the visible range, but the fact that it varies with the wavelength.

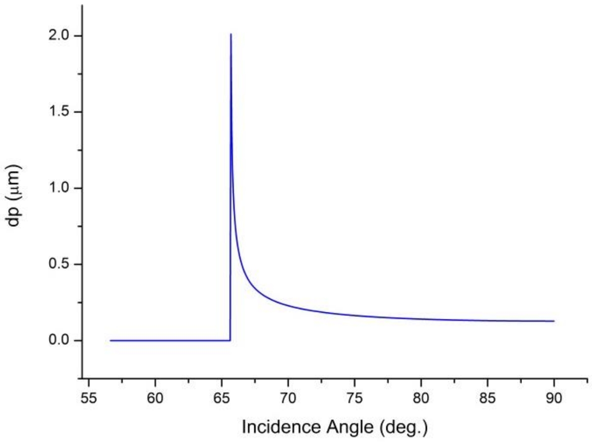

Figure 3.4 shows the evanescent field penetration depth (dp) with incidence angle.

To understand the effect of a change in refractive index of the fibre material with wavelength, the same calculation was extended for different visible wavelengths for a PMMA fibre. Figure 3.5 shows the refractive index and critical angle variation over a visible wavelength range for PMMA fibre calculated using Sellmeier equation [21]. Reduction in refractive index with increasing wavelength causes the increase in the critical angle due to the constant value of refractive index of water considered for the calculations. The refractive index of PMMA decreases with increasing wavelength. Reduction in refractive index causes an increase in penetration depth of the evanescent wave (eq.3.7). Therefore, to study the effect of wavelength on the penetration depth, *dp* was calculated for a range of incidence angles and at λ = 400, 500, 600 and 700 nm as shown in Figure 3.6.

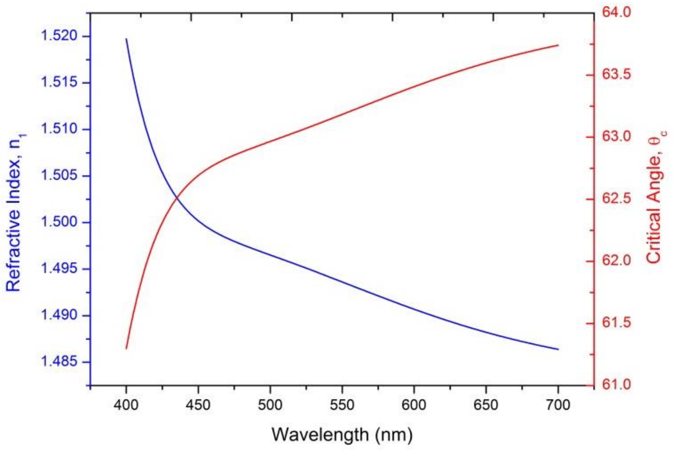

Figure 3.5 Refractive index and critical angle variation of PMMA fibre with wavelength over 400-700 nm.

It is observed that the *dp* increases from 0.20 to 1.70 μm as the wavelength increases from 400 to 700 nm. These results suggest that the sensitivity depends on the wavelength of incident light, refractive index of an optical fibre, refractive index of an aqueous medium and also, on the physical geometry such as the fibre diameter and interaction length.

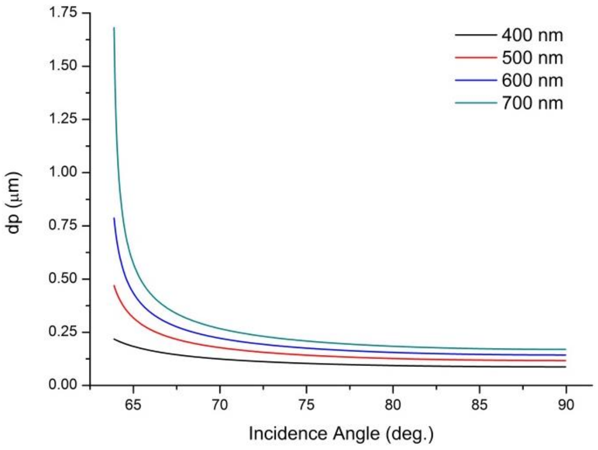

Figure 3.6 Evanescent wave penetration depth (dp) variation with wavelength for a range of incidence angles.

When a light of intensity I_0 incident on a cell of path length *l*, comprising absorption medium with molar absorption coefficient α_m, the output intensity I can be expressed using the Beer-Lambert law (as shown in Figure 3.7) [22]:

$$I = I_0\, exp(-\alpha_m l C) \qquad \text{… eq. (3.8)}$$

where, *C* is the concentration of the absorbing species.

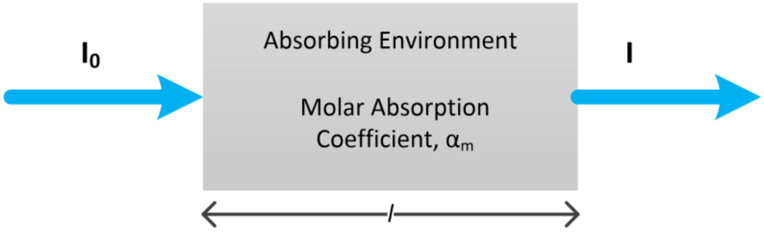

Figure 3.7 Light absorption through a cell using Beer-Lambert law.

As discussed, light propagating through the fibre generates an evanescent field in the cladding. This exponentially decaying evanescent field in the cladding region can be exposed to the surrounding environment by removal of the cladding. Thus, the evanescent field in the uncladded region of the fibre changes with the surroundings. If the evanescent wave penetrates into the absorbing medium surrounding the fibre core, the energy carried by the evanescent wave will be absorbed. Referring back to the previous absorption cell (Figure 3.7) which describes the direct absorption, a similar equation (eq. (3.9)) can be expressed for the evanescent wave based absorption medium for a fibre optic waveguide, with a term referred to as effective attenuation coefficient γ [22],

$$I = I_0\, exp(-\gamma l C) = I_0\, exp\big(-(\alpha_m r_f) l C\big) \quad \text{... eq. (3.9)}$$

where, $\gamma = \alpha_m r_f$ and r_f refers the reduction factor ($r_f < 1$) in the attenuation coefficient. Reduction factor r_f can be expressed as (eq. (3.10)) [22]:

$$r_f = \frac{n_r}{n_e}\eta \quad \text{... eq. (3.10)}$$

where, n_r is the real part of the refractive index of absorbing species, n_e is the effective refractive index of the guided wave ($n_e = n_1 sin\theta$), and η is the fraction of the total power launched into the fibre that interacts with the absorbing environment.

Based on above expressions, it can be concluded that, in the case of evanescent wave absorption based sensors, sensitivity depends on the fibre geometry such as diameter, interaction length and other parameters such as incidence angle, critical angle, wavelength of light, refractive index of core and cladding and molar absorption coefficient of analyte.

3.3 Feasibility Study on Evanescent Wave based Sensing

3.3.1 Background

Interactions between dithizone and metal ions have been already discussed in chapter 2. Briefly, metal ions adsorb on the binding sites formed by apex S and N atoms of the dithizone and by removal of hydrogen atom dithizone forms the metal dithizonates [23]. This binding process leads to a change in the absorption spectrum of dithizone, explained in chapter 2. This change in the absorption spectrum of dithizone can be monitored using uncladded fibre based on the evanescent wave absorption phenomenon as discussed in theory. Therefore, a very simple strategy has been adopted to develop the fibre optic heavy metal ion sensor. As mentioned earlier, light propagating along the fibre generates the evanescent waves at the near surface region of the fibre core [18]. Upon removal of the cladding, they can be exposed to the aqueous environment. Any change in the absorption property of the aqueous medium surrounding the uncladded fibre can lead to a change in transmitted signal. Therefore, a polymer multimode fibre with the uncladded sensing region has been used as a sensor to detect the heavy metal ions in aqueous solutions. This evanescent wave spectroscopy based detection strategy using dithizone offers increased specificity from other contaminants in the aqueous environment compared to the single wavelength detection approaches.

3.3.2 Detection Principle

The detection principle is the same as stated for the metal ions in chapter 2. The chemical structure of a dithizone is shown in Figure 3.8(a). Copper ion forms copper dithizonate by complexing with dithizone as shown in Figure 3.8(b) which causes the change in the absorption spectrum of dithizone, as shown in Figure 3.8(c). This change leads to the change in evanescent field absorption of the light propagating through the fibre leading to change in transmitted signal.

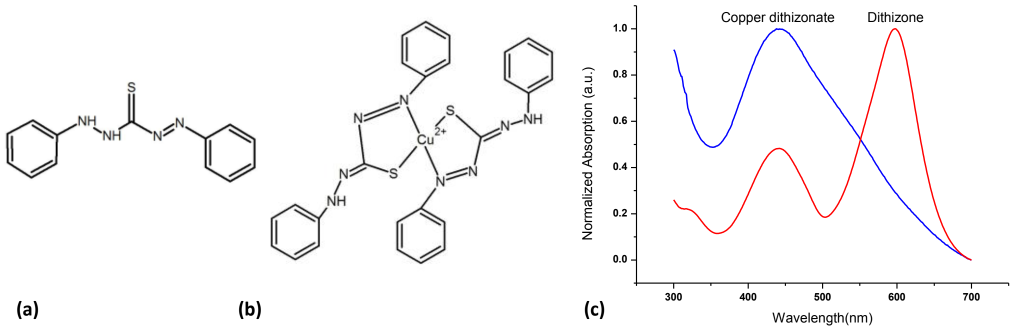

Figure 3.8 (a) Chemical structure of dithizone and (b) copper dithizonate. (c) Normalized absorption spectra of dithizone and copper dithizonate.

3.3.3 Chemicals

Analytical grade dithizone, 2-propanol, mercury, copper and chromium ion standard solutions were purchased from Sigma-Aldrich, UK and used without any further purification.

3.3.4 Experimental Setup

A simple experimental setup of the fibre optic sensor is shown in Figure 3.9(a). A white light LED (400-700 nm) from Electrospell Ltd was used as light source and the light was coupled to the fibre through an LED-Fibre coupler. For easier light coupling and detection, a multimode polymer fibre of 1 mm core diameter was used. Commercial optical fibre stripper and cutter were used to remove the cladding (6 cm in length) of an optical fibre. This unclad fibre was fixed inside the custom made sample cell and exposed to the aqueous solutions throughout the experiment. Concentrations of the metal ions were made from the metal ion standards and added to the dithizone solution to form the metal dithizonates. The optical signal transmitted through the fibre has been detected using a Stellarnet (EPP2000C) spectrometer at an integration time of 400 ms at room temperature. For each sample three spectra (each averaged over three) were collected which allows averaging possible intensity fluctuations from the LED source. Interaction of dithizone with metal ions was characterised using UV/Vis absorption spectroscopy. A Perkin Elmer (Lambda 900) UV/Vis absorption spectrometer was used for characterization and comparison/calibration of the aqueous samples. A custom made sample cell (as shown in Figure 3.9(b)) was used for holding the samples during measurements and was cleaned after each measurement using deionised water.

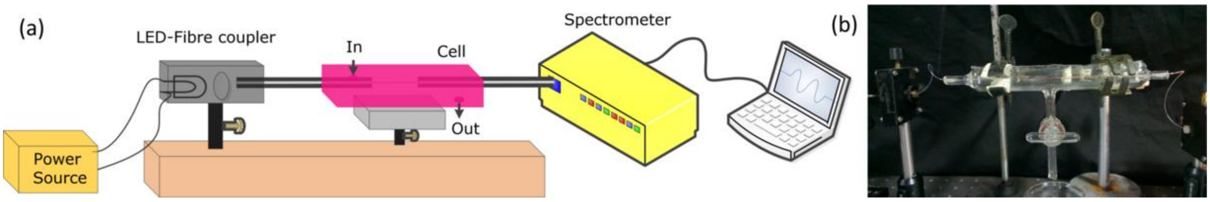

Figure 3.9 A schematic view of the experimental setup (a) and a picture of the custom made sample cell (b).

3.4 Results and Discussions

Absorption study of mercury dithizonates at various mercury ions concentration were carried out using UV-Vis absorption spectrometer by keeping the mercury dithizonate solution in a standard quartz cuvette (1 cm path-length). Figure 3.10(a) shows the mercury dithizonate absorbance trend for various concentrations of mercury ions measured at peak wavelength 490 nm. Absorption increases linearly with the concentration of mercury ions following the Beer-Lambert’s Law. A similar experiment was carried out with the developed fibre optic sensor, where a mercury dithizonate solution was entered into the sample cell and a change in output signal from the spectrometer was recorded at the peak wavelength of mercury dithizonates (490 nm). Figure 3.10(b) shows the trend of the output signal (I) over the reference signal (I_{ref}) with mercury ions concentration where the signal from water was considered as a reference signal. The measured output signal in the spectrometer decreases exponentially with an increase in mercury ion concentration. The observed decrease in output signal can be attributed to the evanescent absorption, as discussed in the theory (section 3.2). Briefly, an increase in the mercury ion concentration causes an increase in the bulk absorption of the mercury dithizonates which leads to an increase in the evanescent absorption and as a result of that transmitted signal decreases.

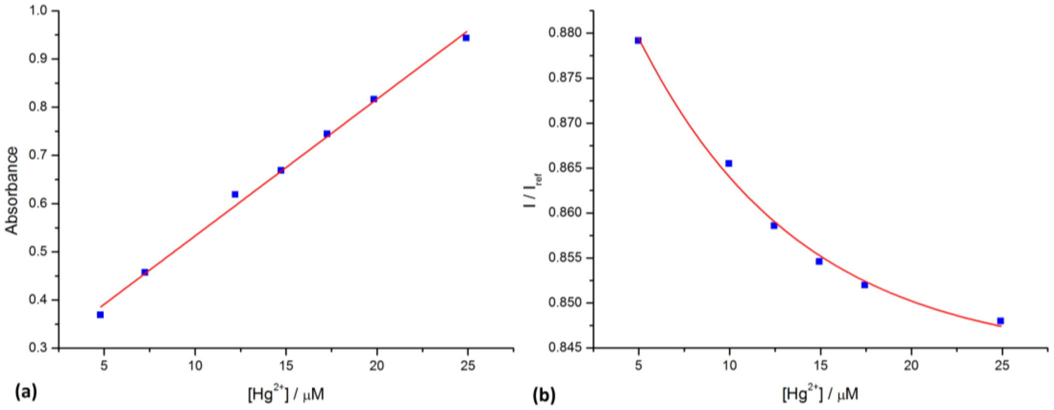

Figure 3.10 (a) Mercury dithizonate absorbance trend and (b) output signal trend from fibre optic sensor with mercury ions concentration.

3.4.1 Metal ions Selectivity

The spectral response of copper, chromium and mercury ions with dithizone (78 μM) was evaluated with 1 μg/ml concentration of each and the corresponding normalized absorption spectra are shown in the Figure 3.11. The absorption peak observed for chromium, copper and mercury dithizonate were at 530, 438 and 490 nm respectively. The peak absorption wavelength of mercury ions was 40 and 52 nm away from the peak absorption wavelength of chromium and copper ions respectively. The wide spectral shift ($\Delta\lambda_{max}$) for copper and chromium ions evades the spectral overlap issues and enables the selective detection of each using principle component analysis (PCA) [24,25].

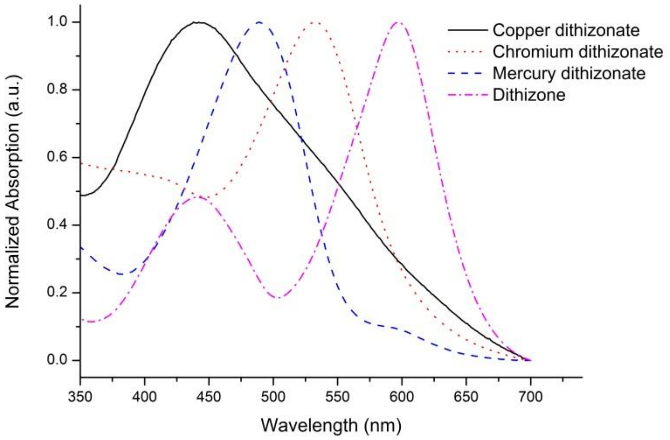

Figure 3.11 Normalized absorption spectra of 1 μg/ml mercury, copper and chromium dithizonate in an aqueous solution.

As discussed, the deformation in HOMO of the dithizone, due to the chelation with metal ions, strongly depends on the electrostatic interaction of metal ions with dithizone. The electrostatic force exerted by the metal ions on the electron cloud in HOMO depends on the electronegativity of metal ions. The electronegativity of mercury, copper and chromium is 2.00, 1.90 and 1.66 respectively. Therefore, the electrostatic force exerted by these metal ions on electron cloud in HOMO is different, henceforth; the change in electron energy levels of dithizone is different. Further, because of this effect, we observe the shift in the absorption band for the mercury, copper and chromium dithizonates. If we follow the influence of electronegativity of atoms on the peak wavelength shift, chromium should give a higher peak wavelength shift compared to copper, but that is not the case. There are other parameters which affect the electron energy levels, the first and most important one is the dithizone structure, which modifies it to lower its energy, and also the enthalpy and entropy of the system [26] and activity of the water/solvent [27]. Therefore, the whole effect is responsible for the different wavelength shift and binding affinity shown by metal ions to the dithizone.

In the same way, copper and chromium ion detection were carried out using the fibre optic sensor. Trends of I/I_{ref} for copper and chromium dithizonates measured at 438 and 530 nm respectively for various concentrations are shown in Figure 3.12 (a) and (b). The trends were similar to the trend observed with mercury ions. The difference observed in the slope of the trends can be attributed to the difference in binding affinity of the mercury, copper and chromium ions with dithizone.

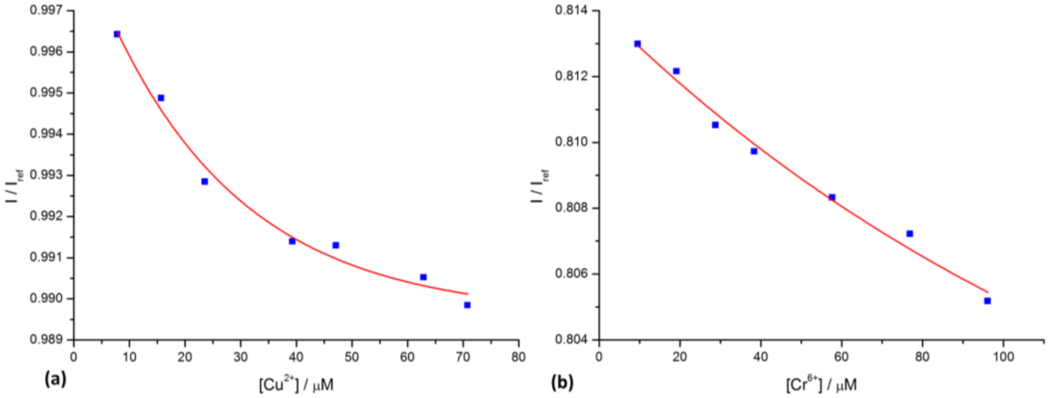

Figure 3.12 Output signal trend from the fibre optic sensor measured for (a) copper and (b) chromium ions with their respective concentrations.

3.4.2 Multi-ion Detection

Simultaneous detection of copper and chromium ions along with mercury ions was evaluated by mixing the copper and chromium ions with mercury ions prior to adding the chelating agent dithizone. Absorbance spectra of dithizone (78 µM) in the presence of mercury, mercury and copper, mercury and chromium ions are shown in Figure 3.13. As discussed, due to the stronger binding affinity of mercury, even in the presence of other metal ions, a strong mercury dithizonate peak can be seen. Table 3.1 shows the analysis of each peak.

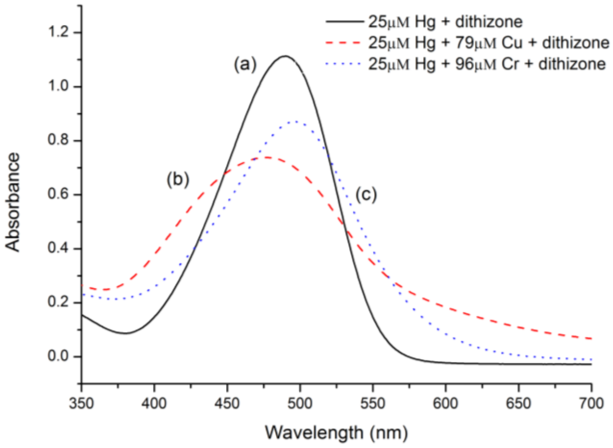

Figure 3.13 Absorbance spectra of metal dithizonates in an aqueous solution.

In the presence of copper ions, the mercury dithizonate absorption peak shifted to 478 nm, while in the presence of chromium ions, the absorption peak shifts to 498 nm. The full-width half maximum data indicates the peak broadening in the presence of copper and chromium ions. The larger value of the area under the peak (b) and (c) indicates that even after 25 µM of mercury ions are consumed in chelating with dithizone, there are still some binding sites available. As the copper ions have the next higher binding affinity after mercury ions, the few binding sites which are left are then used by the copper ions in chelation. Therefore, the reduction in available binding sites for the mercury ions cause the reduction in absorption peak height and introduction of copper dithizones cause the peak broadening. A similar effect can be seen for the chromium ion. The difference observed in the peak height was due to the lower binding affinity of chromium ions. Observed full width half maximum (FWHM) for peak (b) is higher than the peak (c) because the wavelength shift ($\Delta\lambda_{max}$) of copper dithizonate is higher than the chromium dithizonate with respect to the peak wavelength of mercury dithizonate. The higher FWHM value observed for peak (b) and peak (c) compared to peak (a) and shift of the central wavelength both support the detection of copper and chromium ions along with mercury ions simultaneously.

Table 3.1 Absorption peak analysis of metal dithizonate.

Peak	Area	FWHM	Central	Height
(a) Hg	103.21	85.28	490.00	1.08
(b) Cu + Hg	127.28	119.46	478.00	0.54
(c) Cr + Hg	114.13	97.87	498.00	0.75

These results indicate that a lower concentration of interfering metal ions may not affect the mercury ion detection due to the strong binding affinity of mercury. In a similar way, detection of copper and chromium ions may not be affected if a very low concentration of mercury ions are present. Also, the analysis based on the area under the peak indicates the probability of simultaneous detection of other metal ions by increasing the binding sites. Effect of other interfering metal ions such as cadmium, nickel, arsenic, zinc and lead on the detection of mercury has been studied using absorption spectra (results shown in Figure 3.14) and found that mercury has the highest binding affinity with the dithizone amongst all other interfering metal ions.

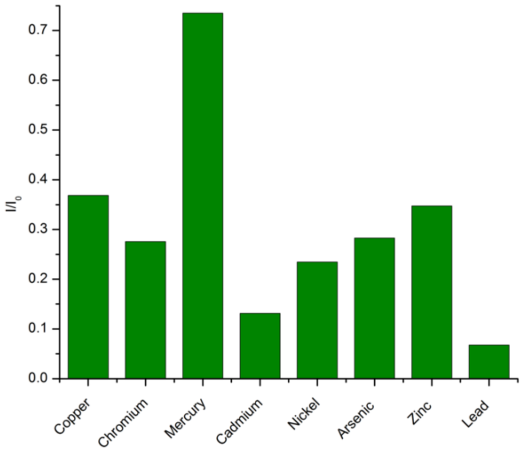

Figure 3.14 Change in peak absorption of various metal dithizonates (1 ppm each) over dithizone absorption spectrum.

3.4.3 Extension of Dynamic Detection Range

To extend the dynamic range of the sensor, intensity variation of mercury dithizonate absorbance peak, for 25 nM-100 μM mercury ions, was studied. Figure 3.15(a) shows the corresponding intensity variations. To better understand the observed nonlinear trend, the effect of dithizone to mercury ions concentration was studied. Absorbance spectra were recorded for a range of ratios of dithizone to mercury ions concentrations ($[C]_{dithizone}$:$[C]_{Hg}$) as shown in Figure 3.15(b). Results indicate that ratios in the range of 1:2 to 1:5 provide the optimum value for mercury ion detection.

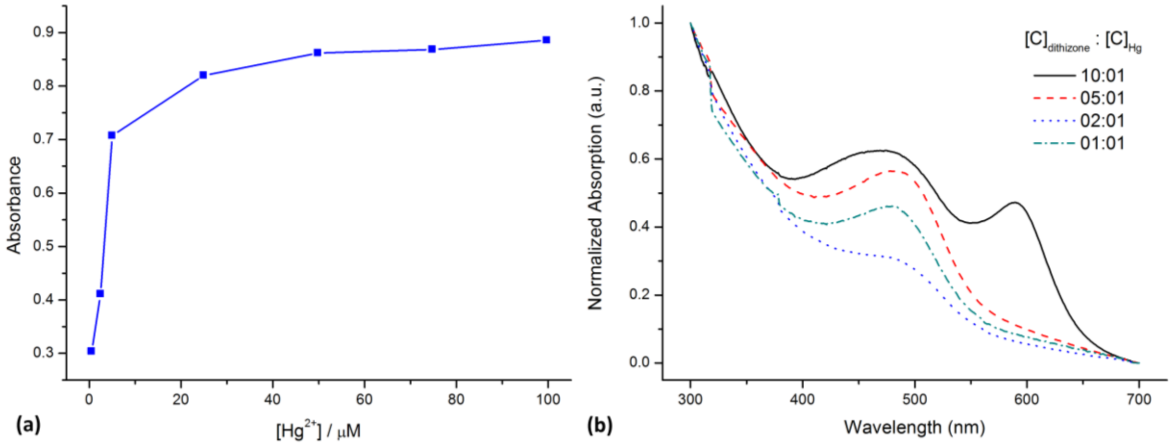

Figure 3.15 (a) Absorbance trend of mercury dithizonates at 490 nm with varying concentration of mercury ions and (b) absorption spectra of 2.5 μM mercury ions with different dithizone concentrations.

Further, the effect of pH on the peak absorbance of mercury dithizonate was studied by varying the pH from 4 to 9 of a solution using nitric acid and ammonium hydroxide. Figure 3.16 shows the effect of pH on the mercury dithizonate peak absorbance measured at 490 nm. The higher absorption observed at pH 6 can be attributed to the availability of maximum binding sites for chelation. A similar effect was observed by Benounis et al. [13] for the calix(4)arene molecule. The adsorption site formed by S-C-N-N atoms was protonated by H^+ ions in highly acidic solutions while in the case of pH > 6, the formation of mercury hydroxide occurs which may result in a lower absorption.

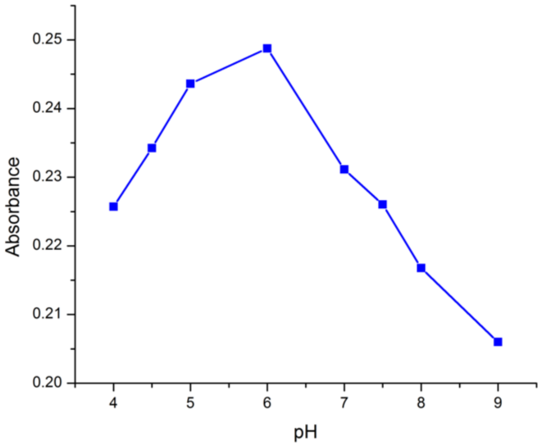

Figure 3.16 Mercury dithizonate absorbance trend measured at the peak absorption wavelength with pH varying from 4 to 9.

These results indicate that the two major contributors to the observed nonlinear absorbance trend are pH and the dithizone:mercury ion concentration ratio. The effect of pH can be overcome by simultaneously measuring the pH of the solution and considering the respective pH based absorption trend. By keeping the dithizone:mercury ion concentration ratio at an optimum value and using multiple sensors with different dithizone concentrations, henceforth, different detection range, dynamic detection range can be extended. Also, the pH based investigations were exploited to recover the dithizone and the effect of changing the pH of the mercury dithizone solution can be seen in appendix – III. Results have shown that lowering the pH ($pH<3$) using HCl, dithizone and mercury ions can be separated [23] which will be used further to regenerate the sensor surface for the next measurement.

3.5 Sensor Development

In the feasibility study, it was established that using evanescent wave absorption spectroscopy, heavy metal ions can be detected using dithizone. This section reports the immobilization of dithizone on the surface of an optical fibre and a novel inverted trench design based fibre optic sensor development to enhance the sensitivity by increasing the evanescent field interaction with the analyte.

3.5.1 Sensor Fabrication

A standard multimode step index silica fibre with core and cladding diameter 200 and 230 μm respectively has been used to develop the sensor. The polymer coating (jacket) of the fibre has been removed mechanically using a commercially available optical fibre stripper for a length of about 5 cm. Cladding (3 cm in length) of the fibre has been removed using acetone. An uncladded fibre has been coated with a layer of PMMA (1 mg/ml) by dip coating with the help of a dip coater unit, at a pulling rate of 37.5 mm/min. After the fibre was fully immersed in the PMMA solution 1 min settling time was allowed and thereafter, it was removed from the solution at the same speed. The coated fibre was allowed to dry at room temperature for 2 hours. Thereafter, the same process was repeated by replacing the PMMA solution with dithizone (1mM). The coated fibre was kept inside the dithizone solution for 2 hours to allow the binding process, thereafter; it was removed from the solution and dried at room temperature.

Figure 3.17(a) and (b) show the SEM images of the coating on the fibre at different magnifications. SEM images indicate that the coating is uniform and the surface is smooth. An overall thickness of the fibre with the coating was about 220 μm which leads to the coating thickness of approximately 10 μm.

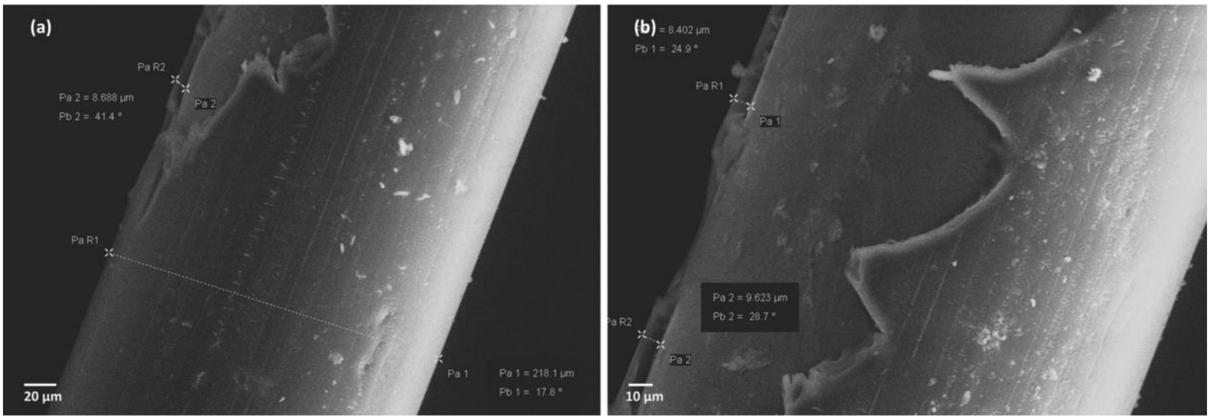

Figure 3.17 SEM images of the coated optical fibre at (a) 700x and (b) 1000x magnification.

3.5.2 Results and Discussions

A similar experiment was performed with the same setup by replacing the previous polymer fibre with the new silica fibre coated with dithizone. Prior to each sample of copper ions, a reference spectrum was collected in water. After the measurement, sensor surface was recovered using pH 3 solution followed by a wash in water. Figure 3.18 shows the plot of I/I_{ref} with copper ion concentrations. It was observed that with an increase in copper ion concentrations, I/I_{ref} decreases exponentially as depicted in theory.

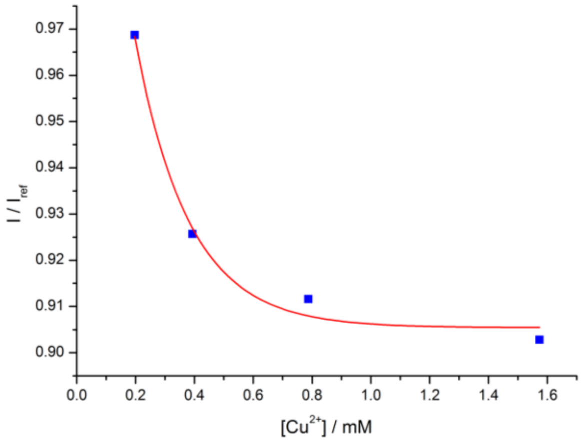

Figure 3.18 Output signal trend with copper ion concentrations.

3.6 U-bend Probe Design using ITF Configuration

3.6.1 Background and Introduction

A light ray launched selectively at an angle close to the critical angle propagating through the fibre, when encounters the aqueous medium (water, n_2=1.330), observes a lower critical angle. Therefore, the penetration depth of the light ray into the water becomes very low. Fibre optic sensors which work on the evanescent wave based sensing principle, especially with a straight or uniform geometry, have their sensitivity limited by the very weak evanescent field absorption due to the small penetration depth. In order to increase the sensitivity, approaches such as selective launching of the specific light modes into the fibre [28], tapering the sensing probe [29] or U-bent probe were reported [30]. Bending the fibre transfers the power from the guided modes to the leaky modes which results in more power to interact with the analyte and therefore, higher sensitivity [30,31].

Demand for trench-assisted multi-core optical fibres has been increasing in the recent years [32-35] due to their advantages such as low bending loss [32,33,36] (insensitive to bending), low crosstalk, high-density space-division multiplexing and wavelength division multiplexing [34,35]. Trench assisted designs in slab waveguides for various integrated optic applications are also becoming popular among researchers [37-39]. The special properties offered by various novel trench-assisted designs in slab waveguides and optical fibres have created a huge potential in various applications. A novel inverted trench design has been developed in order to confine the propagating light at the interface region in the sensing area.

Further work is carried out by developing an inverted trench design (ITF) based U-bend probe to enhance the sensitivity, where the propagating light confines to the trench area. An inverted trench based fibre optic evanescent wave sensor has been developed to estimate the copper ions in aqueous environments. This section reports the computational and experimental investigations on the effect of bending on the sensitivity of fibre optic sensor in estimating the copper ion concentration. COMSOL Multiphysics software has been used to carry out the computational work.

3.6.2 Theory and Computations

In fibre optic evanescent wave absorption based sensors, sensitivity depends on the interaction of evanescent field with the absorbing species. As discussed in the theory of an optical fibre sensors (section 3.2), reduction factor r_f is the major contributor to the sensitivity. Refractive indices n_r and n_e cannot be changed as are the property of the respective materials, but η can be increased by modifying the geometry of the fibre. Therefore, the work carried out here only focuses on the η.

Computational work was carried out for three different fibres, hard clad silica fibre (HCF), bare silica fibre (BF) and inverted trench silica fibre (ITF) for straight and bend geometrical configurations. The full vectorial finite element software COMSOL Multiphysics version 4.4 was used to analyse the design. The effect of bending curvature of the fibre can be represented by proper coordinate transformation (conformal mapping) as described by Heiblum & Harris [40]. Modelling of the sensor design in an aqueous environment was implemented in 2D-axisymmetry in order to compensate for the additional path length introduced by bending. The transverse plane of fibre cross-section is in the r-z plane and the fibre bent is in the ψ-r plane making ψ as the propagation direction of the wave. Evanescent power fraction η in ψ direction is expressed as (eq. (3.11)) [41]:

$$\eta = \int_{water}^{same\ mode} (E_x H_y - H_x E_y) dxdy / \int_{Total}^{same\ mode} (E_x H_y - H_x E_y) dxdy \qquad \text{...eq. (3.11)}$$

Figure 3.19(a) shows the E-field distribution in HCF, BF and ITF in a straight configuration and a refractive index profile of inverted trench design. A red colour indicates very strong electric field and dark blue colour represents no electric field. In HCF, E-field is confined in the centre of the fibre core, while, in BF, fibre modes goes under transition to whispering gallery modes and confine towards the surface [42]. In the case of ITF, due to the inverted trench design, all the E-field confines in the trench area. Figure 3.19(b) shows the comparison of the power fraction η for the HCF, BF and ITF in a straight and bend configuration, where η has been normalized with respect to the bend radius 1.5 cm. Observed higher value of η for the inverted trench based design makes this design a suitable candidate for evanescent wave based sensing applications.

To understand the bending effect on the ITF design for sensing applications, bend analysis was carried out by bending the HCF, BF and ITF at radii R = 2.5, 2.0 and 1.5 cm. Calculated results show that value of η nearly doubles in a straight configuration for an ITF over BF, while about 10 fold increase was observed in a bend configuration at radius of 1.5 cm. This increase was due to the increased effective area of the fibre while maintaining low loss [36]. Also, bending the fibre has caused the E-field loss which led to a slight decrease in η observed in BF [43]. The sensitivity of the evanescent field based sensors directly depends on the η and therefore, observed 10 fold enhancement in η is very significant.

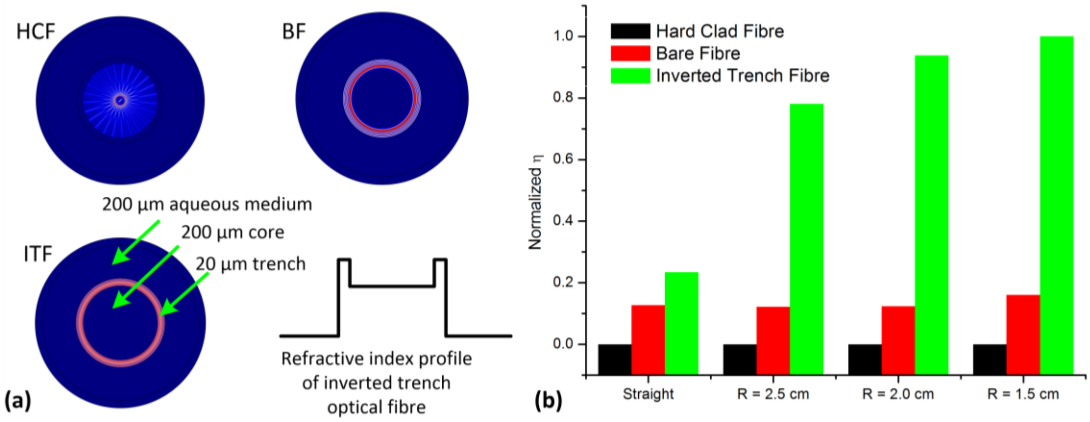

Figure 3.19 (a) Computational images of electric field distribution in cross-sections of HCF, BF and ITF, and a refractive index profile of ITF. (b) Normalized power fraction η of HCF, BF and ITF for straight and different bend radii R.

Further, as the light confines and propagates in the trench region, width of the trench plays a crucial role. Therefore, effect of trench width on the power fraction η has been analysed by calculating η with varying trench width. Figure 3.20 (a) shows the plot of normalized η with trench width varying from 5-100 µm in a straight configuration. Results show that maximum η can be achieved at 20 µm trench width. Further to understand the effect of trench width on η under bend configuration of ITF, calculations were carried out for 10 and 20 µm trench width. Figure 3.20 (b) shows the plot of normalized η in straight and bend configurations for 10 and 20 µm trench widths. Results follow the same trend as observed in the straight ITF configuration, allowing maximum η at 20 µm trench width.

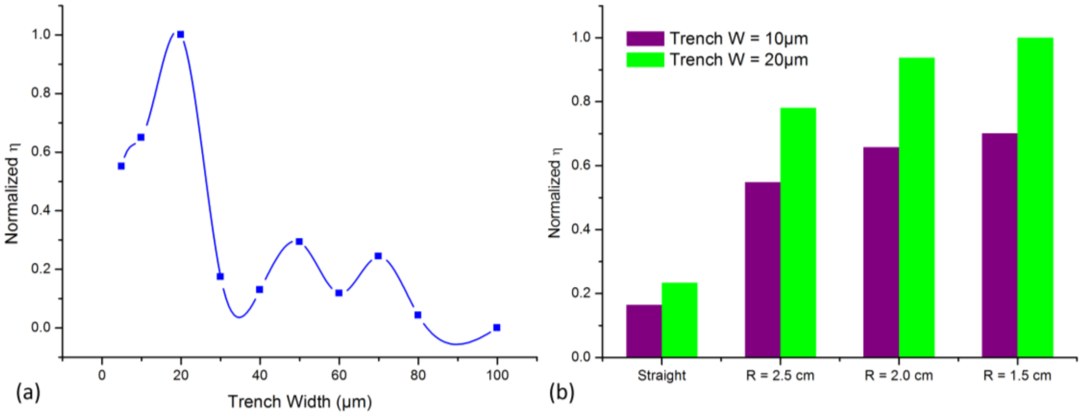

Figure 3.20 (a) Normalized evanescent power fraction in ITF for a straight configuration with varying trench width and (b) for a straight and and different bend radii, R at 10 and 20 μm trench width.

3.6.3 Experimental

3.6.4 Chemicals

Analytical grade copper sulphate, poly(methyl methacrylate), dithizone, anisole and isopropanol were purchased from Sigma-Aldrich, UK and used without any further purification.

3.6.5 Inverted Trench Fibre Optic Sensor Development

An uncladded fibre was coated with a layer of PMMA (1 mg/ml) by dip coating with the help of a dip coater unit, at a pulling rate of 37.5 mm/min. After the fibre was fully immersed in the PMMA solution 1 min settling time was allowed and thereafter removed from the solution at the same speed. The coated fibre was allowed to dry at room temperature for 2 hours. Dip coating process was repeated again with PMMA solution. Thereafter, the same process was repeated by replacing the PMMA solution with dithizone (1 mM). The coated fibre was kept inside the dithizone solution for 2 hours to allow the binding process and thereafter removed from the solution and dried at room temperature.

3.6.6 Experimental Setup

A pictorial view of the simple experimental setup is shown in Figure 3.21. A white light LED from Electrospell Ltd was used as broadband light source and the light was coupled to the fibre through a plano-convex lens. Commercially available optical fibre stripper and cutter have been used to remove the jacket (3 cm in length) of an optical fibre. Cladding has been removed using acetone and coated with dithizone using a dip coating unit. This coated fibre has been mounted using a custom made fibre U-bend holder and exposed to the aqueous copper ion solutions throughout the experiment.

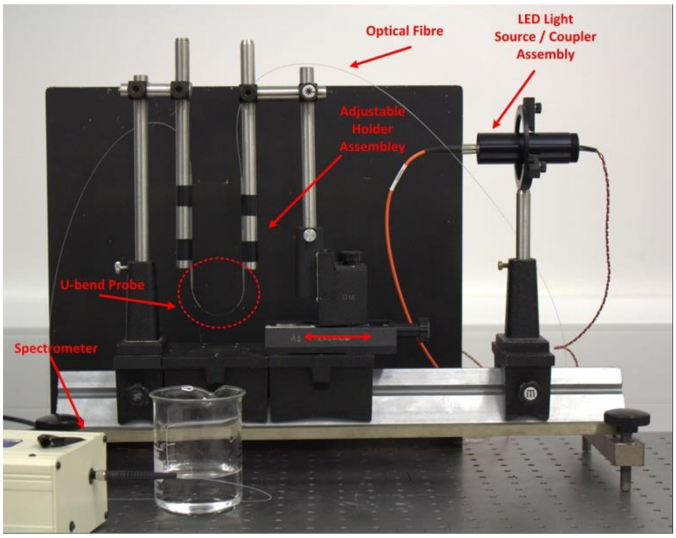

Figure 3.21 A pictorial view of the experimental setup.

U-bend radii of 1.5, 2.0 and 2.5 cm can be adjusted with the movable holder. The optical signal transmitted through the fibre has been detected using a Stellarnet (EPP2000C) spectrometer with an integration time of 250 ms.

3.6.7 Results and Discussions

For a range of copper ion concentrations output signals have been collected from the developed inverted trench fibre optic sensor. Figure 3.22(a) shows the output signal trend I/I_{ref} with increasing copper ion concentration at 460 nm which decreases with increasing concentrations. This decrease in signal was due to the increased absorption of the evanescent field by the samples.

In order to analyse the bending effect on sensitivity experimentally, we have carried out experiments with the same radius used in theoretical calculations. Figure 3.22(b) shows the change in copper ion signal with increasing concentrations for the bend radius R = 2.5, 2.0 and 1.5 cm of the sensor measured at 460 nm. Results show that the smallest bend radius (1.5 cm) has the highest sensitivity, in agreement with the computational results. Copper ions were detected at very high concentrations in the case of bend radii of 2.0 and 2.5 cm, but the negligible effect for concentrations lower than 10 ppm. The observed higher sensitivity with the bend radius of 1.5 cm can be attributed to the higher power fraction η available to interact with the analyte. As discussed in theory of the evanescent wave absorption based waveguide sensors (section 3.2, equation 3.9 and 3.10) increase in the η cause the increase in reduction factor r_f leads to higher sensitivity.

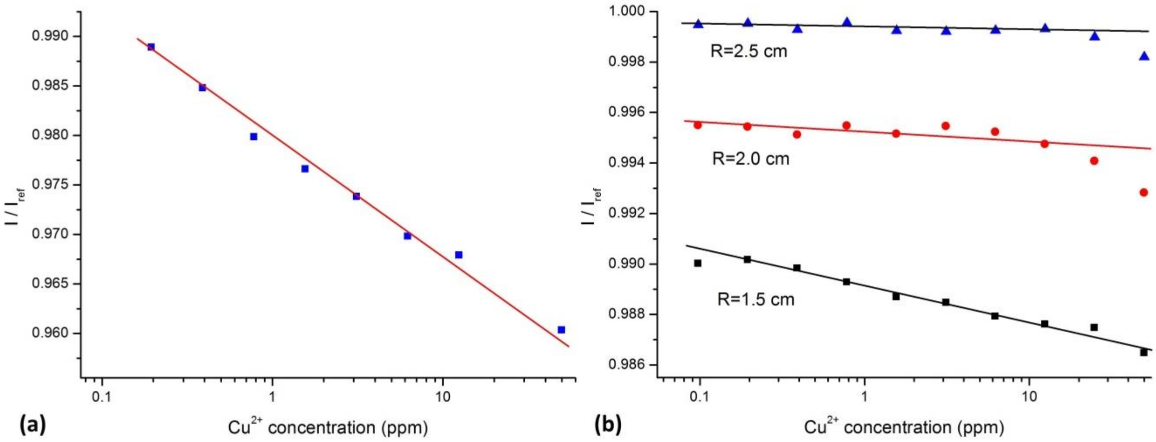

Figure 3.22 (a) A trend of the output signal with copper ion concentrations from the developed inverted trench based fibre optic sensor and (b) intensity change of copper ion signal with different bending radii, R.

Further to verify the effect of trench width *W,* on the sensitivity, trench of 10 and 20 μm have been developed on the optical fibre using the same coating technique as described earlier in the sensor fabrication section. Figure 3.23(a) and (b) show the SEM images of 10 and 20 μm trench widths developed on the optical fibre. Two similar experiments were performed with 10 and 20 μm trench width for the U-bend radius of 1.5 cm. Figure 3.23 (c) shows the gradient of intensity change at different copper ions concentrations for trench width of 10 and 20 μm. The 20 μm trench width has shown a rapid change in copper ion signal for lower concentrations due to the increased power fraction η. For 10 μm trench, the optical field is more confined and shrinks to the centre of the trench. While, in the case of 20 μm trench, effect of trench assisted optical field confinement reduces which allows propagation of some of the leaky modes and thereby, increasing the effective area and hence, the sensitivity [19]. Sensitivity can be further enhanced by tailoring the fibre parameters as discussed in the theory section.

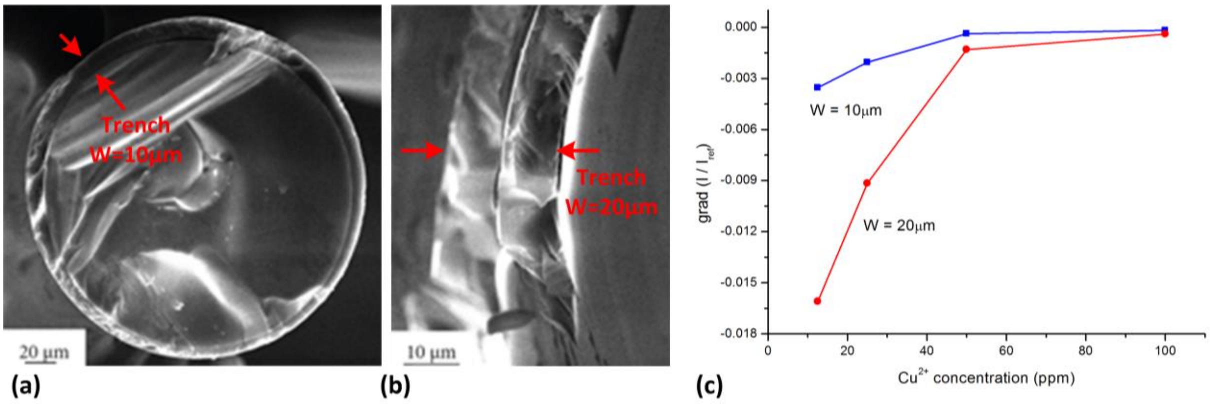

Figure 3.23 SEM images of an optical fiber with (a) 10 μm and (b) 20 μm trench. (c) Change in measured intensity with copper ion concentrations for 10 μm and 20 μm trench.

3.7 Summary

Development of an optical fibre based heavy metal ions sensor has been carried out. Dithizone has been used as a sensitive and selective reagent to detect heavy metal ions. For the first time, dithizone has been used to detect heavy metal ions using an evanescent wave absorption spectroscopy based approach. Effects of environmental parameters such as pH and concentration ratio of dithizone and metal ions have been investigated to achieve optimum conditions and improve the sensitivity. A possibility of multi-ion detection has been investigated for chromium, copper and mercury. In this work, using the developed evanescent wave sensor detection of chromium, copper and mercury ions has been carried out. Detected mercury and copper ion concentrations using the developed sensor were found to be lower than the safe thresholds suggested by the World Health Organization (WHO) in drinking water [44].

For the first time, novel U-bend probe based on an inverted trench based design has been developed in order to enhance the sensitivity of the evanescent absorption based approach. Higher sensitivity has obtained through developed ITF based sensor in U-bend configuration and verified by computational simulations accompanied by experimental work. Also, results have shown that the trench width and U-bend radius are the significant geometrical design parameters to obtain the higher sensitivity.

As discussed in chapter 1 and 2, about the unique surface properties of the nanomaterials, surface modifications of the sensor will be carried out using nanomaterials to utilize their properties in further enhancing the sensitivity. Next chapter discusses various investigations on the sensor surface modifications using nanomaterials.

3.8 References

[1] T. Li, S. Dong, E. Wang, Label-Free Colorimetric Detection of Aqueous Mercury Ion (Hg2+) Using Hg2+-Modulated G-Quadruplex-Based DNAzymes, Anal. Chem. 81 (2009) 2144-2149.

[2] D. Wu, W. Huang, C. Duan, Z. Lin, Q. Meng, Highly sensitive fluorescent probe for selective detection of Hg2+ in DMF aqueous media, Inorg. Chem. 46 (2007) 1538-1540.

[3] B. Liu, F. Zeng, Y. Liu, S. Wu, A FRET system built on quartz plate as a ratiometric fluorescence sensor for mercury ions in water, Analyst. 137 (2012) 1698-1705.

[4] A. Afkhami, T. Madrakian, S.J. Sabounchei, M. Rezaei, S. Samiee, M. Pourshahbaz, Construction of a modified carbon paste electrode for the highly selective simultaneous electrochemical determination of trace amounts of mercury(II) and cadmium(II), Sensor Actuat. B-Chem. 161 (2012) 542-548.

[5] J.C.C. Yu, E.P.C. Lai, S. Sadeghi, Surface plasmon resonance sensor for Hg(II) detection by binding interactions with polypyrrole and 2-mercaptobenzothiazole, Sensor Actuat. B-Chem. 101 (2004) 236-241.

[6] C. Chen, Y. Du, J. Li, X. Yang, E. Wang, Fabrication of a sensor chip containing Au and Ag electrodes and its application for sensitive Hg(II) determination using chronocoulometry, Anal. Chim. Acta. 738 (2012) 45-50.

[7] C. Guo, J. Irudayaraj, Fluorescent Ag Clusters via a Protein-Directed Approach as a Hg(II) Ion Sensor, Anal. Chem. 83 (2011) 2883-2889.

[8] W. Ma, C. Hao, W. Ma, C. Xing, W. Yan, H. Kuang, L. Wang, C. Xu, Wash-free magnetic oligonucleotide probes-based NMR sensor for detecting the Hg ion, Chem. Commun. 47 (2011) 12503-12505.

[9] H.H. Zeng, R.B. Thompson, B.P. Maliwal, G.R. Fones, J.W. Moffett, C.A. Fierke, Real-time determination of picomolar free Cu(II) in seawater using a fluorescence based fiber optic biosensor, Anal. Chem. 75 (2003) 6807-6812.

[10] B. Gu, M. Yin, A.P. Zhang, J. Qian, S. He, Fiber-optic metal ion sensor based on thin-core fiber modal interferometer with nanocoating self-assembled via hydrogen bonding, Sensor Actuat. B-Chem. 160 (2011) 1174-1179.

[11] S.K. Srivastava, B.D. Gupta, Influence of ions on the surface plasmon resonance spectrum of a fiber optic refractive index sensor, Sensor Actuat. B-Chem. 156 (2011) 559-562.

[12] S. Jung, T. Lee, W.M. Kim, K. Lee, D.S. Jeong, W.S. Lee, I. Kim, Thickness dependence of surface plasmon resonance sensor response for metal ion detection, J. Phys. D: Appl. Phys. 46 (2013) 315104.

[13] M. Benounis, N. Jaffrezic-Renault, H. Halouani, R. Lamartine, I. Dumazet-Bonnamour, Detection of heavy metals by an optical fiber sensor with a sensitive cladding including a new chromogenic calix[4]arene molecule, Mat. Sci. Eng. C-Bio. S. 26 (2006) 364-368.

[14] X.B. Zhang, C.C. Guo, Z.Z. Li, G.L. Shen, R.Q. Yu, An optical fiber chemical sensor for mercury ions based on a porphyrin dimer, Anal. Chem. 74 (2002) 821-825.

[15] F. Long, C. Gao, H.C. Shi, M. He, A.N. Zhu, A.M. Klibanov, A.Z. Gu, Reusable evanescent wave DNA biosensor for rapid, highly sensitive, and selective detection of mercury ions, Biosens. Bioelectron. 26 (2011) 4018-4023.

[16] J. Perez-Hernandez, J. Albero, E. Llobet, X. Correig, I.R. Matias, F.J. Arregui, E. Palomares, Mercury optical fibre probe based on a modified cladding of sensitised Al(2)O(3) nano-particles, Sensor Actuat. B-Chem. 143 (2009) 103-110.

[17] B. Kuswandi, Simple optical fibre biosensor based on immobilised enzyme for monitoring of trace heavy metal ions, Anal. Bioanal. Chem. 376 (2003) 1104-1110.

[18] V.V.R. Sai, T. Kundu, C. Deshmukh, S. Titus, P. Kumar, S. Mukherji, Label-free fiber optic biosensor based on evanescent wave absorbance at 280 nm, Sensor Actuat. B-Chem. 143 (2010) 724-730.

[19] Z. Fang, K.K. Chin, R. Qu, H. Cai, Fundamentals of Optical Fibers, John Wiley & Sons, Inc., New Jersey, 2012.

[20] R. Schasfoort, A. Tudos, Handbook of Surface Plasmon Resonance, Royal Society of Chemistry, Cambridge, United Kingdom, 2008.

[21] N. Sultanova, S. Kasarova, I. Nikolov, Dispersion Properties of Optical Polymers, Acta Physica Polonica a. 116 (2009) 585-587.

[22] J. Dakin, B. Culshaw, Optical Fiber Sensors: Components and Subsystems, 3rd ed., Artech House, London, 1996.

[23] W.E. White, Dithizone as an analytical reagent, J. Chem. Educ. 13 (1936) 369.

[24] M. Shariati-Rad, M. Hasani, Principle component analysis (PCA) and second-order global hard-modelling for the complete resolution of transition metal ions complex formation with 1,10-phenantroline, Anal. Chim. Acta. 648 (2009) 60-70.

[25] W. Xu, C. Ren, C.L. Teoh, J. Peng, S.H. Gadre, H. Rhee, C.K. Lee, Y. Chang, An Artificial Tongue Fluorescent Sensor Array for Identification and Quantitation of Various Heavy Metal Ions, Anal. Chem. 86 (2014) 8763-8769.

[26] V. Vallet, U. Wahlgren, I. Grenthe, Chelate Effect and Thermodynamics of Metal Complex Formation in Solution: A Quantum Chemical Study, J. Am. Chem. Soc. 125 (2003) 14941-14950.

[27] A.S.R. Potty, J.Y. Fu, S. Balan, B.L. Haymore, D.J. Hill, G.E. Fox, R.C. Willson, Neutral additives enhance the metal-chelate affinity adsorption of nucleic acids: Role of water activity, J. Chromatogr. 1115 (2006) 88-92.

[28] V. Ruddy, B.D. Maccraith, J.A. Murphy, Evanescent Wave Absorption-Spectroscopy using Multimode Fibers, J. Appl. Phys. 67 (1990) 6070-6074.

[29] B.D. Gupta, C.D. Singh, Evanescent-Absorption Coefficient for Diffuse Source Illumination - Uniform-Fiber and Tapered-Fiber Sensors, Appl. Opt. 33 (1994) 2737-2742.

[30] B.D. Gupta, H. Dodeja, A.K. Tomar, Fibre-optic evanescent field absorption sensor based on a U-shaped probe, Opt. Quant. Electron. 28 (1996) 1629-1639.

[31] S.K. Khijwania, K.L. Srinivasan, J.P. Singh, An evanescent-wave optical fiber relative humidity sensor with enhanced sensitivity, Sens. Actuator B-Chem. 104 (2005) 217-222.

[32] J. Sun, Z. Kang, J. Wang, C. Liu, S. Jian, Novel bending-resistant design of two-layer low-index trench fiber with parabolic-profile core, Optics Express. 22 (2014) 18036-18043.

[33] P.R. Watekar, S. Ju, W. Han, Optimized design of trenched optical fiber for ultralow bending loss at 5mm of bending diameter, Appl. Opt. 50 (2011) E97-E101.

[34] S. Li, J. Wang, A Compact Trench-Assisted Multi-Orbital-Angular-Momentum Multi-Ring Fiber for Ultrahigh-Density Space-Division Multiplexing (19 Rings x 22 Modes), Sci. Rep. 4 (2014) 3853.

[35] S. Li, J. Wang, Multi-orbital-angular-momentum multi-ring fiber for high-density space-division multiplexing, IEEE Photonics Journal. 5 (2013) 7101007.

[36] B.L. Behera, A. Maity, S.K. Varshney, R. Datta, Theoretical investigations of trench-assisted large mode-area, low bend loss and single-mode microstructured core fibers, Opt. Commun. 307 (2013) 9-16.

[37] K. Liu, H. Huang, S.X. Mu, H. Lin, D.L. Macfarlane, Ultra-compact three-port trench-based photonic couplers in ion-exchanged glass waveguides, Opt. Commun. 309 (2013) 307-312.

[38] W. Wang, W. Liu, S. Wang, J. Shao, Z. Xu, C. Guan, Integrated tunable optical dispersion compensator consisting of arrayed waveguide grating with air trench output waveguides, J. Lightwave Technol. 29 (2011) 2039-2047.

[39] A.V. Velasco, M.L. Calvo, P. Cheben, A. Ortega-Monux, J.H. Schmid, C.A. Ramos, I.M. Fernandez, J. Lapointe, M. Vachon, S. Janz, D. Xu, Ultra-compact polarization mode converter implemented in a dual-trench silicon-on-insulator waveguide, (2012) 1-2.

[40] K. Seshan, Handbook of Thin-Film Deposition Processes and Techniques - Principles, Methods, Equipment and Applications, 2nd ed., William Andrew Publishing, Norwich, 2002.

[41] Y.L. Hoo, W. Jin, C. Shi, H.L. Ho, D.N. Wang, S.C. Ruan, Design and modeling of a photonic crystal fiber gas sensor, Appl. Opt. 42 (2003) 3509-3515.

[42] R.T. Schermer, J.H. Cole, Improved bend loss formula verified for optical fiber by simulation and experiment, IEEE J. Quant. Electron. 43 (2007) 899-909.

[43] D. Marcuse, Field deformation and loss caused by curvature of optical fibers, J. Opt. Soc. Am. 66 (1976) 311-320.

[44] World Health Organization, Guidelines for drinking-water quality, 2015 (2011) 564.

Chapter 4

Investigations on Surface Modifications using Nanomaterials

4 Investigations on Surface Modifications using Nanomaterials

4.1 Introduction

An inverted trench design provides higher sensitivity as concluded in the chapter 3 based on theoretical and experimental investigations. From the literature, it is known that nanostructures provide a very high surface to volume ratio. Therefore, sensor surface modified with nanomaterials can provide enhanced surface interactions leading to further increased sensitivity. This chapter reports investigations on the surface modifications using nanomaterials to enhance the sensitivity.

Materials identified for the surface modification includes: (i) optical material (transparent/semi-transparent) and electrically active (conductive/ semiconductive) (ii) their refractive index greater than the waveguide material (specifically in visible wavelength range) (iii) and suitable to coat/synthesize on waveguide material. ZnO is a wide bandgap semiconducting material and has a refractive index greater than the waveguide material (BK6/SF10/SF11 glass/fused silica). Synthesis of various ZnO nanostructures, and their interactions with heavy metal ions and dithizone have already been discussed in chapter 2. Other suitable candidates for this application are gold thin film and its nanostructures and graphene and have been characterized and discussed.

For simplicity, glass slide has been used to study the interaction of aqueous solution with the surface modified with ZnO nanostructures. Thereafter, synthesis of ZnO nanostructures on the surface of an optical fibre is carried out. Similarly, rectangular glass waveguide coated with thin film of gold (~50 nm) has been used to develop ZnO nanostructures on the surface and investigated. At last, graphene, another suitable material for the hybrid sensor development, has been investigated. Dispersions of graphene flakes have been used to modify the surface of the gold coated glass slide.

4.2 Surface Modification by ZnO Nanowires

The surface properties (hydrophilic or hydrophobic nature) of ZnO play a crucial role in aqueous environments, especially in sensing applications such as biosensing, biomedical and microfluidic applications [1]. Adsorption/adhesion of species on the surface and their interaction depends on the surface energy and it closely relates to the wetting nature of the surface [2]. Therefore, control over the wettability is highly required in all such applications. Broadly, there are two distinct approaches, contact and non-contact type, for changing the wettability of the surface. In a contact type, the surface is being chemically modified using low/high energy material which is not desirable [3]. Non-contact type approaches include high-temperature annealing [4], plasma treatment [5], ion sputtering [4] and light illumination [6]. Recently, light-induced wettability tuning is becoming popular [7-9].

However, the major problem arises in the control over surface wettability which is crucial for improving the interaction between surface and surrounding aqueous medium. Therefore, it is important to have a well-defined control over the surface wettability of ZnO nanowires. Several papers have reported on the tunable wettability shown by ZnO nanowires exposed to UV lamps [8-10]. However, these lamps are relatively slow to switch on, stabilize and also, generate a considerable amount of heat. Further, they are not eco-friendly, they are a potential health hazard due to the UV exposure and limit the miniaturization of the devices. A UV lamp imposes the problem of destroying the biomolecules/cells on the surface because of deep UV light (UV-C) irradiation [11]. Therefore, use of UV lamps to tune the surface wettability of ZnO nanowires is not a convenient approach. Also, UV lamps cannot provide well-defined control over the surface wettability. This is the first study on LED based control of ZnO nanowires' wettability and its wavelength dependency. LEDs are smaller in size, inexpensive, energy efficient, have a narrow emission spectrum and offer better tunability of various control parameters. Therefore, LEDs can offer advanced and dynamic control over the tuning of surface wettability. Also, LEDs can be integrated on the sensor chip.

The role of light wavelength in controlling the surface wettability of ZnO nanowires is unclear. Therefore, the role of LED emission wavelength in controlling the wettability of ZnO nanowires have been investigated and discussed in this chapter. Initial investigations on the spectral effects of light irradiation, using LEDs (λ_p = 365 nm, 385 nm, 454 nm and 519 nm), on the hydrophobicity of ZnO nanowire films have been carried out. Also, the effects of light wavelength and irradiation time over the hydrophobic-hydrophilic transition rate and relative change in contact angle have been studied. Results show that spectral overlap between LED emission spectra and ZnO nanowire absorption spectra defines the rate of change in wetting angle of ZnO nanowires. LED with λ_p = 365 nm has shown very high transition rate compared to other wavelengths. Also, LEDs with emission wavelengths of 454 nm and 519 nm did not show change to the hydrophobic state of the ZnO nanowires even after 30 min of irradiation.

4.2.1 Materials and Methods

4.2.1.1 Materials

All the materials used in the experiment were analytical grade. Zinc acetate, zinc nitrate hexahydrate and ammonium hydroxide were purchased from the Sigma-Aldrich, UK. All glassware was cleaned in deionized water prior to the experiment.

4.2.1.2 Synthesis of ZnO Nanowire Films

ZnO nanowires were grown on glass substrates using hydrothermal synthesis method [12]. 10 mM zinc acetate was drop casted on the glass substrates and annealed on a hotplate for one min at 100°C for better adhesion. The process was repeated 5 times to get a uniform thick seed layer. ZnO nanowires were grown by immersing the seeded substrates into the mixture of 125 ml 20 mM zinc nitrate and 7 ml 28-30% ammonium hydroxide and annealed on a hotplate at 95° C for 5 hours. Thereafter, substrates were removed from the growth solution and rinsed with de-ionized water several times. The substrates were allowed to dry at room temperature and atmospheric pressure before characterization.

Surface analysis of the synthesized ZnO nanowire films was carried out using a Scanning Electron Microscope from ZEISS (EVO LS10). Surface wettability was characterized using contact angle measurement system from the First Ten Angstrom (FTA200) at room temperature (RH - 8%). The absorption spectrum of the ZnO nanowires was collected using Lambda 950 UV/Vis Spectrometer from Perkin Elmer.

4.2.2 Experiments

A schematic view of the experimental setup for irradiating the samples with LEDs is shown in Figure 4.1. LEDs (λ_p = 365 nm and 385 nm) were purchased from Nichia Corporation and LEDs (λ_p = 454 nm and 519 nm) were purchased from Avago Technologies. Full spectral width at the half maximum of the LEDs (λ_p = 365 nm, 385 nm, 454 nm and 519 nm) were 15 nm, 15 nm, 25 nm and 30 nm respectively. LED emission was coupled through a bi-convex lens and irradiated over the sample placed on a sample stage. A neutral density filter and aperture were used to control the optical power density. A dichroic mirror was used in the path to tap a fraction of the light for monitoring the power level with a Coherent (FieldMaster GS) power meter and/or LED spectra with StellerNet (EPP2000C) spectrometer. Surface wettability of the developed ZnO nanowires was studied using the contact angle measurement system, by measuring the water contact angle before and after the light irradiation for different time durations. All light irradiation experiments were performed at constant optical power. All contact angle measurements were carried out using 2 μl water drop under ambient conditions.

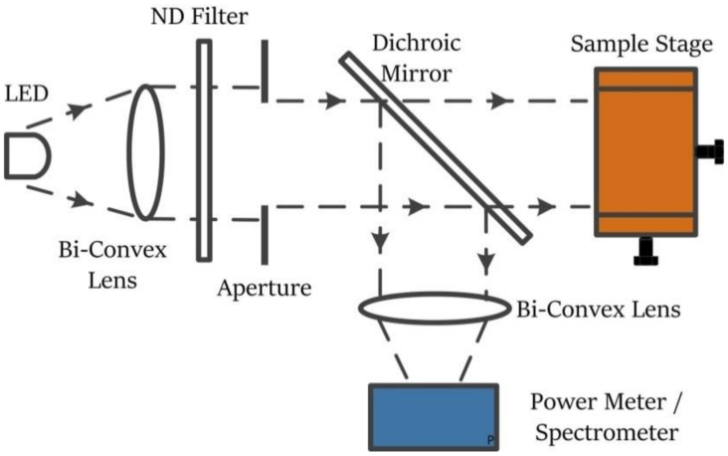

Figure 4.1 A schematic view of the experimental setup.

4.2.3 Results and Discussions

Figure 4.2 shows the SEM image of ZnO nanowires at different magnifications. From the SEM image, it can be seen that the synthesized ZnO nanowires are preferentially oriented towards the c-axis perpendicular to the glass substrate. The hexagonal structure of the ZnO nanowires can be seen in the magnified SEM image. Also, the magnified view of the nanowire tip reveals the growth of layered hexagonal nanostructures on the tip. This nanoscale roughness on the tip reduces the contact area between solid and the droplet which allows the entrapping of a large amount of air below the droplet, and therefore, enhances the hydrophobicity of the surface [9,13]. Length and diameter of the synthesized ZnO nanowires were about 11-12 µm and 400-500 nm respectively.

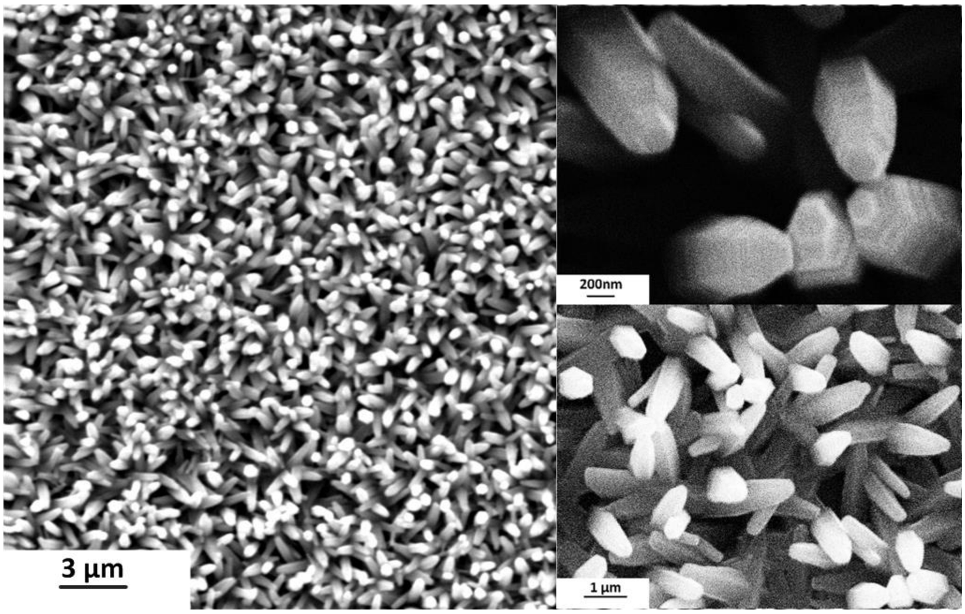

Figure 4.2 SEM images of the synthesized ZnO nanowires on glass at different magnifications.

The water contact angle was measured immediately after the synthesis of ZnO nanowires and found to be about 0°. This super hydrophilic nature shown by the as-synthesized ZnO nanowires using hydrothermal method can be attributed to the hydroxyl groups on the surface. Thereafter, substrates were left to dry under ambient conditions for 72 hours. During this process adsorbed hydroxyl groups on the surface were replaced by atmospheric oxygen leading to the hydrophobic surface. Therefore, measured water contact angle of ZnO nanowires after drying the substrate was around 125°.

Surface wettability of the synthesized ZnO nanowires was analysed by measuring the static contact angle. ZnO nanowires surface wettability can be considered conferring to the Cassie-Baxter [14] or Wenzel [15] models.

A Young contact angle, θ_y, on the smooth surface can be defined in terms of surface energy as [16]:

$$\cos\theta_y = (\gamma_{sv} - \gamma_{sl}) / \gamma_{lv}$$

where, γ_{sv}, γ_{sl} and γ_{lv} are surface tension of solid-vapour, solid-liquid and liquid-vapour, respectively. Considering the surface roughness, the Wenzel model defines the apparent contact angle, θ, as:

$$\cos\theta = r \cos\theta_y$$

where, r is a surface roughness factor. This suggests the effect of a change in surface roughness on the hydrophobicity (contact angle). But, the Wenzel model assumes that the liquid penetrates the rough surface which is the case after irradiation of UV light.

Under the unexposed condition, ZnO nanowires tend to show a hydrophobic surface where liquid does not penetrate the rough surface (nanowire groves). Therefore, this condition refers to the Cassie-Baxter state [14].

$$\cos\theta = f (\cos\theta_y + 1) - 1$$

where, f is the area fraction of actual solid surface area to the projected solid surface area. Therefore, upon UV light exposure, ZnO nanowires follow the wettability transition from Cassie-Baxter state to the Wenzel state.

A static water contact angle (WCA) has been measured on the ZnO nanowire sample before and after the light irradiation using UV LED (emission wavelength, λ_p = 365 nm). Figure 4.3 shows the measured WCA for the 0-30 minutes light illumination period and the inset pictures show the captured images of a water droplet on the sample before (hydrophobic) and after (hydrophilic) light irradiation. Within 5 minutes, ZnO nanowire surface undergoes hydrophobic-hydrophilic transition. This rapid transition rate can be attributed to the nanoscale structures on the tip [9]. A gradual change in WCA continues for further 5 minutes and thereafter, it slows down. The reason behind this observed change in wettability by light irradiation on the ZnO nanowires can be explained as follows:

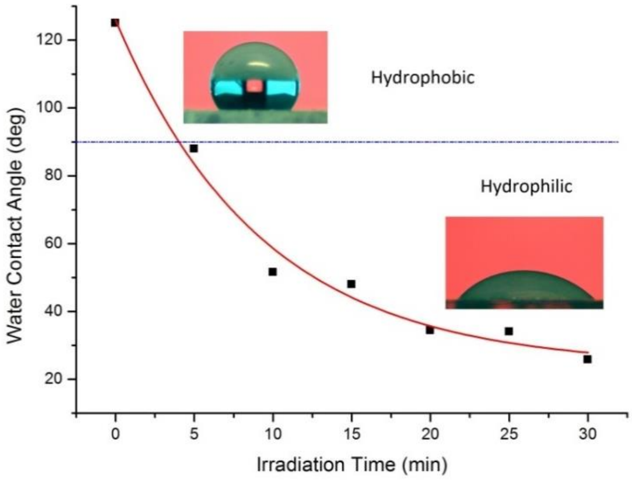

Figure 4.3 Measured WCA change over a time on ZnO nanowires irradiated with 365 nm LED. Inset pictures are captured images of a water droplet on the ZnO nanowire sample, before (hydrophobic) and after (hydrophilic) the light illumination. The trend line is the exponential curve fit to the measured WCA data.

As we know that ZnO is a large bandgap semiconducting material. Therefore, light with energy higher than the bandgap energy is absorbed by the ZnO. This absorption of light (photons) generates electron-hole pairs in the ZnO surface. These electron-hole pairs will further create the surface defects/composition change leading to different surface energy and hence, the surface wettability. The process which leads to the surface composition change can be expressed as [9]:

$$\mathrm{ZnO} + 2h\nu \rightarrow 2e^{-} + 2h^{+}$$

$$\mathrm{Zn}^{2+} + e^{-} \rightarrow \mathrm{Zn_s}^{+} \text{ (surface trapped electron)}$$

$$\mathrm{O}^{2-} + h^{+} \rightarrow \mathrm{O}^{-} \text{ (surface trapped hole)}$$

$$\mathrm{O}^{-} + h^{+} \rightarrow 1/2\mathrm{O}_2 + V_o \text{ (oxygen vacancy)}$$

The surface trapped electrons ($\mathrm{Zn_s}^{+}$) tend to react with oxygen molecules adsorbed on the surface:

$$\mathrm{Zn_s}^{+} + \mathrm{O}_2 \rightarrow \mathrm{Zn_s}^{2+} + \mathrm{O}_2^{-}$$

At the same time, water molecules may adsorb at the oxygen vacancy (V_o) site. These defect sites are kinetically more favourable for hydroxyl groups (OH^-) adsorption than oxygen adsorption, hence promotes increased water adsorption at the UV light irradiated areas. However, the adsorption of OH^- on the defective sites creates distortion in the electronic structure of the surface and makes it energetically unfavourable. Therefore, after the UV illumination stops, surface try to recover to its original hydrophobic state by replacing the adsorbed OH^- with the atmospheric oxygen. During this process, OH^- and atmospheric oxygen compete to dissociatively adsorb on the defect sites. Therefore, oxygen rich environment can promote the recovery rate [17].

Further to understand the effect of wavelength, light irradiation was carried out on the ZnO nanowires using LEDs with a peak emission wavelength λ_p = 365, 385, 454 and 519 nm. WCA was measured on each sample before and after the light irradiation and referred as WCA_0 and WCA respectively. Figure 4.4 shows the relative change in water contact angle (WCA/WCA_0) measured with irradiation time for different illumination wavelengths. Rapid change in wetting angle was observed for the LED with λ_p = 365 nm, as discussed earlier. Trend lines in the graph indicate that the change in wetting angle slows down gradually with increasing wavelength. In addition, results for the illumination wavelengths of 454 nm and 519 nm reveal that there was no clear hydrophobic-hydrophilic transition observed within 30 minutes of irradiation.

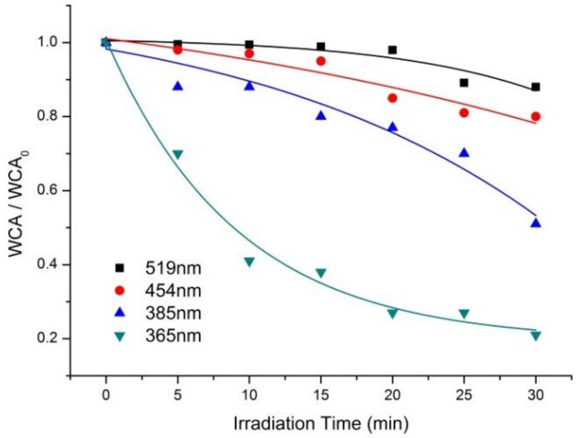

Figure 4.4 Measured relative contact angle change with irradiation time for different LED emissions at λp = 365, 385, 454 and 519 nm. Trend line indicates the respective exponential fit to the data.

As discussed earlier, the whole process of change in wettability depends on the absorption of light by ZnO nanowires. Therefore, to understand the observed spectral effect on the wettability, the absorption spectrum of the synthesized ZnO nanowires was collected. A normalized absorption spectrum of ZnO nanowires along with the LEDs normalized emission spectra are shown in Fig. 5. Better spectral overlap indicates that ZnO nanowires absorb more light at 365 nm than other wavelengths. Therefore, the rate of change in surface energy, and therefore, the wetting angle is very high for 365 nm than the other wavelengths. This indicates that the wettability of the ZnO nanowires can be controlled by tuning the wavelength of irradiating light. A small change observed in the wetting angle under 454 nm and 519 nm illuminations can be attributed to the small fraction of light absorbed by ZnO nanowires due to the native defects. Although, the spectral width of LEDs emitting at 454 nm and 519 nm is slightly higher than the other LEDs used in the experiment, a negligible effect was anticipated due to very low absorption by ZnO nanowires in that range (as seen in Figure 4.5).

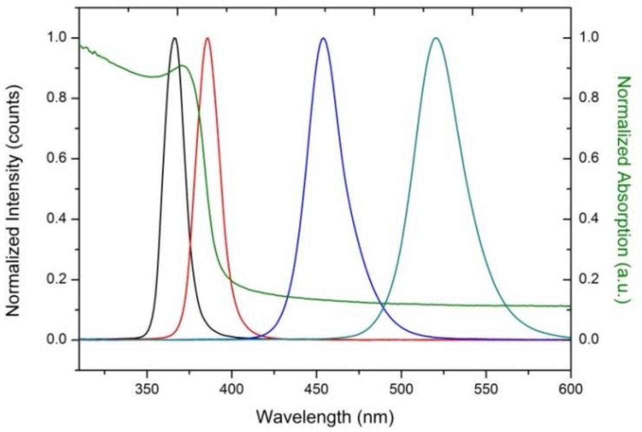

Figure 4.5 LEDs normalized emission spectra (λp = 365, 385, 454, 519 nm) along with ZnO nanowire normalized absorption spectrum in green.

4.3 Surface Modification by Different ZnO Structures

Investigations on the wettability of different ZnO nanostructures were carried out using contact angle measurements as discussed in the previous section. Figure 4.6(a) and (b) shows SEM images of ZnO nanowires synthesized on a glass slide using the hydrothermal method as described in chapter 2. The pilot window shows the corresponding SEM images at lower magnification and images of a water droplet on the surface. Measured contact angles on the ZnO nanowires and ZnO nanowire bundles were 119° and 94°C respectively. ZnO nanowire bundles have shown lower hydrophobicity than the nanowires because it has large porous structures on the surface which allow the water molecules to penetrate up to a certain distance, hence the measure WCA was lower. Figure 4.6 (c) and (d) show SEM images of developed ZnO thin films coated on glass slides from the ZnO nanoparticle and commercial powder dispersions. A thin coated ZnO nanoparticle film has shown a hydrophilic nature (measured WCA = 28°). A large amount of porosity and structural non-uniformities have been observed on the thin films made from commercial ZnO powder and therefore, water penetrates into the material.

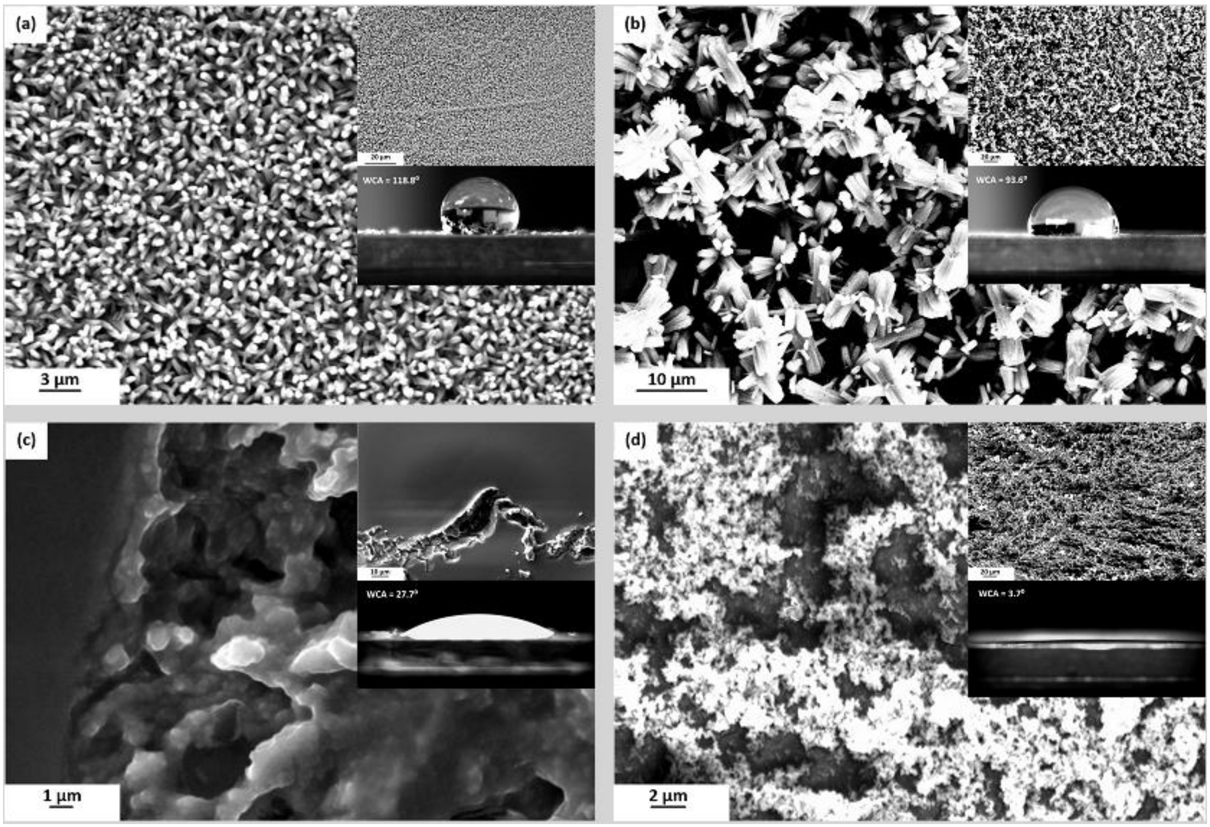

Figure 4.6 SEM images of ZnO (a) nanowires, (b) nanowire bundles, (c) nanoparticle thin film and (d) commercial ZnO powder film. Pilot windows show respective SEM images at a lower magnification and the image of a water drop showing the contact angle.

Wettability tuning of the ZnO nanowires and nanoparticle coated thin films using UV LED was also investigated and found similar results. Figure 4.7 shows the trend of measured water contact angle vs UV light irradiation time for ZnO nanowires and thin film. ZnO nanowires have shown the hydrophobic/hydrophilic state transition upon UV light irradiation within 35 min. ZnO thin film was turned into superhydrophilic from the initial hydrophilic state.

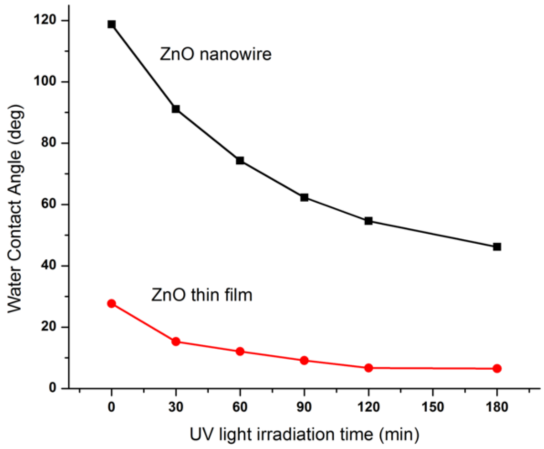

Figure 4.7 Measured water contact angle over a time on ZnO nanowires and thin film irradiated with 365 nm LED.

4.4 Surface Modification of an Optical Fibre by ZnO Nanostructure

4.4.1 Synthesis Method

ZnO nanostructures were grown on polyclad multimode silica optical fibre (200/230 μm) using hydrothermal synthesis method [12]. The materials used during the synthesis process were same as mentioned in section 4.2.1.1. Briefly, ZnO nanostructures were grown by immersing the cleaned optical fibre into the mixture of 125 ml 20 mM zinc nitrate and 7 ml 28-30% ammonium hydroxide and annealed on a hotplate at 95° C for 5 hours. Thereafter, optical fibres were removed from the growth solution and rinsed with de-ionized water several times. The optical fibres were allowed to dry at room temperature and atmospheric pressure before characterization. Surface analysis of the synthesized ZnO nanostructures was carried out using a Scanning Electron Microscope from ZEISS (EVO MA10).

4.4.2 Results and Discussions

Figure 4.8(a) shows the SEM image of the synthesized ZnO nanowires on the optical fibre. A high magnification image reveals the growth of bunched ZnO nanowires. The density of the synthesized ZnO nanowires is very low. The observed results of low dense bunched growth of ZnO nanowires can be attributed to the absence of the seed layer, as discussed in chapter 2. Briefly, in case of no seed layer, a nucleation site must be formed before the growth process. Consumption of Zn^{2+} ions is very high in the areas where crystal starts to build. Therefore, the availability of Zn^{2+} ions near the nucleation site is low which leads to the formation of branches in the crystal (as seen in Figure 4.8(b)). Overall, non-availability of the seed has caused the growth rate to slow down and bulk crystal formation with less density.

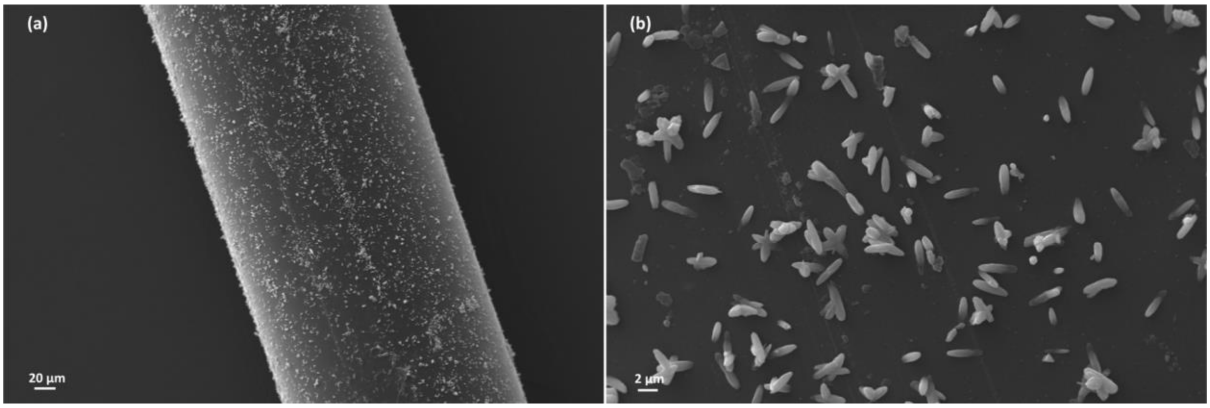

Figure 4.8 SEM images of ZnO nanostructures synthesized on an optical fibre at (a) 500x and (b) 5Kx magnification

4.5 Surface Modification of Gold Thin Film by ZnO Nanostructure

4.5.1 Synthesis Method

ZnO nanowires were synthesized on the gold coated glass substrate using hydrothermal method [12]. The materials used during the synthesis process were same as mentioned in section 4.2.1.1. Briefly, gold thin film coated substrates were immersed into the mixture of 125 ml 20 mM zinc nitrate and 7 ml 28-30% ammonium hydroxide and annealed on a hotplate at 95° C for 5 hours. Thereafter, substrates were removed from the growth solution and rinsed with de-ionized water several times. The substrates were allowed to dry at room temperature and atmospheric pressure before characterization. Surface analysis of the synthesized ZnO nanostructures was carried out using a Scanning Electron Microscope from ZEISS (EVO MA10).

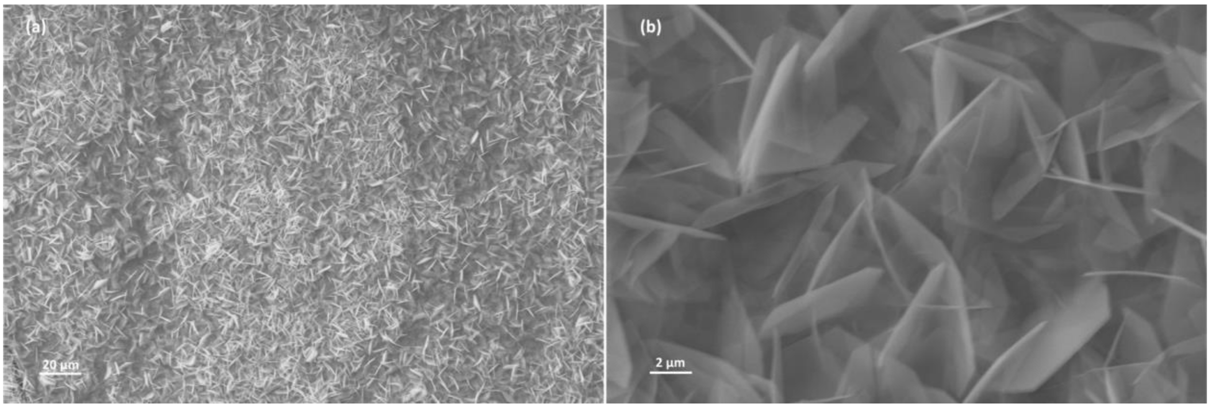

Figure 4.9 SEM images of ZnO nanosheets synthesized on gold thin film coated on glass substrate at (a) 1Kx and (b) 10Kx magnification

4.5.2 Results and Discussions

Figure 4.9 shows the SEM images of the synthesized ZnO nanosheets on the gold thin film coated on the glass substrate. Although, the same process and parameters were used, instead of ZnO nanowires, nanosheets were observed under SEM. The observed change in structure can be attributed to the change in material from glass to gold. The observed results can be explained as follows. Hexagonal close-packed Zn and O atoms form the ZnO crystal structure. The wurtzite crystal structure of ZnO has six non-polar side facets and two polar top and bottom facets [18,19]. Each crystallographic plane has different polarity and, therefore, interacts quite differently with the organic adsorbate or surfactants [18,20]. ZnO crystal has preferential growth along the [0001] direction (c-axis), which led to forming the rod-like structure [19]. The gold thin film acts as a catalyst which not only lowers the surface energy of the developing nuclei but also, directs the crystallization by stabilizing specific crystal plane [21,22]. In this case, gold thin film stabilizes the polar planes of ZnO crystal, and thereby, suppresses the growth along the [0001] direction which led to the formation of ZnO nanosheets.

The composition of the ZnO nanosheets has been investigated using energy dispersive X-ray spectroscopy (EDX). The spectrum of collected EDX data, as shown in Figure 4.10, show almost the same peaks of ZnO nanosheets observed with ZnO nanowires with additional gold peaks. The data indicates that the ZnO nanosheets are composed of Zn and O, since the Au, Ca, Si, K peaks corresponds to the substrate.

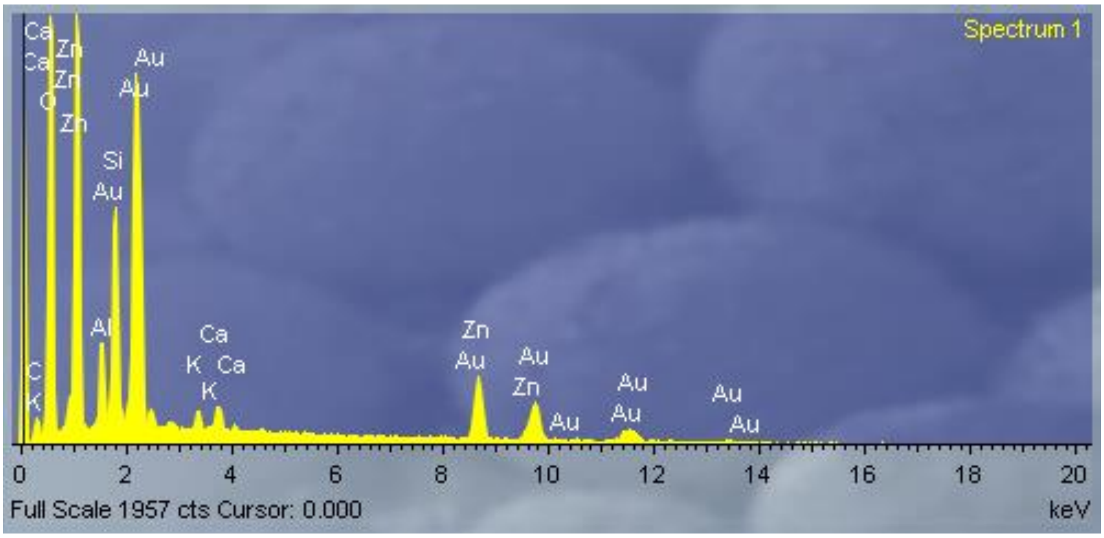

Figure 4.10 EDX spectrum of synthesized ZnO nanosheets on a gold coated glass slide.

4.6 Graphene

Graphene, a single atomic layer material, has tremendous application potential in the field of electronics, sensors, photonics and energy storage [23-25]. Chemical modification on graphene and graphene based hybrid materials is being extensively researched in order to explore their properties in various fields such as nanoelectronics, biosensors, drug delivery, supercapacitors, fuel cells, hydrogen storage, transistors, and polymer nanocomposites [26,27].

Graphene is considered as semi-metal or zero bandgap semiconducting material. A monolayer of graphene absorbs only 2.3% of white light [24]. Graphene has remarkably very high electron mobility 200,000 $cm^2V^{-1}S^{-1}$ [28]. Few layers of graphene have very good adsorption property, easy to functionalize by various covalent and non-covalent modifications and has large surface-to-volume ratio [23]. Several methods have been reported for the synthesis of graphene includes exfoliating graphite, chemical vapour deposition, unzipping of carbon nanotubes, epitaxial growth on silicon carbide or metal substrates [23].

A very high electron mobility of graphene has shown fast electron transfer rate of several orders of magnitude higher over the conventional glassy carbon electrode. Therefore, graphene and its composites have been used in the development of many electrochemical sensors for biosensing and environmental sensing applications [29].

Graphene and graphene oxide (GO) are known fluorescence quenchers. Based on the GO quenching effect Zhang and team have developed Hg^{2+} ion sensor using DNA duplexes of poly(dT) and GO. Developed sensor has achieved 0.5 nM Hg^{2+} detection limit [30]. Tang et al. have developed an electrochemical sensor to detect cadmium and lead using graphene coated platinum electrode [31]. Pb^{2+}, Cu^{2+} and Hg^{2+} ion sensor have been developed by Gong et al. [32] by functionalization of graphene oxide on the gold electrode and achieved two orders of improvement in the detection limit relative to the control electrode.

Wu et al. [33] have reported that graphene layers can increase the sensitivity of the SPR sensor. Verma et al. [34] have developed SPR based biosensor using silicon and graphene layers coated over conventional SPR film which has twice the sensitivity reported. SPR based fibre optic sensor has been developed coated with multi-layers of graphene by Kim and co-workers. The sensor has been used to analyse the interaction between structured DNA biotin and Streptavidin and reported excellent sensitivity [35]. Therefore, graphene has been selected as another material suitable for the development of hybrid sensor with excellent electrochemical and optical properties.

4.7 Surface Modification of Gold Thin Film by Graphene

Pristine graphene monolayer flakes (average lateral size ~550nm) suspended in ethanol (1mg/l) was purchased from Graphene Laboratories, Inc. Figure 4.11 shows the optical microscope images of the gold film with and without graphene flakes captured at 100x magnification. Graphene flakes can be seen on gold thin film as randomly distributed and shaped, light brown colour patches.

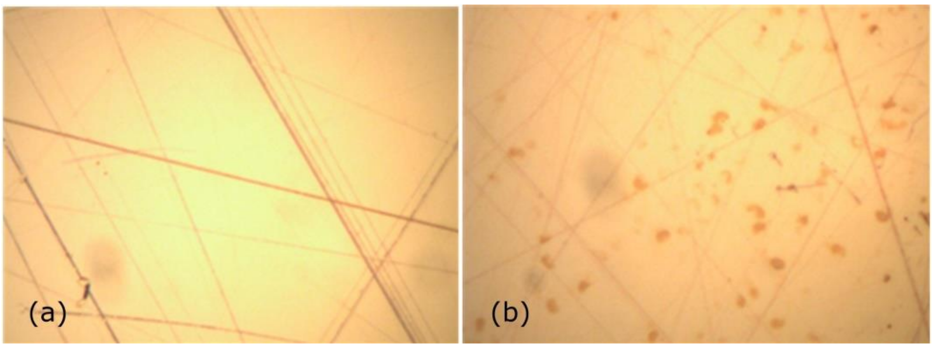

Figure 4.11 Optical images of the gold film with and without graphene monolayer flakes at 100x magnification.

A TEM image of the graphene flakes (shown in Figure 4.12) reveals that the graphene flakes have random shape and about 0.8-2 µm in size. There are three graphene flakes that can be seen in the image with some impurities. From the image contrast observations, two in the centre seems to be overlapped and are monolayers while one in the top left-hand corner seems to be multi-layered graphene (3-4 layers).

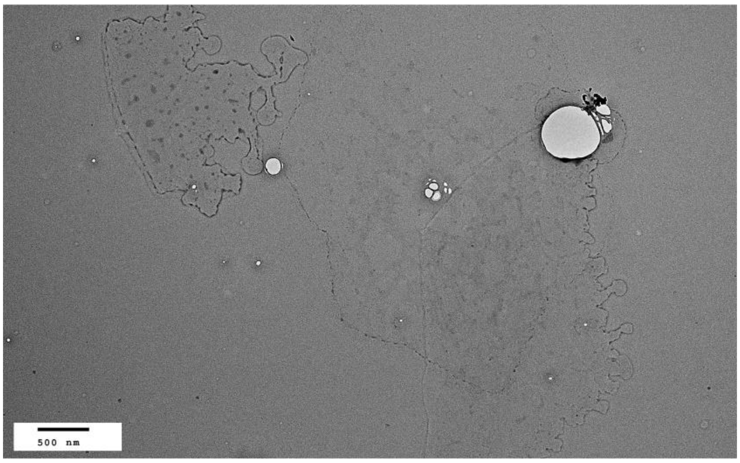

Figure 4.12 TEM image of graphene monolayer flakes

4.8 Wettability Effect on Sensitivity

In order to study the effect of this wettability on the sensitivity, a simple reflectance study of the white light was carried out under different wetting conditions of ZnO nanowires. Figure 4.13(a) shows the experimental setup for the reflectance measurement from the ZnO nanowire coated glass slide. The reflectance of around 93% has been observed from a water drop placed on the glass slide, which decreases to 24% for a ZnO nanowire coated glass slide (as shown in Figure 4.13(b)). The observed decrease in the reflectance can be attributed to the high refractive index of the ZnO. Also, it was observed that most of the light was confined to the ZnO layer (~ 10-12 µm). Thereafter, ZnO nanowires were exposed to the UV LED (365 nm) for 20 min which makes the ZnO nanowires hydrophilic. Measured reflectance on this hydrophilic ZnO NW coated glass slide was 20%. Observed further reduction in the reflectance can be attributed to change in wettability of the ZnO nanowires. The hydrophilic surface has enabled more surface area of interaction between ZnO NWs and water and therefore, more light was able to escape from the ZnO layer to the water droplet placed on it. Thereafter, ZnO nanowires were irradiated for further 2 hours which turns their surface into the super hydrophilic state. The reflectance measured on the super hydrophilic surface was close to the measured on a glass slide (91%) which indicates that water has totally penetrated into the groves of ZnO NWs. Therefore, it can be deduced that tuning the wettability of the ZnO nanowires allows more light to interact with the water through ZnO nanowire interface, which in turn enhances the sensitivity of the sensor surface.

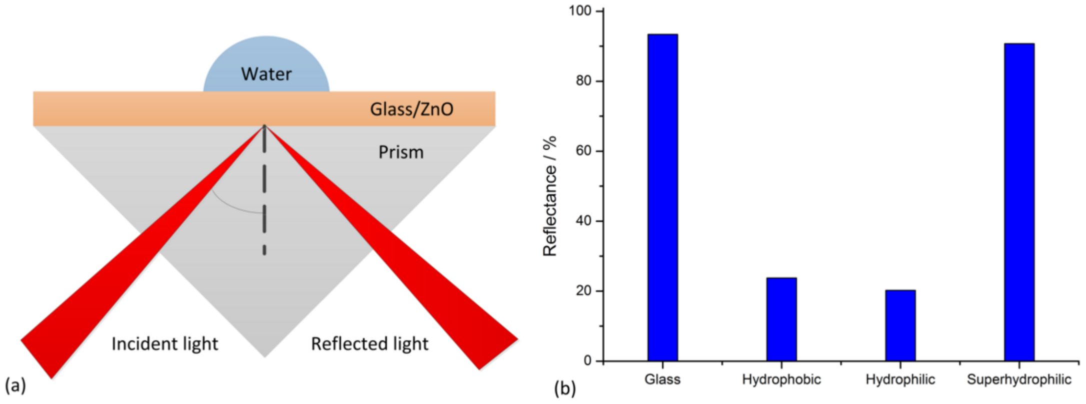

Figure 4.13 (a) A schematic of the experimental setup for the reflectance measurement and (b) plot of measured reflectance under different surface wetting conditions of ZnO nanowires.

4.9 Summary

Surface modifications of optical fibre and flat glass substrates coated with gold thin film have been carried out using ZnO nanostructures. Synthesized ZnO nanostructures are hydrophobic in nature and therefore, presumably decelerate the surface interactions in the aqueous environments. Modification in the wetting nature (hydrophobicity) shown by the ZnO nanowires can lead to improved surface interactions and hence, improved sensitivity for the developed sensor.

Hence, for the first time, work has been carried out on controlling the wetting nature of the ZnO nanostructure based surface using LEDs. The effect of irradiation wavelength and time on tuning the wettability of ZnO nanowires has been studied using different LEDs. Results show that the spectral overlap between ZnO absorption spectra and LED emission wavelength controls the hydrophobic-hydrophilic transition rate. Various controllable parameters of LEDs can provide advanced control in tuning the desired surface wettability of the ZnO nanowires and hence the high sensitivity.

Surface modification of the developed gold thin film has been presented. Results show a structural change of the nanostructures from nanowires to nanosheets. The surface of an optical fibre has been modified to enhance the sensitivity of the sensor using ZnO nanostructures. Graphene, a 2D material, has been proposed as another suitable material for the surface modifications. The surface of the gold thin film has been modified with graphene monolayer flakes and will be used in chapter 5 and in the development of electrochemical and optical sensors.

4.10 References

[1] M.I. Janssen, M.B.M. van Leeuwen, T.G. van Kooten, J. de Vries, L. Dijkhuizen, H.A.B. Wosten, Promotion of fibroblast activity by coating with hydrophobins in the beta-sheet end state, Biomaterials. 25 (2004) 2731-2739.

[2] A.W. Adamson, A.P. Gast, Physical Chemistry of Surfaces, 6th ed., Wiley, New York, 1997.

[3] G. Kwak, M. Seol, Y. Tak, K. Yong, Superhydrophobic ZnO Nanowire Surface: Chemical Modification and Effects of UV Irradiation, J Phys Chem C. 113 (2009) 12085-12089.

[4] R.D. Sun, A. Nakajima, A. Fujishima, T. Watanabe, K. Hashimoto, Photoinduced surface wettability conversion of ZnO and TiO2 thin films, J Phys Chem B. 105 (2001) 1984-1990.

[5] J. Li, H. Wan, X. Liu, Y. Ye, H. Zhou, J. Chen, Facile fabrication of superhydrophobic ZnO nanoparticle surfaces with erasable and rewritable wettability, Appl Surf Sci. 258 (2012) 8585-8589.

[6] G. Kenanakis, E. Stratakis, K. Vlachou, D. Vernardou, E. Koudoumas, N. Katsarakis, Light-induced reversible hydrophilicity of ZnO structures grown by aqueous chemical growth, Appl Surf Sci. 254 (2008) 5695-5699.

[7] Y. Liu, Z. Lin, W. Lin, K.S. Moon, C.P. Wong, Reversible superhydrophobic-superhydrophilic transition of ZnO nanorod/epoxy composite films, ACS Appl Mater Inter. 4 (2012) 3959-3964.

[8] H. Li, M. Zheng, S. Liu, L. Ma, C. Zhu, Z. Xiong, Reversible surface wettability transition between superhydrophobicity and superhydrophilicity on hierarchical micro/nanostructure ZnO mesh films, Surf Coat Technol. 224 (2013) 88-92.

[9] V. Khranovskyy, T. Ekblad, R. Yakimova, L. Hultman, Surface morphology effects on the light-controlled wettability of ZnO nanostructures, Appl Surf Sci. 258 (2012) 8146-8152.

[10] J. Lv, J. Zhu, K. Huang, F. Meng, X. Song, Z. Sun, Tunable surface wettability of ZnO nanorods prepared by two-step method, Appl Surf Sci. 257 (2011) 7534-7538.

[11] S. Nakajima, L. Lan, S. Kanno, M. Takao, K. Yamamoto, A. Eker, A. Yasui, Light-induced DNA damage and tolerance for the survival of nucleotide excision repair-deficient human cells, J Biol Chem. 279 (2004) 46674-46677.

[12] X. Wen, W. Wu, Y. Ding, Z.L. Wang, Seedless synthesis of patterned ZnO nanowire arrays on metal thin films (Au, Ag, Cu, Sn) and their application for flexible electromechanical sensing, J Mater Chem. 22 (2012) 9469-9476.

[13] C. Badre, T. Pauporte, M. Turmine, D. Lincot, A ZnO nanowire array film with stable highly water-repellent properties, Nanotechnology. 18 (2007) 365705.

[14] A.B.D. Cassie, S. Baxter, Wettability of porous surfaces. Trans Faraday Soc. 40 (1944) 0546-0550.

[15] R.N. Wenzel, Resistance of solid surfaces to wetting by water, J Ind Eng Chem. 28 (1936) 988-994.

[16] T. Young, An Essay on the Cohesion of Fluids, Philos T R Soc Lond. 95 (1805) 65-87.

[17] R. Wang, N. Sakai, A. Fujishima, T. Watanabe, K. Hashimoto, Studies of surface wettability conversion on TiO2 single-crystal surfaces, J Phys Chem B. 103 (1999) 2188-2194.

[18] S. Sun, X. Zhang, J. Zhang, X. Song, Z. Yang, Unusual Designated-Tailoring on Zone-Axis Preferential Growth of Surfactant-Free ZnO Mesocrystals, Crystal Growth & Design. 12 (2012) 2411-2418.

[19] A. Wei, X.W. Sun, C.X. Xu, Z.L. Dong, Y. Yang, S.T. Tan, W. Huang, Growth mechanism of tubular ZnO formed in aqueous solution, Nanotechnology. 17 (2006) 1740-1744.

[20] S. Cho, S. Jung, K. Lee, Morphology-controlled growth of ZnO nanostructures using microwave irradiation: From basic to complex structures, Journal of Physical Chemistry C. 112 (2008) 12769-12776.

[21] N.A.J.M. Sommerdijk, G. de With, Biomimetic CaCO3 Mineralization using Designer Molecules and Interfaces, Chem. Rev. 108 (2008) 4499-4550.

[22] M.M. Brewster, X. Zhou, S.K. Lim, S. Gradecak, Role of Au in the Growth and Nanoscale Optical Properties of ZnO Nanowires, Journal of Physical Chemistry Letters. 2 (2011) 586-591.

[23] W. Choi, I. Lahiri, R. Seelaboyina, Y.S. Kang, Synthesis of Graphene and Its Applications: A Review, Critical Reviews in Solid State and Materials Sciences. 35 (2010) 52-71.

[24] P. Avouris, Graphene: Electronic and Photonic Properties and Devices, Nano Letters. 10 (2010) 4285-4294.

[25] Q. Bao, K.P. Loh, Graphene Photonics, Plasmonics, and Broadband Optoelectronic Devices, Acs Nano. 6 (2012) 3677-3694.

[26] T. Kuila, S. Bose, A.K. Mishra, P. Khanra, N.H. Kim, J.H. Lee, Chemical functionalization of graphene and its applications, Progress in Materials Science. 57 (2012) 1061-1105.

[27] Y. Zhu, S. Murali, W. Cai, X. Li, J.W. Suk, J.R. Potts, R.S. Ruoff, Graphene and Graphene Oxide: Synthesis, Properties, and Applications, Adv Mater. 22 (2010) 3906-3924.

[28] X. Du, I. Skachko, A. Barker, E.Y. Andrei, Approaching ballistic transport in suspended graphene, Nature Nanotechnology. 3 (2008) 491-495.

[29] Y. Shao, J. Wang, H. Wu, J. Liu, I.A. Aksay, Y. Lin, Graphene Based Electrochemical Sensors and Biosensors: A Review, Electroanalysis. 22 (2010) 1027-1036.

[30] J.R. Zhang, W.T. Huang, W.Y. Xie, T. Wen, H.Q. Luo, N.B. Li, Highly sensitive, selective, and rapid fluorescence Hg2+ sensor based on DNA duplexes of poly(dT) and graphene oxide, Analyst. 137 (2012) 3300-3305.

[31] Tang Feng-Jie, Zhang Feng, Jin Qing-Hui, Zhao Jian-Long, Determination of Trace Cadmium and Lead in Water Based on Graphene-modified Platinum Electrode Sensor, Chinese Journal of Analytical Chemistry. 41 (2013) 278-282.

[32] X. Gong, Y. Bi, Y. Zhao, G. Liu, W.Y. Teoh, Graphene oxide-based electrochemical sensor: a platform for ultrasensitive detection of heavy metal ions, Rsc Advances. 4 (2014) 24653-24657.

[33] L. Wu, H.S. Chu, W.S. Koh, E.P. Li, Highly sensitive graphene biosensors based on surface plasmon resonance, Optics Express. 18 (2010) 14395-14400.

[34] R. Verma, B.D. Gupta, R. Jha, Sensitivity enhancement of a surface plasmon resonance based biomolecules sensor using graphene and silicon layers, Sensors and Actuators B-Chemical. 160 (2011) 623-631.

[35] J.A. Kim, A. Kulkarni, J. Kang, R. Amin, J. Choi, S.H. Park, T. Kim, Evaluation of Multi-Layered Graphene Surface Plasmon Resonance-Based Transmission Type Fiber Optic Sensor, Journal of Nanoscience and Nanotechnology. 12 (2012) 5381-5385.

Chapter 5

Investigations on Electrochemical Sensor Development

5 Investigations on Electrochemical Sensor Development

5.1 Introduction

Electrochemical sensors measure the electric charge transfer occurring due to the redox process of species on the surface of an electrode. During the redox process, deposition and removal of redox species occur on the surface of an electrode. Therefore, the physiochemical properties of the electrode surface play very crucial role in electrochemical sensors. In the development of hybrid sensor, the same electrode was used to detect the optical signal. Therefore, changes in physiochemical properties on the surface of an electrode not only influence the electrochemical signal but also the optical signal. Therefore, in order to develop the hybrid sensor, an electrochemical sensor developed and various investigations carried out are discussed in this chapter.

Heavy metal ions can be identified based on their specific redox potentials. Several papers have been reported on heavy metal ions detection using electrochemical sensors [1-5]. The redox process occurs on the surface of an electrode, therefore, parameters such as electrode material, their surface area, conductivity, and buffer solution which carries the analyte, their pH value, concentration and conductivity, and the electrode-solution interface plays very important roles in defining the sensitivity of the electrochemical sensors. In order to improve the sensitivity of an electrochemical sensor, nanomaterials such as carbon nanotubes, metal/metal oxide nanoparticles, graphene/graphene oxide were used to modify the surface of an electrode [6,7]. Nanomaterial modified electrode gives enhanced surface area and fast electron transfer rate and higher signal to noise ratio compared to the bulk electrode materials. Therefore, electrodes modified with nanomaterials have shown increased sensitivity and lower detection limits for the heavy metal ions [8].

Recently, graphene based electrochemical sensors have attracted significant interest due to its unique electronic properties [9-11]. Graphene has a wide potential window of 2.5 V in PBS buffer (pH 7) [10]. Graphene modified electrode exhibits a linear redox current variation with scanning rate in cyclic voltammetry (CV) and a higher electron transfer rate compared to glassy carbon (GC) electrode [11]. In the last decade, several papers have reported on graphene composites for electrochemical sensing applications [12-14]. Few papers have reported graphene composite based voltammetric detection of heavy metal ions such as zinc, lead, cadmium, copper, mercury [15-17]. Electrochemical detection of Cd(II), Pb(II), Cu(II) and Hg(II) have been carried out using SnO_2/reduced graphene oxide nanocomposite modified GC electrode [15]. Nafion-graphene nanocomposite modified GC electrode has been used to detect heavy metal ions [16]. Carboxyl functionalized graphene oxide film modified carbon paste electrode has been used to estimate the copper ions by Yuan and co-workers [18]. Graphene oxide terminated p-aminophenyl modified GC electrode [19] and graphene oxide functionalized with polyallylamine hydrochloride modified GC electrode [20] have been used to detect copper ions. But so far graphene flakes modified gold electrode is not investigated for copper ions detection. In this work, the effect of graphene flakes modified gold electrode was investigated in estimating the copper ion concentrations in phosphate buffer solution.

In this chapter, investigations on the development of an electrochemical sensor were carried out. To understand the dynamic behaviour of electrolyte molecules and metal ions in the near surface region of an electrode, redox process of copper ions has been studied. Effects of various parameters such as electrode material, surface area, concentrations, buffer conductivity, scan frequency and deposition time were investigated. Obtained results are used to understand the influence of the electric field on the dynamics of electrolyte molecules and metal ions near the surface of an electrode in optical detection. Graphene monolayer flakes modified gold electrode was investigated to estimate the copper ions concentrations in phosphate buffer and corresponding sensitivity enhancement.

5.2 Theory

A cyclic voltammetry (CV) is an important tool for the analysis of electrochemical processes associated with the analyte of interest in the aqueous solution. The characteristic peak location in forward and reverse scan, respective currents and their ratio and scanning rate give important information about the electrochemical processes. Experimentally, the cell potential is measured with respect to the reference electrode. Measured potential can be calculated by using the Nernst equation (eq. (5.1)) at room temperature [21]:

$$E = E^0 + \frac{RT}{nF} log \frac{[O]}{[R]} \qquad \text{... eq. (5.1)}$$

Where, *E* and *E*^{0} are the cell and standard electrode potentials, *n* is the number of electrons exchanged in process, [O] and [R] are the concentration of oxidized and reduced species respectively, R and T are the universal gas constant and temperature respectively. In order to understand the occurrence of these processes on the metal electrode, a schematic presentation of redox process is shown in Figure 5.1. The energy level of electrons of the metal electrode can be raised by driving the electrode at more negative potentials Figure 5.1(a). At a certain level, the energy becomes high enough that electrons can transfer into the lowest unoccupied molecular orbital (LUMO) electronic states of the analytes in the solution. This flow of electrons from the electrode to the analyte/solution represents the reduction currents and the corresponding potential called standard reduction potential of that analyte. Similarly, driving the potential to more positive level leads to the condition where the electrons of the analyte find more favourable condition and transfer to the electrode, as shown in Figure 5.1(b). This specific potential and corresponding current are referred to as oxidation potential and oxidation current of the analyte respectively and the process is called oxidation process.

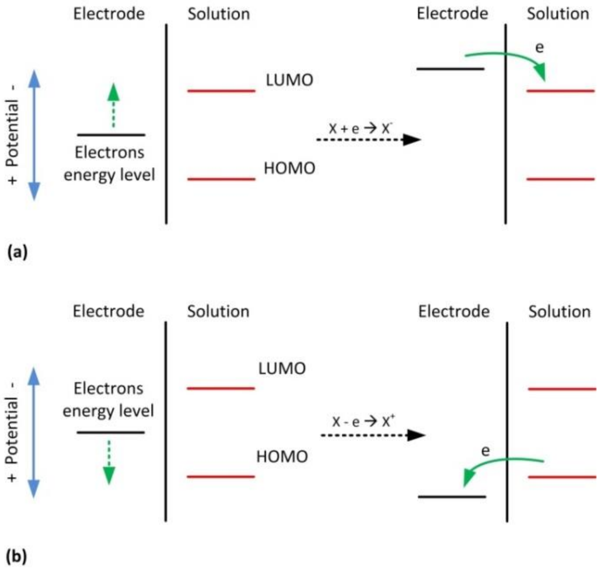

Figure 5.1 (a) Reduction and (b) oxidation process representation of analyte on the surface of a metal electrode.

Electrode-solution interface behaves like a capacitor, an element consisting of two metal plates separated by dielectric material. When the voltages are applied across the capacitor, charges get accumulated on the plates of the capacitor. The charge on electrode and charge in solution stays equal at all times at the electrode-solution interface. Capacitor behaviour is governed by the expression, C=q/E, where, C is the capacitance, q is the charge stored, and E is the applied potential. The solution also imposes the resistance on the movement of charges. Consider the resistance of the solution is R_s and the capacitance of the solution is C_s, the equivalent circuit [22] can be represented as shown in Figure 5.2.

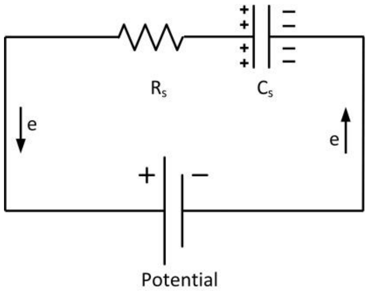

Figure 5.2 Equivalent circuit of a metal electrode-solution interface.

When the potential E is applied to the electrode, charge starts to accumulate on the capacitor which results into the flow of current referred to as charging current. This charging current, i_c with time can be expressed as (eq. (5.2)),

$$i_c(t) = \frac{E}{R_s} e^{-t/R_s C_s} \qquad \text{... eq. (5.2)}$$

This equation predicts the fundamental behaviour of the currents upon applied potential and the effects of various physical parameters on it.

Electrostatic interaction among the molecules of electrolyte/solution and metal ions creates the shell of adsorbed species around the metal ions in solution. At the electrode-solution interface, based on the electrode potential, counter ions/species in the solution forms a very thin layer at the interface, as shown in Figure 5.3. This layer acts as a blockage in the charge transfer process and hence, in most cases charge transfer occurs through tunnelling. Therefore, the strength of electrolyte, pH of the solution, dielectric constant of the solution, and the viscosity of the solution have effects on the movement of metal ions and hence on the redox potential and currents [21,22]. The movement of metal ions towards the electrode or the mass transfer process occurs through following modes: (a) migration, movement of metal ions under the influence of electric field, (b) diffusion, movement of metal ions due to concentration gradient in order to establish the equilibrium and (c) convection, movement due to the external forces such as stirring [22]. If the mass transfer processes are slower, then the redox currents become dependent on these processes, and therefore these redox currents are referred as mass transfer limited currents.

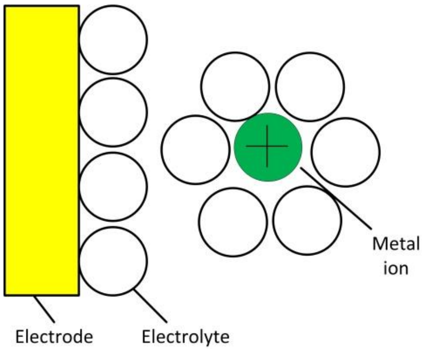

Figure 5.3 Schematic representation of metal electrode-solution interface with metal ions in solution.

Mass transfer limited currents can be given by the following expression (eq. (5.3)) [22]:

$$i = nFAmC \qquad \text{… eq. (5.3)}$$

where, *n* is the number of electrons transferred in the oxidation/reduction process, *A* is the surface area of the electrode, *m* is the mass transfer coefficient and *C* is the amount of species oxidized/reduced at the electrode. A standard gold disc electrode of 1.6 mm is widely used in voltammetry experiments, but for the SPR experiments 17 mm gold coated disc is used. Therefore, to estimate the range of currents when using SPR substrate as an electrode, currents were calculated for both the electrodes. Consider that 0-50mM copper ions get reduced on the surface of gold electrode having diameter 1.6 and 17 mm, $n = 2$ and $m = 0.01$ cm/s. Mass transfer limited currents calculated using eq.(5.3) are shown in Figure 5.4. In a millimolar range of concentrations, currents in the standard electrode will be less than 10 µA, while in the case of SPR substrate; currents may approach up to 200 µA.

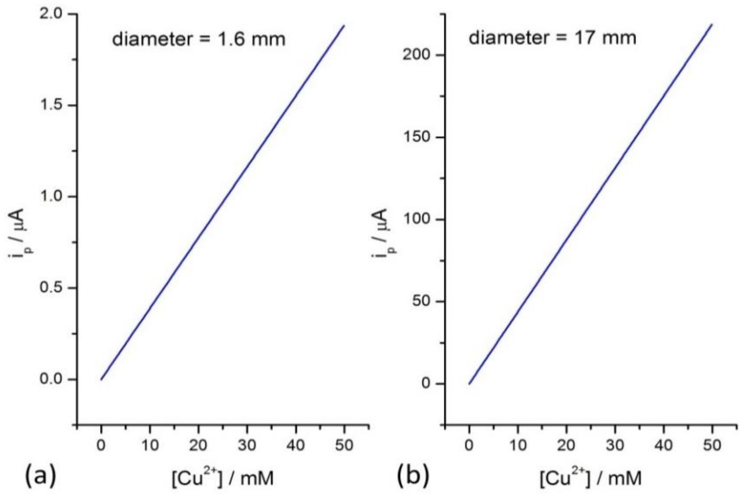

Figure 5.4 Copper ion reduction currents on gold disc standard (a) 1.6 and (b) 17 mm electrodes.

Anodic stripping voltammetry (ASV) is the most widely used method to detect heavy metal ions [21]. ASV involves two steps: (a) deposition of metal ions onto the electrode surface and (b) stripping of the deposited metal ions from the electrode surface. This simple method was used to detect the copper ions and various parameters were exploited in the experimental section.

5.3 Experimental

5.3.1 Chemicals

Analytical grade potassium chloride, copper (II) sulfate, mercury (II) sulfate, lead (II) nitrate, sodium phosphate dibasic dihydrate, sodium phosphate monobasic monohydrate and mercury and copper ion standard solutions in nitric acid were purchased from Sigma-Aldrich, UK and used without any further purification. All glassware was cleaned in deionized water prior to the experiment. All experiments were performed using Electrochemical Trace Analyser (Model- 394) from EG&G Instruments. All the experiments were carried out using Ag/AgCl/3M KCl reference electrode and a platinum wire as the counter electrode.

5.3.2 Cyclic Voltammetry

In order to first understand the redox behaviour of copper ions, cyclic voltammetry on the range of copper ions concentrations in PBS (pH 6.0) was carried out using GC electrode. Figure 5.5(a) shows the cyclic voltammogram of copper ions in PBS. It has been observed that the oxidation and reduction potentials shift with the concentration. This shift in oxidation and reduction potential was considered while developing the hybrid sensor which incorporates optical detection. Further, the trend of oxidation and reduction currents (as shown in Figure 5.5(b)) are similar indicating reversible oxidation and reduction process of copper ions. The oxidation currents are slightly higher than the reduction currents which can be attributed to the pre-deposited metal ions on the electrode. The trend line is the exponential fit to the obtained peak current data. The behaviour of currents were further analysed by calculating Ip_{ox}/Ip_{re} with concentration as shown in Figure 5.5(c). The exponential trend of oxidation and reduction currents and the exponential trend of their ratio indicate that the redox process is limited by the mass transfer of copper ions. Therefore, the observed exponential trend of redox currents can be attributed to the mass transfer limited diffusion currents as discussed in the theory (section 5.2).

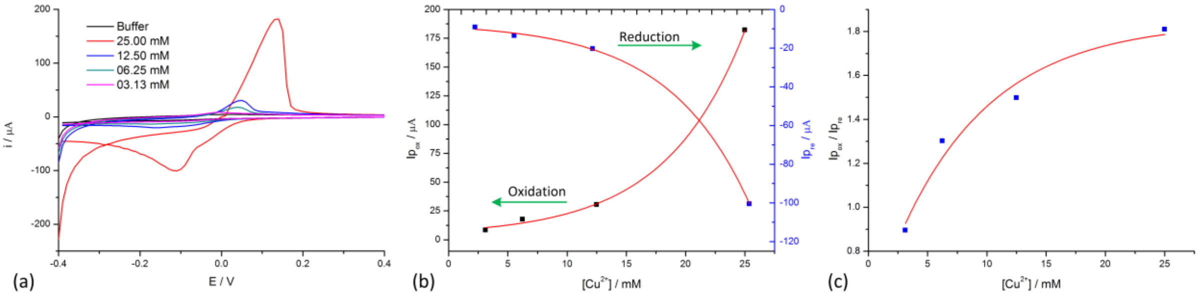

Figure 5.5 (a) Cyclic voltammogram of various copper ion concentrations in PBS and corresponding (b) trend of oxidation and reduction currents with concentrations. (c) The trend of Ip_{ox}/Ip_{re} with copper ion concentrations.

5.3.3 Square Wave Anodic Stripping Voltammetry

Copper ion concentrations were detected using the square wave stripping voltammetry in PBS (pH 5.8) as shown in Figure 5.6(a). The gold electrode was used to oxidise the deposited (for 30 s) Cu^{2+} ions on the electrode surface. It was observed that decreasing the concentration cause the increase in peak potentials and peak width. These effects can be attributed to the slower mass diffusion of copper ions. Figure 5.6(b) shows the trend of oxidation currents of Cu^{2+} ion concentrations. The trend line shown is the exponential fit to the obtained data. The exponential increase in currents can be attributed to the diffusion controlled process as discussed earlier [22].

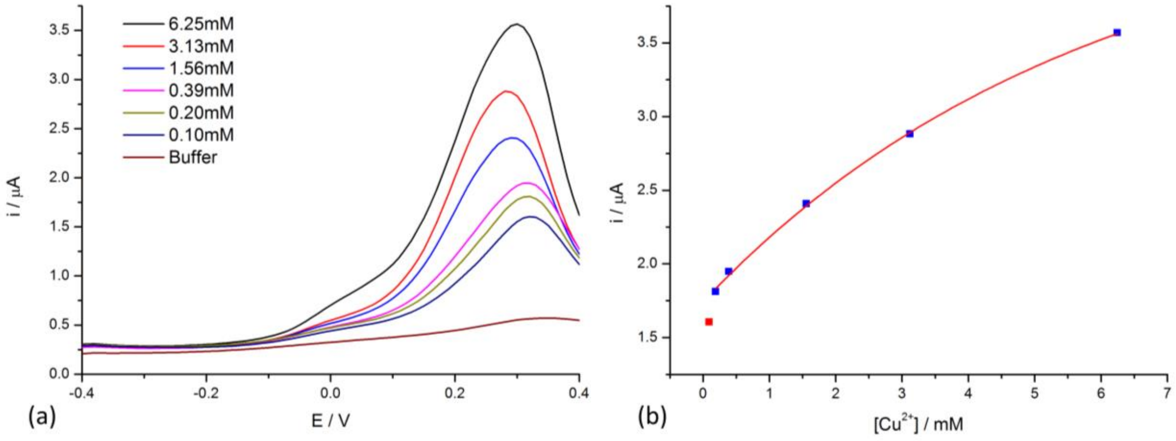

Figure 5.6 (a) SV scan of Cu^{2+} ion concentrations in PBS and corresponding (b) plot of stripping currents vs concentrations.

To detect the lower concentrations and overcome the lower current issue, deposition time was increased to 60 s. Increased deposition time has allowed more ions to be deposited on the electrode surface. Therefore, sweeping the voltage induces higher oxidation currents. With an increase in the deposition time, sub-nanomolar Cu^{2+} ion concentrations were detected as shown in Figure 5.7(a). It has been observed that lowering the Cu^{2+} ion concentrations cause the increase in oxidation potential and peak width. Figure 5.7(b) shows the plot of oxidation currents with Cu^{2+} ion concentrations. The trend line is the exponential fit to the obtained data. Observed effects were the same as seen with the higher concentration range, except the higher oxidation currents which was due to the longer deposition time [23].

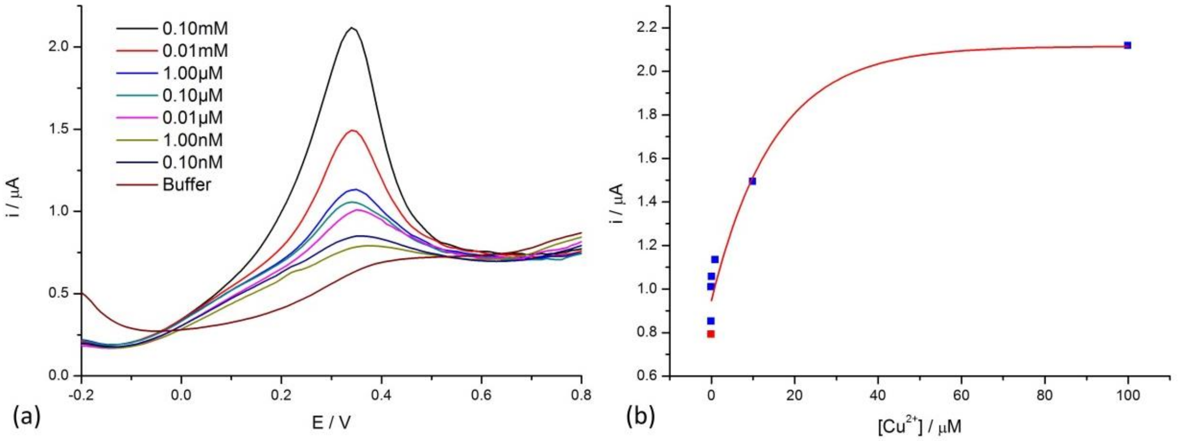

Figure 5.7 (a) SV scan of Cu^{2+} ion concentrations in PBS buffer at 60s deposition time and corresponding (b) trend of oxidation currents vs concentrations

5.3.3.1 Effect of deposition time

Further, to understand the effect of deposition time on the 0.1mM Cu^{2+} ion detection, a set of experiments were carried out in PBS (pH 5.8) for different deposition time using square wave stripping voltammetry as shown in Figure 5.8(a). A scan was carried out at 25 Hz with potential incremental steps of 10 mV. The Cu^{2+} ion oxidation peak observed at 0.33 V increases linearly with the deposition time from 10 to 90s, as shown in Figure 5.8(b). The observed increment in currents was due to the increased deposition time which allows more and more ions to be deposited on the electrode surface [23].

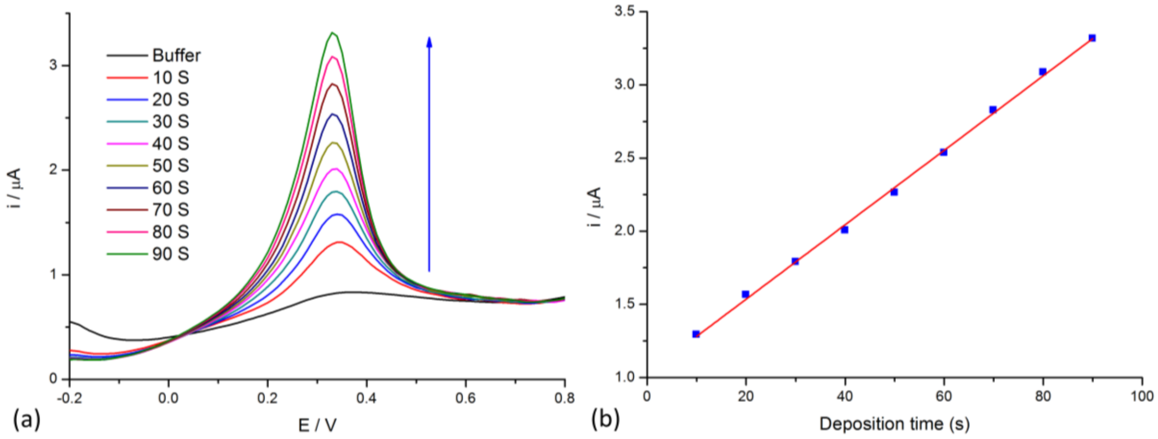

Figure 5.8 (a) SV scan of Cu^{2+} ion concentrations at different deposition time in PBS and corresponding (b) trend of oxidation currents with deposition time. Red line indicates linear fit to the data.

5.3.3.2 Effect of scan frequency

Effect of scanning frequency on the detection of copper ions was studied by changing the scanning frequency of applied square wave signal from 10 to 100 Hz. Figure 5.9 shows the square wave stripping signal of 3.13 mM copper ions in PBS (pH 6.0) using GC electrode. Prior to stripping, copper ions were allowed to deposit on the electrode for 30 s. Results indicate that an increase in the frequency leads to increased currents [23]. The observed shift in the oxidation potential can be attributed to the slower diffusion of copper ions. The concentrations ratio $[Cu^0]/[Cu^{2+}]$ near the electrode surface (oxidized and non-oxidized ions) starts unbalancing because of the difference in diffusion rate of incoming and outgoing species near the surface. This effect and rapidly increasing voltage forces the occurrence of secondary process where Cu -> Cu^{2+} transition undergoes to Cu -> Cu^{+} -> Cu^{2+} and is given by [21,24]:

(a) $Cu^{2+}_{(aq)} + 2e \rightarrow Cu_{(s)}$ (+0.34 V)

(b) $Cu^{2+}_{(aq)} + e \rightarrow Cu^{+}_{(aq)}$ (+0.16 V)

(c) $Cu^{+}_{(aq)} + e \rightarrow Cu_{(s)}$ (+0.52 V)

Three copper oxidation peaks have been observed at 0.04, 0.22 and -0.23 V corresponding to the processes (a), (c) and (b) for a 10 Hz frequency. Results indicate that the increase in frequency increased the occurrence of processes of (c) and (b). Therefore, in order to avoid the secondary species formation due to the detection process, careful selection of scanning frequency should be required.

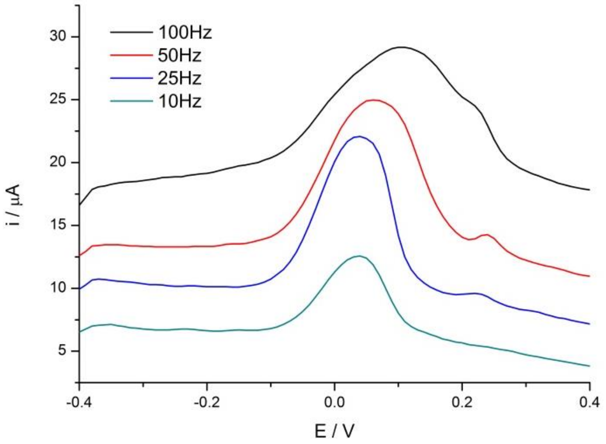

Figure 5.9 SV scan of 3.13mM Cu^{2+} ions in PBS at different scan frequency.

5.3.3.3 Effect of working electrode material

To analyse the effect of working electrode and its surface area, 3.13 mM copper ions in PBS (pH 6.0) were detected using gold and GC electrode. The diameters of the gold and GC electrode used were 1.6 and 3.0 mm respectively. Figure 5.10 shows the square wave (3.13 mM) Cu^{2+} stripping signal in PBS for gold and glassy carbon electrode. The result clearly indicates the change in current and shift in the reduction peak. Increase in current (1 μA to 17 μA) by replacing gold electrode with GC electrode was due to the increase in electrode surface area from 2.01×10^{-02} to 7.07×10^{-02} cm^2. The observed shift (from 0.24 to 0.05 V) of ~0.2 V in Cu^{2+} reduction peak was ascribed to the work function difference of gold and glass carbon [21].

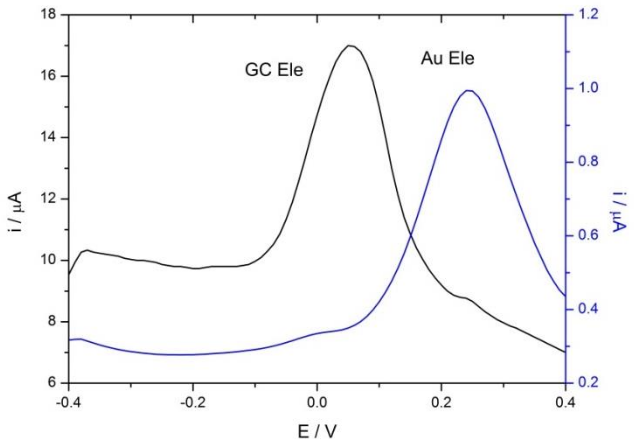

Figure 5.10 SV scan of 3.125mM Cu^{2+} ions using GC and Au electrodes in PBS.

5.3.3.4 Effect of buffer solution

It was observed that reference electrode starts oxidizing while detecting very low concentrations of the copper ions. The process of observed oxidation is expressed as [21]:

$Ag_{(s)} + Cl^{-}_{(aq)} + e \rightarrow AgCl_{(s)}$ (~ - 0.22 V)

Figure 5.11 shows an anodic stripping scan signal of PBS (pH 6.0) with and without 10 mM KCl using GC electrode. Oxidation peak of aqueous chloride ions in the Ag/AgCl reference electrode was observed at -0.19 V. To avoid the interference and oxidation of reference electrode while detecting the lower concentration of the copper ions, 10 mM KCl was added which increases the ionic conductivity of the buffer and therefore, prevents the oxidation of AgCl(s).

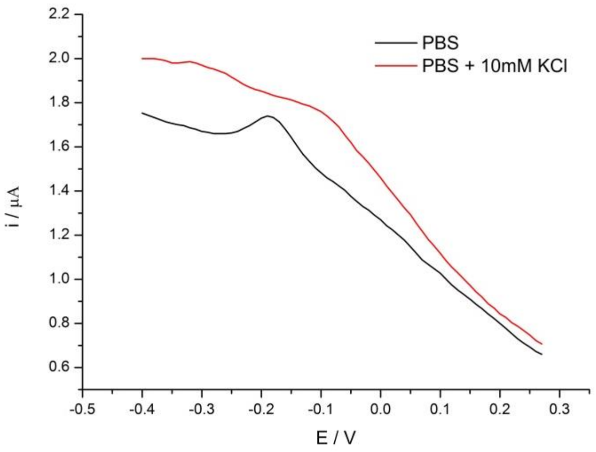

Figure 5.11 Effect of buffer solution in square wave voltammetry.

5.4 Multi-ion detection

In order to detect multiple heavy metal ions, 15.74 μM copper sulphate, 4.98 μM mercury (II) sulphate and 4.83 μM lead (II) nitrate were dissolved in PBS (pH 5.8). Figure 5.12 shows the anodic stripping signal of lead, copper and mercury ions in buffer solution using gold electrode. Prior to stripping the metal ions, they were deposited on the gold electrode for 30 seconds at -0.5 V potential. Result shows five oxidation current peaks at -0.068, 0.096, 0.408, 0.496 and 0.90 V correspond to different oxidation process of different metal ions. The oxidation current peak of lead and mercury ions were observed at -0.068 V and 0.90 V respectively [25]. Remaining three peaks correspond to the different oxidation process of copper ions as discussed in section (5.3.3.2).

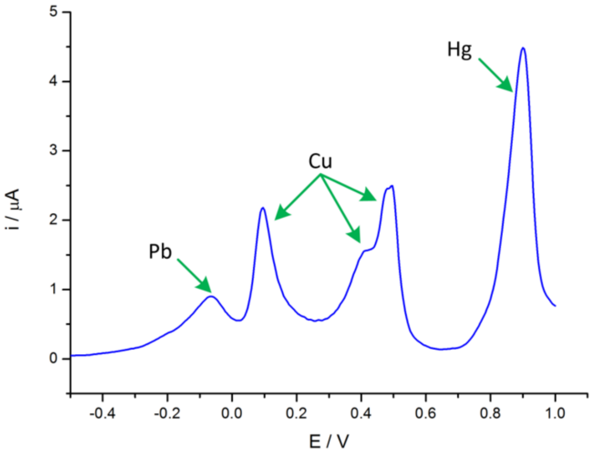

Figure 5.12 Lead, copper and mercury ion stripping signal in buffer solution using square wave anodic stripping voltammetry

5.5 Graphene Modified Electrode

The gold electrode was modified by drop casting pristine graphene monolayer flakes. The modified electrode was used to detect the copper ions. Effect of graphene on the copper ion detection was analysed. Figure 5.13(a) shows the plot of stripping current vs copper ion concentrations using bare and graphene modified gold electrode in PBS. Graphene flakes modified gold electrode shows higher detection currents for the copper ions concentrations in the range of 0.3-6.5 mM. The observed increase in the currents can be ascribed to the increased electron transfer rate by the graphene flakes [11,26].

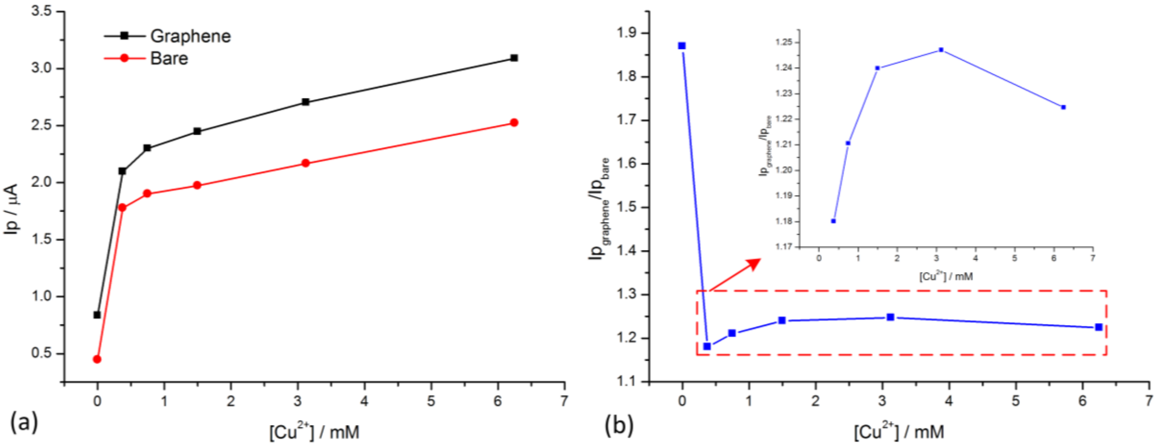

Figure 5.13 (a) Copper ion detection currents and (b) ratio of currents with a range of copper ion concentrations on a bare and graphene modified gold electrode. Pilot window shows expanded view of the currents ratio for copper ion concentrations.

Enhancements in the current *Ip* were analysed by taking the ratio of peak currents, $Ip_{graphene}/Ip_{bare}$, measured on bare and graphene modified gold electrodes for a range of copper ion concentrations, as shown in Figure 5.13(b). The current measured with graphene modified electrode was almost twice over the bare electrode in a buffer solution. However, lower enhancement was observed in the case of copper ion concentrations as shown in Figure 5.13(b) pilot window. Owing to the fact that graphene flakes do not cover the full surface of the gold electrode, the redox process occurs on both the areas, with and without graphene. With increase in copper ion concentration from 0.3 to 1.5 mM, currents produced by the copper oxidation on the graphene is larger than the remaining bare surface, thereby, causing the enhancement in the total observed currents. Further, increase in concentration causes more oxidation process to occur on the bare surface of an electrode, which leads to a small decrease in enhancement. Results suggest that an electrode fully covered with graphene can provide enhancement in redox currents and, therefore, improves the sensitivity of the electrochemical sensor.

5.6 Summary

An electrochemical sensor has been developed to detect the heavy metal ions. Effect of various parameters such as scanning speed, electrode materials, buffer solution, working electrode surface area and deposition time on the detection currents were investigated. Selectivity of multiple heavy metal ions was investigated by simultaneous detection of copper, mercury and lead ions. Graphene monolayer flakes modified gold electrode has been used to detect copper ions. Results have shown that graphene monolayer coated electrode improves the sensitivity of the copper ion sensor. Results from various investigations have provided a better understanding of near surface interactions of metal ions, solvent and electrode under the influence of applied electric field. Developed electrochemical sensor and investigations on the various parameters is used to further investigate their effects on optical detection in chapter 6.

5.7 References

[1] A. Afkhami, T. Madrakian, S.J. Sabounchei, M. Rezaei, S. Samiee, M. Pourshahbaz, Construction of a modified carbon paste electrode for the highly selective simultaneous electrochemical determination of trace amounts of mercury(II) and cadmium(II), Sensor Actuat. B-Chem. 161 (2012) 542-548.

[2] X.H. Gao, W.Z. Wei, L. Yang, T.J. Yin, Y. Wang, Simultaneous determination of lead, copper, and mercury free from macromolecule contaminants by square wave stripping voltammetry, Anal. Lett. 38 (2005) 2327-2343.

[3] B. Ogorevc, X.H. Cai, I. Grabec, Determination of Traces of Copper by Anodic-Stripping Voltammetry After its Preconcentration Via an Ion-Exchange Route at Carbon-Paste Electrodes Modified with Vermiculite, Anal. Chim. Acta. 305 (1995) 176-182.

[4] E. Saito, E.F. Antunes, H. Zanin, F.R. Marciano, A.O. Lobo, V.J. Trava-Airoldi, E.J. Corat, Oxygen Plasma Exfoliated Vertically-Aligned Carbon Nanotubes as Electrodes for Ultrasensitive Stripping Detection of Pb2+, J. Electrochem. Soc. 161 (2014) H321-H325.

[5] O. Abollino, A. Giacomino, M. Malandrino, G. Piscionieri, E. Mentasti, Determination of mercury by anodic stripping voltammetry with a gold nanoparticle-modified glassy carbon electrode, Electroanalysis. 20 (2008) 75-83.

[6] M. Govindhan, B. Adhikari, A. Chen, Nanomaterials-based electrochemical detection of chemical contaminants, RSC Advances. 4 (2014) 63741-63760.

[7] S. Su, W. Wu, J. Gao, J. Lu, C. Fan, Nanomaterials-based sensors for applications in environmental monitoring, Journal of Materials Chemistry. 22 (2012) 18101-18110.

[8] G. Aragay, A. Merkoci, Nanomaterials application in electrochemical detection of heavy metals, Electrochim. Acta. 84 (2012) 49-61.

[9] J. Chang, G. Zhou, E.R. Christensen, R. Heideman, J. Chen, Graphene-based sensors for detection of heavy metals in water: a review, Analytical and Bioanalytical Chemistry. 406 (2014) 3957-3975.

[10] M. Zhou, Y. Zhai, S. Dong, Electrochemical Sensing and Biosensing Platform Based on Chemically Reduced Graphene Oxide, Anal. Chem. 81 (2009) 5603-5613.

[11] Y. Shao, J. Wang, H. Wu, J. Liu, I.A. Aksay, Y. Lin, Graphene Based Electrochemical Sensors and Biosensors: A Review, Electroanalysis. 22 (2010) 1027-1036.

[12] J. Li, S. Guo, Y. Zhai, E. Wang, High-sensitivity determination of lead and cadmium based on the Nafion-graphene composite film, Anal. Chim. Acta. 649 (2009) 196-201.

[13] L. Jiang, S. Gu, Y. Ding, F. Jiang, Z. Zhang, Facile and novel electrochemical preparation of a graphene-transition metal oxide nanocomposite for ultrasensitive electrochemical sensing of acetaminophen and phenacetin, Nanoscale. 6 (2014) 207-214.

[14] M. Oyama, X. Chen, X. Chen, Recent Nanoarchitectures in Metal Nanoparticle-Graphene Nanocomposite Modified Electrodes for Electroanalysis, Analytical Sciences. 30 (2014) 529-538.

[15] Y. Wei, C. Gao, F. Meng, H. Li, L. Wang, J. Liu, X. Huang, SnO2/Reduced Graphene Oxide Nanocomposite for the Simultaneous Electrochemical Detection of Cadmium(II), Lead(II), Copper(II), and Mercury(II): An Interesting Favorable Mutual Interference, Journal of Physical Chemistry C. 116 (2012) 1034-1041.

[16] C.M. Willemse, K. Tlhomelang, N. Jahed, P.G. Baker, E.I. Iwuoha, Metallo-Graphene Nanocomposite Electrocatalytic Platform for the Determination of Toxic Metal Ions, Sensors. 11 (2011) 3970-3987.

[17] Z. Wang, H. Wang, Z. Zhang, X. Yang, G. Liu, Sensitive electrochemical determination of trace cadmium on a stannum film/poly(p-aminobenzene sulfonic acid)/electrochemically reduced graphene composite modified electrode, Electrochim. Acta. 120 (2014) 140-146.

[18] X. Yuan, Y. Chai, R. Yuan, Q. Zhao, C. Yang, Functionalized graphene oxide-based carbon paste electrode for potentiometric detection of copper ion(II), Analytical Methods. 4 (2012) 3332-3337.

[19] V.K. Gupta, M.L. Yola, N. Atar, Z. Ustundag, A.O. Solak, A novel sensitive Cu(II) and Cd(II) nanosensor platform: Graphene oxide terminated p-aminophenyl modified glassy carbon surface, Electrochim. Acta. 112 (2013) 541-548.

[20] H. Liu, S. Li, D. Sun, Y. Chen, Y. Zhou, T. Lu, Layered graphene nanostructures functionalized with NH2-rich polyelectrolytes through selfassembly: construction and their application in trace Cu(II) detection, Journal of Materials Chemistry B. 2 (2014) 2212-2219.

[21] P.J. Gellings, H.J. Bouwmeester, The CRC Handbook of Solid State Electrochemistry, CRC Press, London, 1997.

[22] C. Zoski, Handbook of Electrochemistry, 1st ed., Elsevier, Amsterdam, 2007.

[23] A.F. Alghamdi, Electrochemical oxidation behavior of hydrochlorothiazide on a glassy carbon electrode and its voltammetric determination in pharmaceutical formulations and biological fluids, J. Food Drug Anal. 22 (2014) 363-369.

[24] K.B. Yatsymyrsky, Ranges of oxidation states of d-transition metals in their complex compounds, Teoreticheskaya i Eksperimentalnaya Khimiya. 33 (1997) 284-290.

[25] W. Yantasee, Y.H. Lin, T.S. Zemanian, G.E. Fryxell, Voltammetric detection of lead(II) and mercury(II) using a carbon paste electrode modified with thiol

self-assembled monolayer on mesoporous silica (SAMMS), Analyst. 128 (2003) 467-472.

[26] R. Li, J. Zhang, Z. Wang, Z. Li, J. Liu, Z. Gu, G. Wang, Novel graphene-gold nanohybrid with excellent electrocatalytic performance for the electrochemical detection of glucose, Sensors and Actuators B-Chemical. 208 (2015) 421-428.

Chapter 6

Investigations on Development of Hybrid Sensor

6 Investigations on Development of Hybrid Sensor

6.1 Introduction

Development of electrochemical sensor to detect heavy metal ions has been investigated in chapter 5 and sensitivity has been improved using surface modification by graphene. Further, in order to develop the novel hybrid sensor, optical detection needs to be integrated with the same electrochemical sensor. In chapter 3, an evanescent field based optical sensing approach was already discussed using an optical fibre. The same evanescent field based effects is further exploited in this chapter.

Surface plasmon is the collective oscillation of free electrons on the metal surface or in other words, it's a propagating electron density waves at the metal-dielectric interface. These waves are bound to the interface and are highly sensitive to the changes in the refractive index of the surrounding environment. Under optimum thickness condition of the gold electrode used in the electrochemical sensor, evanescent field can be coupled to the surface plasmons of the gold thin film. This phenomenon has been used to develop the surface plasmon resonance (SPR) based sensor [1].

Investigations on developing surface plasmon based optical sensor on a planar substrate has been carried out and discussed in this chapter. Effect of graphene on the SPR sensitivity has been studied. Effect of wavelength and number of graphene layers on the sensitivity of SPR were analysed by theoretical calculations. Investigations on the development of an integrated hybrid sensor by combining electrochemical sensing with SPR have been carried out. Effect of PBS solution in hybrid sensing has been investigated. Effects of background currents, oxidation of gold and charged ions on the hybrid sensor have been investigated. Effect of ZnO coating on the sensitivity of the SPR sensor has also been studied computationally.

6.2 Surface Plasmon Resonance (SPR) Theory

An investigation on the evanescent field and approaches of enhancing their interaction with analyte towards the development of an optical fibre based sensor was discussed in chapter 3. In this chapter, the same effect has been extended to the surface plasmons, by replacing the second medium with a thin layer of metal, as follows.

An EM planar wave travelling in a medium with refractive index *n* can be expressed as (eq. (6.1)) [1],

$$E = E_0 exp(j\omega t - jk \cdot r) = E_0 exp\left(j\omega t - jk_x x - jk_y y - jk_z z\right) \qquad \text{… eq. (6.1)}$$

where, E_0 is the magnitude of EM field, ω is the angular frequency, *j* is the complex number; *k* and *r*, are wave and position vector, respectively.

The wave vector *k* can be expressed as (eq. (6.2)) [1],

$$k = \sqrt{k_x{}^2 + k_y{}^2 + k_z{}^2} = \frac{2\pi n}{\lambda} = \frac{n\omega}{c} \qquad \text{… eq. (6.2)}$$

Where, λ and *c* are the wavelength and velocity of the propagating light in vacuum and k_x, k_y and k_z are the wave vectors in *x*, *y* and *z* directions respectively.

Now, consider the case, where this travelling wave approaches an interface of two materials with refractive index n_1 and n_2 as shown in Figure 6.1, where the angle of incidence and refraction are α and β respectively. Applying the Snell's law (eq. (6.3)), we have [1]:

$$n_1 \sin\alpha = n_2 \sin\beta \qquad \text{… eq. (6.3)}$$

Here, considering the 2D interface, where, $k_z = 0$ and $k_{1x} = k_{2x} = k_x$

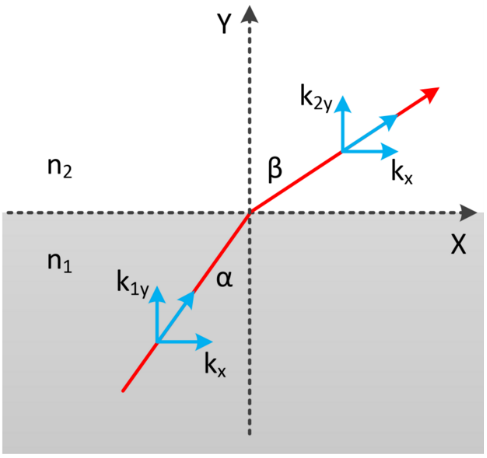

Figure 6.1 Light refraction at the interface of two materials.

Substituting and equating equation (6.1) and (6.2), the k_{2y} component of the propagation vector can be given by (eq. (6.4)) [1],

$$k_{2y}^2 = n_1^2 \left(\frac{2\pi}{\lambda}\right)^2 \left(\frac{n_2^2}{n_1^2} - sin^2\alpha\right) \qquad \text{… eq. (6.4)}$$

Assume that $n_1 > n_2$, k_{2y} becomes imaginary when sin$\alpha > n_2/n_1$. This indicates that the EM field becomes evanescent. Substituting these conditions in the equation (6.1), the EM field in the medium 2 can be expressed as (eq. (6.5)) [1],

$$E_2 = E_0 e^{-\kappa_{2y} y} exp(j\omega t - jk_x x) \qquad \text{… eq. (6.5)}$$

The expression means that electric field decays exponentially in the medium 2 perpendicular to the interface but a travelling wave exists in x direction bound to the interface. The magnitude of decaying electric field is given by $1/\kappa_{2y}$ Ξ $1/jk_{2y}$ and is referred as an evanescent field.

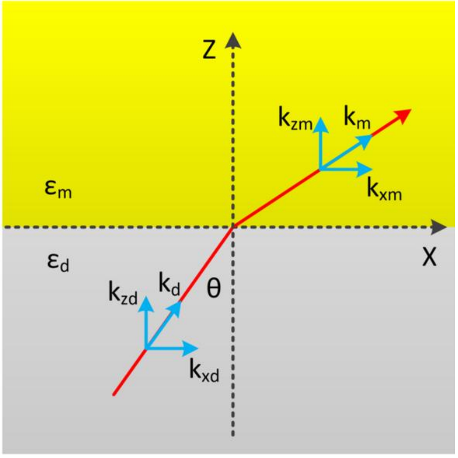

Figure 6.2 Light refraction at the metal-dielectric interface

To derive the dispersion relationship for a surface plasmon, we replace the second dielectric medium with a metal as shown in Figure 6.2.

The wave vector *k* can be expressed as (eq. (6.6)):

$$k_i = \sqrt{k_{xi}^2 + k_{zi}^2} = \frac{\omega}{c}\sqrt{\varepsilon_i} \qquad \text{… eq. (6.6)}$$

where, *i* can be replaced with *d* and *m* for the respective dielectric or metal wave vector. From the theory of dielectric interface, we know that under the TIR condition, k_{zm} becomes evanescent while k_{xm} is a propagating wave. Surface plasmon can be excited when k_{xd} = k_{xm} = k_{sp}. Therefore, using equation (6.6) k_{sp} can be expressed as (eq. (6.7)):

$$k_{sp}^2 = k_{xi}^2 = \left(\frac{\omega}{c}\right)^2 \varepsilon_i - {k_{zi}}^2 \qquad \text{… eq. (6.7)}$$

Substituting the boundary conditions where, $k_{zd}/\varepsilon_d = k_{zm}/\varepsilon_m$ and using equation (6.6) and (6.7), k_{sp} can be deduced to (eq. (6.8)),

$$k_{sp} = \frac{\omega}{c}\sqrt{\frac{\varepsilon_d \varepsilon_m}{\varepsilon_d + \varepsilon_m}} \qquad \text{… eq. (6.8)}$$

Dielectric constant of a metal ε_m can be defined as a function of angular frequency ω as (eq. (6.9)) [1]:

$$\varepsilon_m(\omega) = 1 - \frac{\omega_p^2}{\omega^2} \qquad \text{… eq. (6.9)}$$

where, ω_p is the plasma frequency given by (eq. (6.10)),

$$\omega_p = \sqrt{4\pi n_e e^2/m_e} \qquad \text{… eq. (6.10)}$$

where, n_e is the density of free electrons, e is the electric charge and m_e is the mass of an electron.

6.2.1 SPR Angle Calculation

Figure 6.3 shows the surface plasmon resonance sensor configuration [2], where the first layer is SF11 glass prism with refractive index n_1. The second layer is gold followed by a sensing aqueous medium. An incident light beam propagating through the prism undergoes total internal reflection at the prism-gold layer interface, generating an evanescent wave. The generated evanescent wave penetrates through the gold layer and propagates in the x direction.

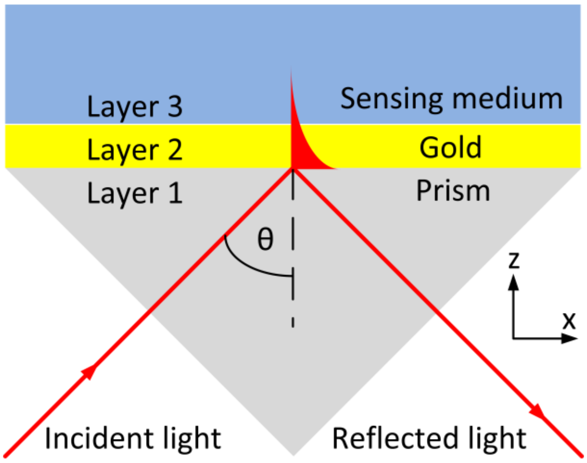

Figure 6.3 Surface plasmon resonance sensor configuration.

The magnitude of propagating wave vector in the x-direction can be expressed as (eq. (6.11)) [3],

$$k_x = \frac{2\pi n_1}{\lambda}\sin\theta \qquad \text{… eq. (6.11)}$$

Propagation vector of surface plasmon involves the refractive index of gold, n_2 and the sensing medium, n_3 because the wave propagation at the metal-surrounding medium interface occurs partly in both the material. Therefore, the surface plasmon propagation vector, k_{sp} can be defined as (eq. (6.12)) [3],

$$k_{sp} = \frac{2\pi}{\lambda}\sqrt{\frac{n_2^2 n_3^2}{n_2^2+n_3^2}} \qquad \text{… eq. (6.12)}$$

The surface plasmon polariton (SPP) can be excited by adjusting the incident angle θ, so that the propagation vector of the evanescent field, k_x, matches with the k_{sp}. Therefore, when this condition satisfies $k_x = k_{sp}$, reflected light intensity drops sharply. The reflectivity curve at this resonance condition referred to as SPR curve and the angle corresponding to the reflectivity minimum referred to as SPR angle θ_{spr} and is given by (eq. (6.13)),

$$\theta_{spr} = \sin^{-1}\left[\frac{1}{n_1}\sqrt{\frac{n_2^2 n_3^2}{n_2^2+n_3^2}}\right] \qquad \text{… eq. (6.13)}$$

6.2.2 Reflectance of N-layer Model

The reflectance of the p-polarized incident light was calculated using the N-layer model for the most common Kretschmann configuration [2] as shown in Figure 6.4.

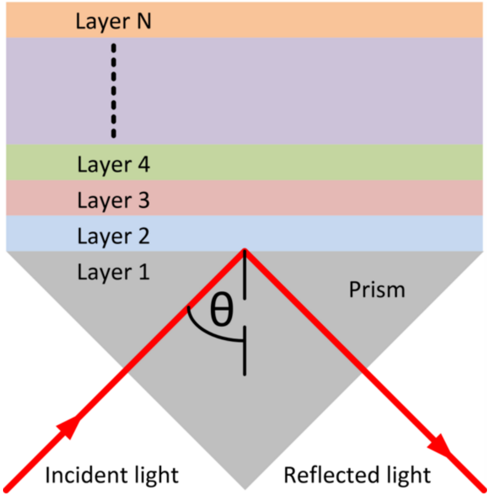

Figure 6.4 N-layer model for reflectance calculation.

Using a transfer matrix method, the reflectivity calculation was carried out for N-layered structure, where the m^{th} layer of thickness d_m, has a complex refractive index $n_{m,c} = n_m - ik_m$. The interference matrix of m^{th} layer can be expressed as (eq. (6.14)) [4],

$$M_m = \begin{bmatrix} M_{11} & M_{12} \\ M_{21} & M_{22} \end{bmatrix} = \begin{bmatrix} cos\beta_m & -i\ sin\beta_m/q_m \\ -iq_m sin\beta_m & cos\beta_m \end{bmatrix} \qquad \text{… eq. (6.14)}$$

where,

$$q_m = \frac{(\varepsilon_m - {n_1}^2 sin^2\theta)^{1/2}}{\varepsilon_m} \qquad \text{… eq. (6.15)}$$

$$\beta_m = d_m \left(\frac{2\pi}{\lambda}\right)(\varepsilon_m - {n_1}^2 sin^2\theta)^{1/2} \qquad \text{… eq. (6.16)}$$

The total interference matrix of the whole N-layered system can be obtained by [4], $M = \prod_{m=1}^{N} M_m$

Reflectance, R, of the N-layer stack can be obtained by (eq. (6.17)) [4],

$$R = \left|\frac{(M_{11}+M_{12}q_N)q_1-(M_{21}+M_{22}q_N)}{(M_{11}+M_{12}q_N)q_1+(M_{21}+M_{22}q_N)}\right|^2 \qquad \text{… eq. (6.17)}$$

In order to find the optimum thickness of the gold layer for the design of the sensor, range of reflectivity calculations were carried out for different thickness of gold layer (30-100 nm) for an incident wavelength in the range of 600-1000 nm. Results show that optimum thickness of the gold layer in the calculated wavelength range is in a range of 43-53 nm. Calculated results can be seen in appendix - IV.

6.3 Graphene and SPR Sensors

SPR is a well-known rapid and sensitive technique used for probing biomolecular interactions in real time. Several new approaches have been suggested to improve the sensitivity of SPR sensors over the last two decades [5,6]. Most of them are based on creating nanoparticles [7], nanowires [8], nanorings [9] nanoholes [5] and nanoslits [10] on the metal surface to enhance the localized E-field and therefore, it is quite challenging to have control over their optical properties [11].

Graphene, a single layer of carbon atoms arranged in a honeycomb structure, is emerging as the most popular material of the decade which is under intense research [12-15]. Graphene has a very high surface to volume ratio and strong binding/adsorption affinity towards biomolecules due to its carbon ring structure from π-π stacking interactions [13,16,17]. Recently, there have been few reports on using a graphene on the thin metal film based SPR sensor in order to improve the sensitivity [18]. But, so far to my knowledge, the role of wavelength on the sensitivity of the graphene based SPR sensors has not been investigated. In this work, investigations on wavelength effect on the sensitivity of graphene surface plasmon resonance sensor and relative sensitivity enhancement with an increase in graphene layers have been carried out using theoretical computations. The work was carried out by first understanding the surface plasmon resonance effect through theory and modelling work and thereafter, extending to graphene based SPR sensors.

6.4 Effect of Graphene on the Sensitivity of the SPR Sensor

Figure 6.5 shows graphene surface plasmon resonance sensor configuration. A propagating light through SF11 prism undergoes total internal reflection at the prism-gold layer interface, generating an evanescent wave. This generated evanescent wave penetrates through the 50 nm gold and graphene layers and propagates in the *x* direction. The reflectance of the p-polarized incident light has been calculated using the N-layer model for a most common Kretschmann configuration as described in theory [2].

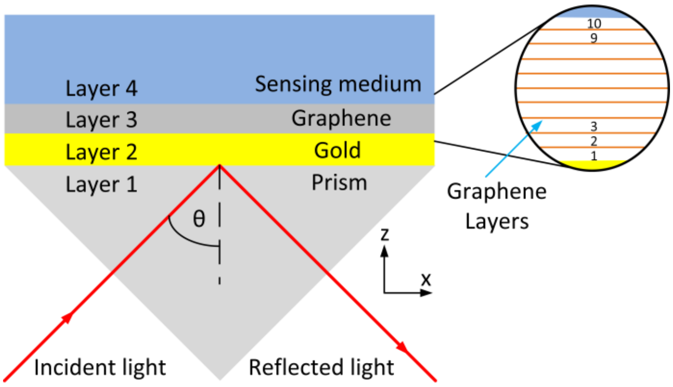

Figure 6.5 Schematic diagram graphene based SPR sensor

Sensitivity analysis has been carried out for a change in refractive index unit (RIU = 0.005) using 50 nm gold film coated on SF11 prism at 633 nm. Refractive index of SF11 prism and gold were 1.77858 [19] and 0.18344 + *i*3.4332 [20] respectively. Complex refractive index, n_3, of graphene can be expressed as (eq. (6.18)) [21]:

$$n_3 = 3.0 + i\frac{C}{3}\lambda \qquad \text{… eq. (6.18)}$$

where, C ≈ 5.446 μm^{-1} is the opacity constant [22], and λ is the wavelength in µm. A single layer of graphene has a thickness of 0.34 nm and hence, the thickness of L layers of graphene can be given by $d_3 = 0.34*L$ [21].

Figure 6.6 shows the effect of monolayer graphene on the reflectivity curve of SPR. The addition of monolayer graphene on gold film has caused the shift in the SPR angle ($\Delta\theta_{spr}$ = 0.22 deg) and an increase in the minimum reflectance by 1.54%. Sensitivity can be measured by change in θ_{spr} for the given change in refractive index. Sensitivity has been analysed by considering the change in refractive index (Δn = 0.005) of the aqueous solution which causes a shift in the SPR angle ($\Delta\theta^o$ = 0.352 deg) and therefore, sensitivity can be expressed as $S_{RIU}^0 = \Delta\theta^o/\Delta n$ = 70.4 for a conventional SPR sensor. A shift of $\Delta\theta^1$ = 0.355 has been observed for a monolayer graphene coated SPR sensor leading to the sensitivity $S_{RIU}^1 = \Delta\theta^1/\Delta n$ = 71. The SPR angle shift and sensitivity results indicate that the graphene coated SPR sensor has a higher sensitivity.

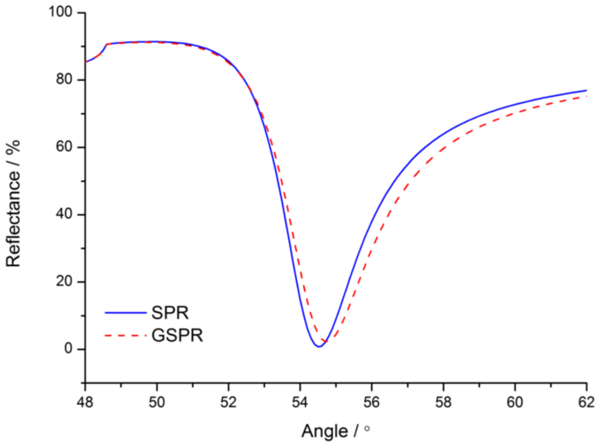

Figure 6.6 Reflectivity curve of the SPR sensor with and without monolayer graphene.

6.4.1 Sensitivity Enhancement using Multi-layered Graphene

To analyse the effect of multi-layers of graphene on the sensitivity, reflectivity calculations were carried out for a number of graphene layers, L = 1 to 10. A single layer of graphene absorbs 2.3% of light and each additional layer absorbs the same amount of light [22]. Therefore, the increase in the number of graphene layers cause the increase in thickness and absorption led to a shift to the higher plasmonic angles and broadening of the SPR curve, as shown in Figure 6.7(a). In order to analyse the sensitivity enhancement over a conventional SPR sensor, $\Delta S_{RIU}^{L} = S_{RIU}^{L} - S_{RIU}^{0}$ was calculated as a function of the number of graphene layers. Sensitivity enhancement is plotted as a function of graphene layers, L = 1 to 10, as $\Delta S_{RIU}^{L}/S_{RIU}^{0}$ as shown in Figure 6.7(b). Results indicate that increasing the graphene layers increases the sensitivity. However, increasing the graphene layers will broaden the SPR curve and may create difficulties in the detection; therefore, calculations were restricted to the 10 layers of graphene. The observed sensitivity enhancement can be attributed to the optical properties of graphene. The refractive index of graphene at 633 nm is $n_3 = 3 + i1.1491$. Therefore, the dielectric constant of graphene is $\varepsilon_3 = 7.6796 + i6.8946$. An increase in the number of graphene layers modifies the SPP in such a way that change in the SPR angle led to enhanced sensitivity.

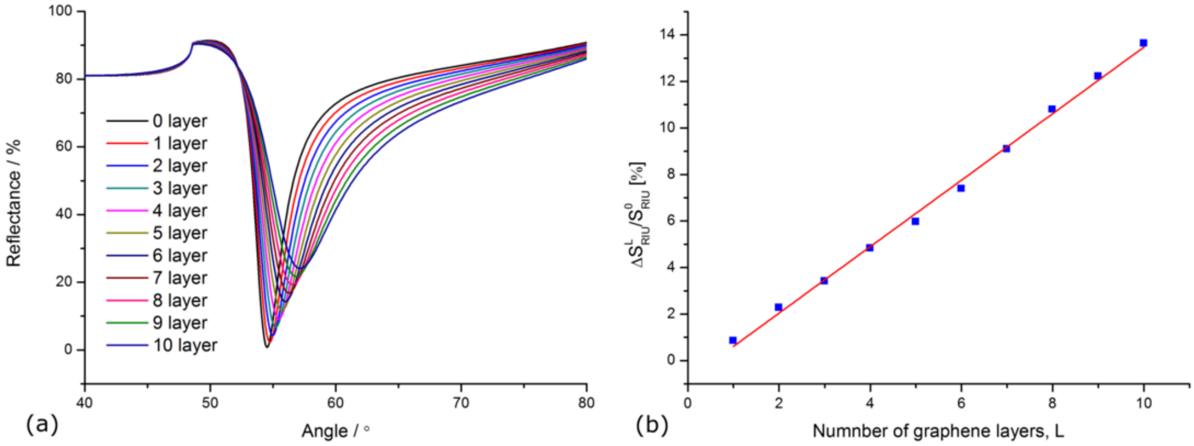

Figure 6.7 Reflectivity curve of the graphene based SPR sensor with increasing number of graphene layers L at λ = 633 nm. (b) Sensitivity enhancement $\Delta S_{RIU}{}^{L}/S_{RIU}{}^{0}$ with graphene layers over a conventional SPR.

6.4.2 Wavelength Effect on the Sensitivity Enhancements using Multi-layered Graphene

Further, to analyse the effect of wavelength on graphene based SPR sensors, reflectivity calculations were carried out for conventional and monolayer graphene coated SPR sensor. Various parameters used for the calculation are listed in Table 6.1.

Table 6.1 List of parameters used to calculate the reflectance of the SPR sensor

Wavelength	SF11 Prism [19]	Gold [20]			Graphene [21,22]		
λ(nm)	n_1	n_2	k_2	d_2(nm)	n_3	k_3	d_3(nm)
633	1.7786	0.1834	3.4332	50	3	1.1491	0.34
700	1.7718	0.1310	4.0624	50	3	1.2707	0.34
800	1.7646	0.1535	4.9077	50	3	1.4523	0.34
900	1.7596	0.1744	5.7227	50	3	1.6338	0.34
1000	1.7559	0.2277	6.4731	50	3	1.8153	0.34
1550	1.7434	0.5241	10.742	50	3	2.8138	0.34

Figure 6.8(a) shows the SPR curve with graphene monolayer at different wavelengths. It has been observed that increasing the wavelength reduces the FWHM of the SPR peak and also, lowers the SPR angle. Observed shift in the SPR angle can be attributed to the reduction in the refractive index of the prism.

Sensitivity analysis was carried out in order to analyse the effect of wavelength on the SPR sensor, as shown in Figure 6.8(b). Higher sensitivity has been observed for all the wavelengths (600-1600 nm) for the graphene based SPR over a conventional SPR sensor. A sensitivity of the graphene based SPR decreases with increasing wavelength and follows the same trend as for conventional SPR sensors.

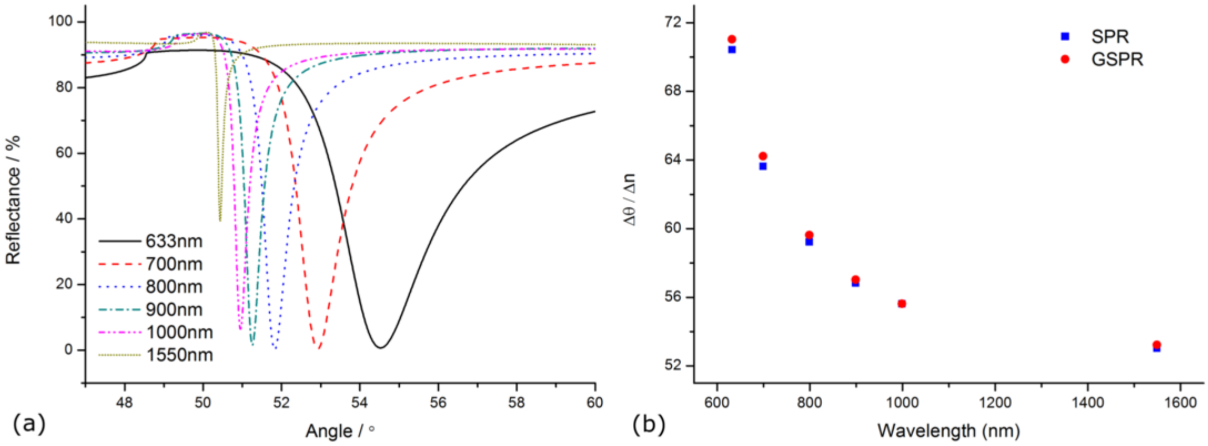

Figure 6.8 (a) Graphene SPR reflectance curve at various wavelengths and (b) corresponding sensitivity trend with and without monolayer graphene.

Further to see the effect of increasing the number of graphene layers and the relative enhancement over the conventional SPR, referred as $\Delta S_0^n/S$, reflectivity calculations were carried out for multi-layers of graphene at different wavelengths as shown in Figure 6.9. Results show that with an increase in a number of graphene layers sensitivity increases linearly for 10 layers of graphene while the increase in the wavelength causes a reduction in sensitivity. The observed increase in sensitivity with graphene layers can be attributed to the dielectric properties of the graphene while the decrease in sensitivity with wavelength can be attributed to the dielectric properties of the gold.

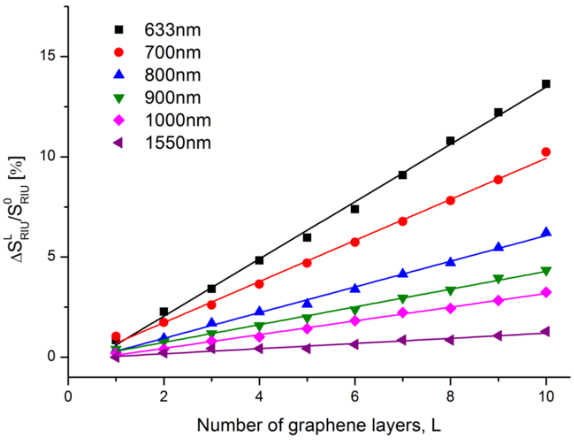

Figure 6.9 SPR sensitivity enhancement $\Delta S_{RIU}{}^{L}/S_{RIU}{}^{0}$ as a function of graphene layers at different wavelengths.

6.5 Experiments

6.5.1 Experimental Setup

Experimental investigations were carried out based on widely used Kretschmann and Raether [2] configuration (as shown in Figure 6.10). SF11 glass slides were purchased from HV Skan Limited, UK and were coated with (48 nm Au + 2 nm Ti) gold thin film by Ssens, Netherlands. SF11 prism was purchased from Edmund Optics, UK. Index matching fluid was purchased from Cargille Laboratories, USA. BK7 glass substrates and index matching fluid were purchased from Fisher Scientific, UK. A custom made sample cell and a holder assembly were used. (Drawings of the sample cell and holder assembly can be seen in appendix -V).

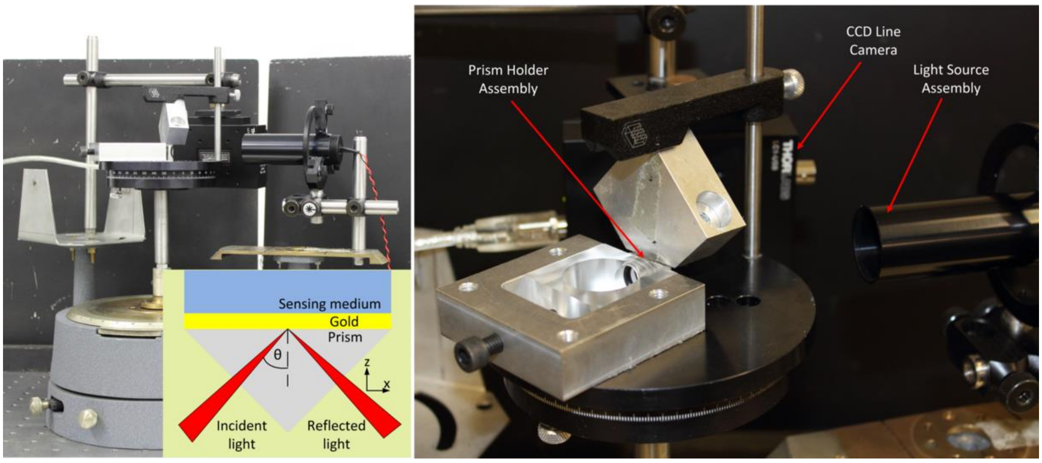

Figure 6.10 Experimental setup of the surface plasmon resonance sensor for an angular interrogated configuration.

Graphene monolayer flakes were deposited on the 50 nm gold thin film coated on BK7 glass substrate and refractive index matching fluid was used between the prism and glass substrate. A white light LED, polarizer and 633 nm narrowband filter were used to produce suitable light and a plano-convex lens was used to focus the light on the gold coated substrate through a right angled prism. Reflected light was collected on the high-resolution line camera (LC1-USB) from Thorlabs which works as a detector.

6.6 Results and Discussions

6.6.1 Effect of Multi-layered Graphene on SPR

Figure 6.11(a) and (b) show the calculated and measured reflectivity spectrum of the gold thin film with and without graphene. Measured reflectivity curve shows an increase in the reflectance minimum R_{min} and θ_{spr} upon deposition of graphene flakes on the gold film, which can be attributed to the optical properties of the graphene as discussed in the theory (section 6.2). Measured shift in the SPR angle was about 0.59 degree which corresponds to about 6 layers of graphene (Calculated SPR angle with graphene layers plot shown in the appendix - VI). Therefore, reflectance has been calculated and shown in Figure 6.11(a) with 6 layers on graphene. The observed difference can be attributed to the integrated effect of coated multiple multi-layered graphene flakes, as discussed in chapter 4. Also, during calculation, a uniform sheet of graphene was considered, but in the experiments graphene flakes were not uniform and randomly distributed, leaving some areas uncoated.

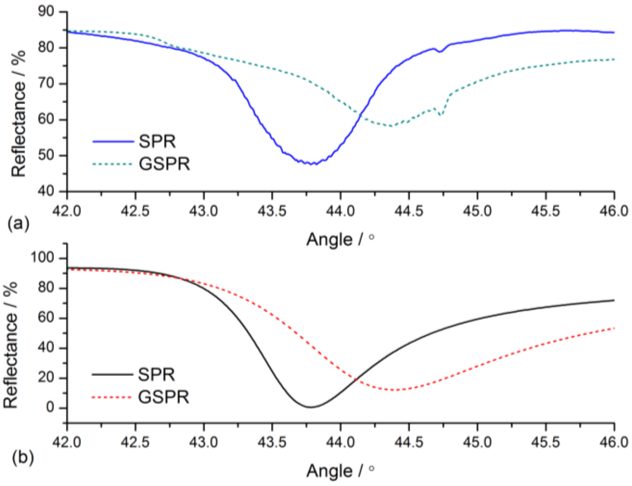

Figure 6.11 (a) Measured and (b) calculated SPR reflectance with and without graphene coating in air.

Therefore, these factors must have contributed to the observed difference in SPR angle. It has been also observed that the FWHM of the SPR peak has increased which can be attributed to the integrated effect of multi-wavelengths used (narrow band pass filter – 20 nm) as light source instead single wavelength used in calculation.

6.6.2 Effect of Phosphate Buffer Solution (PBS) on the SPR Reflectance

As discussed in the theory (section 6.2), SPR resonance angle depends on the complex dielectric constant of the gold thin film and the dielectric properties of the medium adjacent to the gold surface. When a medium contains charged ions, i.e. phosphate ions in the case of PBS, these charged ions form the Helmholtz double layer near the gold surface as discussed in the previous chapter. The formation of a double layer influences the response of SPR significantly. Therefore, SPR reflectance was measured in water and in PBS as shown in Figure 6.12. It was observed that the PBS provides an additional SPR angular shift, $\Delta\theta_{spr}$ = 0.46 degree towards higher angles. The observed angular shift and reflectivity change can be related to the change in dielectric constant and formation of charged double layer of phosphate ions on the gold surface [23].

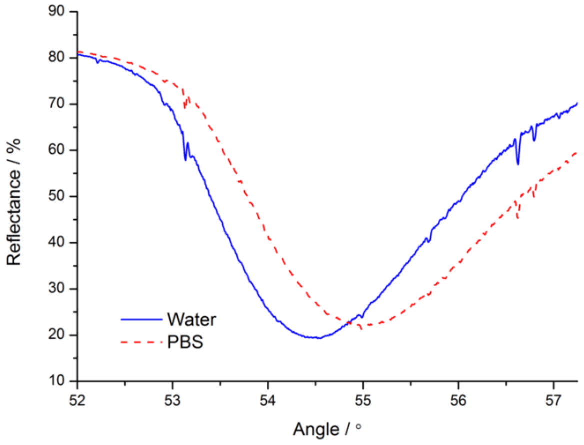

Figure 6.12 SPR reflectivity curve measured in water and PBS at 633 nm.

6.7 Investigations on Hybrid Sensing

Hybrid sensing has been realized by applying electrical signal to the developed optical system (SPR sensor). Labview based user interface was developed, as shown in appendix – VII, in order to provide electric potential and collect the optical signal through CCD array. Electrical signal interface was developed using the National Instruments USB 6009 data acquisition (DAQ) device. In order to study the effect of applied potential on the SPR reflectance curve, +2 V was applied to the gold electrode and the SPR reflectance collected. Figure 6.13 (a) shows the change in SPR reflectance over a period of 8 seconds. Results show that application of +2 V causes a shift in the SPR angle towards higher angles. While decreasing the potential back to 0 V, a reverse shift in the SPR angle towards the original position was observed (as shown in Figure 6.13 (b)). During this voltage cycling, several other processes must have taken place, such as change in electron density at the interface, adsorption and desorption of phosphate ions and oxidation of gold electrode. The observed shift can be primarily attributed to the local dielectric changes at the interfacial region below the gold oxidation potential (1.4 V) as reported by other groups [24-26]. Application of positive voltage attracts the additional ions and/or change in ionic cluster adsorbed on the surface which leads to the change of electron density in the vicinity of the gold surface and results in the observed shift in the SPR angle [24,27].

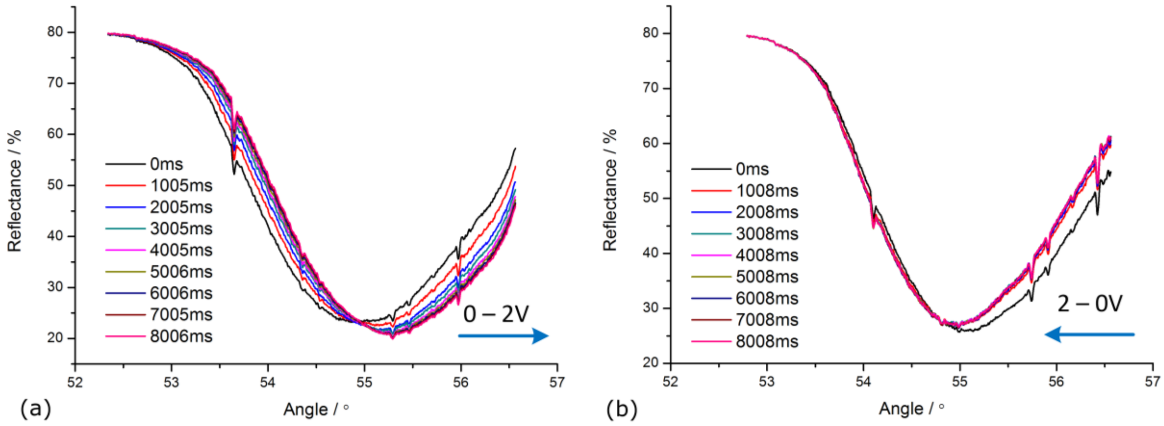

Figure 6.13 Time lapse of SPR curve measured upon the applied bias of (a) 0 to 2 V and (b) 2 to 0 V on the gold electrode in PBS.

The process of reduction occurs at some retarded potential than oxidation and henceforth, the observed trend of the SPR angle shift from 0-2 V and 2-0 V was different. Also, after completion of cycle 0-2-0 V, a shift in the SPR angle was observed which can be attributed to the thickness/roughness change upon the oxidation of gold coating [24,28].

In order to understand the effect on the SPR angle further, the potential was applied in the steps of 0.1 V from 0-2 V and corresponding SPR angles were measured, as shown in Figure 6.14. It was observed that SPR angle remains unchanged (nearly) below 1.4 V which indicates that SPR sensing is insensitive to the background currents as the background reactions below 1.4 V do not leave any solid products on the electrode surface [28,29]. Gold has an oxidation potential of 1.4 V, therefore, increasing the potential above 1.4 V must have led to the oxidation of gold coating causing the SPR angle to shift towards higher angles immediately, as seen in the Figure 6.14. Thereafter, potential was switched to 0 V from 2 V which stops the oxidation process and lowering the SPR angle immediately where ions starts to achieve equilibrium condition near the interface. Increasing the voltage from 0 to 0.1 V, ions in the PBS solution start to move towards the electrode and deposit on the electrode causing the shift in the SPR angle. Further, increase in potential cause the more ions to be deposited on the gold surface and thereby increasing the SPR angle. Further, recent study carried out by Beata and Daniel [30] has shown that an applied electric field perpendicular to the graphene pushes the positively charged ions closer to the graphene and increases the charge transfer which was observed in terms of sensitivity improvement in chapter 5. Graphene enhances the sensitivity of the SPR as investigated in this chapter and with the application of electric field, the ability to attract positively charged ions on the surface, further enhances the SPR sensitivity.

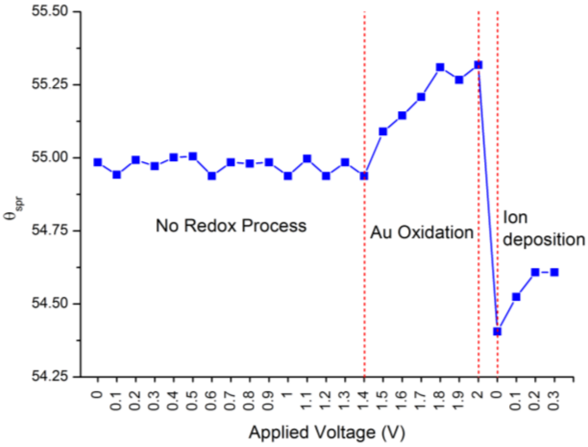

Figure 6.14 Trend of SPR angle movement with the applied voltage in PBS.

6.8 Sensitivity Enhancement of the SPR Sensor using ZnO Coating

Effect of ZnO coating on the SPR was evaluated by calculating the SPR reflectance for different thicknesses of ZnO coatings. Figure 6.15(a) shows the calculated SPR curves with thickness of ZnO coating (d_{ZnO}) varying from 0-35 nm for an incident light wavelength of 633 nm. The refractive index of the ZnO used for the calculation was 1.9888 at 633 nm [31,32]. Sensitivity $S_{RIU} = \Delta\theta / \Delta n$ has been calculated for different thicknesses of ZnO, as shown in Figure 6.15(b), (exponential fit was shown by red trend line). Sensitivity results indicate that ZnO coating provides higher sensitivity compared to the conventional and graphene SPR sensor and it increases exponentially in the range of 0-30 nm. However, increasing the ZnO coating thickness beyond 30 nm will broaden the SPR curve and may create difficulties in the detection, therefore, work have been restricted to a maximum of 35 nm. The enhanced sensitivity shown by the ZnO thin film coated SPR sensor can be attributed to the optical properties of the ZnO.

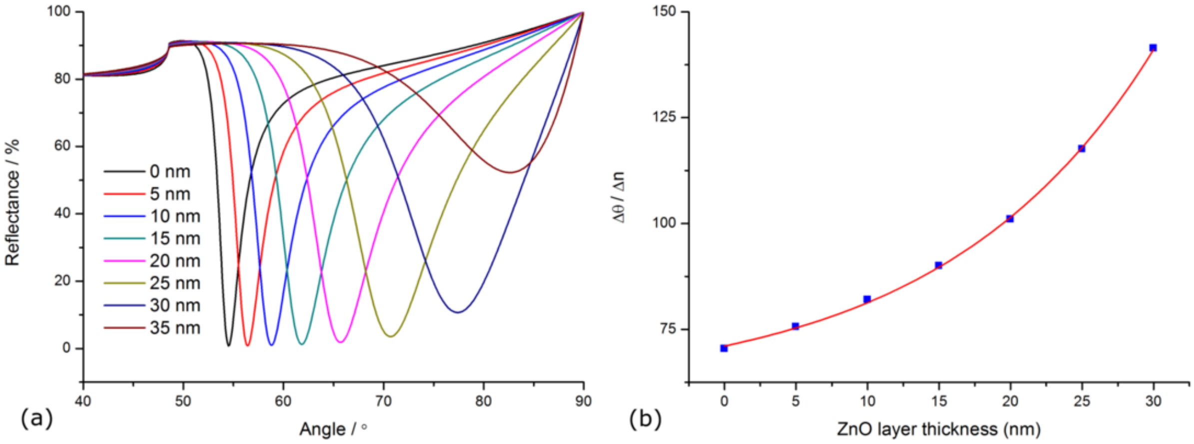

Figure 6.15 (a) Reflectance curve of ZnO coated SPR sensor with increasing thickness of ZnO layer and (b) corresponding sensitivity curve.

6.9 Summary

Hybrid sensor has been developed and preliminary investigations on hybrid sensing have been carried out and discussed. Sensitivity analysis of graphene coated SPR biosensor has been carried out using angular interrogated method. Computational results have shown that the graphene layer increases the sensitivity of the conventional SPR sensor for an incidence light wavelength in the range of 600-1600 nm. Relative sensitivity enhancement was carried out over a conventional SPR sensor with increasing number of graphene layers and results have shown an increase in sensitivity with the number of graphene layers. Also, ZnO coating based SPR sensor have been analysed through modelling work and was found that ZnO coating of thicknesses in the range of 20-30 nm show higher sensitivity compared to the graphene based sensors. Although, ZnO coating shows higher sensitivity through computation work, it assumes a flat and smooth surface which is not possible in reality. Therefore, to understand the effect of nanostructured surface of ZnO on the SPR sensor will be exploited in future work through experimental work. Preliminary results on the hybrid sensing have shown that the SPR signal was not affected by the background currents. Applied electrical signal improves the sensitivity by attracting more ions on the electrode surface. These investigations have opened up new possibilities for the real-time monitoring of highly sensitive molecular interactions studies using hybrid approach.

6.10 References

[1] R. Schasfoort, A. Tudos, Handbook of Surface Plasmon Resonance, Royal Society of Chemistry, Cambridge, United Kingdom, 2008.

[2] E. Kretschmann, H. Raether, Radiative Decay of Non Radiative Surface Plasmons Excited by Light, Zeitschrift Fur Naturforschung Part A-Astrophysik Physik Und Physikalische Chemie. A 23 (1968) 2135.

[3] Y. Tang, X. Zeng, J. Liang, Surface Plasmon Resonance: An Introduction to a Surface Spectroscopy Technique, J. Chem. Educ. 87 (2010) 742-746.

[4] H.R. Gwon, S.H. Lee, Spectral and Angular Responses of Surface Plasmon Resonance Based on the Kretschmann Prism Configuration, Materials Transactions. 51 (2010) 1150-1155.

[5] D. Kim, Nanostructure-Based Localized Surface Plasmon Resonance Biosensors, Optical Guided-Wave Chemical and Biosensors I. 7 (2010) 181-207.

[6] T. Wang, W. Lin, Electro-optically modulated localized surface plasmon resonance biosensors with gold nanoparticles, Appl. Phys. Lett. 89 (2006) 173903.

[7] J. Zhao, X. Zhang, C.R. Yonzon, A.J. Haes, R.P. Van Duyne, Localized surface plasmon resonance biosensors, Nanomedicine. 1 (2006) 219-228.

[8] D. Kim, Effect of resonant localized plasmon coupling on the sensitivity enhancement of nanowire-based surface plasmon resonance biosensors, Journal of the Optical Society of America A-Optics Image Science and Vision. 23 (2006) 2307-2314.

[9] E.M. Larsson, J. Alegret, M. Kall, D.S. Sutherland, Sensing characteristics of NIR localized surface plasmon resonances in gold nanorings for application as ultrasensitive biosensors, Nano Letters. 7 (2007) 1256-1263.

[10] K. Lee, C. Lee, W. Wang, P. Wei, Sensitive biosensor array using surface plasmon resonance on metallic nanoslits, J. Biomed. Opt. 12 (2007) 044023.

[11] L. Wu, H.S. Chu, W.S. Koh, E.P. Li, Highly sensitive graphene biosensors based on surface plasmon resonance, Optics Express. 18 (2010) 14395-14400.

[12] W. Choi, I. Lahiri, R. Seelaboyina, Y.S. Kang, Synthesis of Graphene and Its Applications: A Review, Critical Reviews in Solid State and Materials Sciences. 35 (2010) 52-71.

[13] P. Avouris, Graphene: Electronic and Photonic Properties and Devices, Nano Letters. 10 (2010) 4285-4294.

[14] Q. Bao, K.P. Loh, Graphene Photonics, Plasmonics, and Broadband Optoelectronic Devices, ACS Nano. 6 (2012) 3677-3694.

[15] A.K. Geim, K.S. Novoselov, The rise of graphene, Nature Materials. 6 (2007) 183-191.

[16] A.H. Castro Neto, F. Guinea, N.M.R. Peres, K.S. Novoselov, A.K. Geim, The electronic properties of graphene, Reviews of Modern Physics. 81 (2009) 109-162.

[17] Y. Zhu, S. Murali, W. Cai, X. Li, J.W. Suk, J.R. Potts, R.S. Ruoff, Graphene and Graphene Oxide: Synthesis, Properties, and Applications, Adv Mater. 22 (2010) 3906-3924.

[18] S. Szunerits, N. Maalouli, E. Wijaya, J. Vilcot, R. Boukherroub, Recent advances in the development of graphene-based surface plasmon resonance (SPR) interfaces, Analytical and Bioanalytical Chemistry. 405 (2013) 1435-1443.

[19] M. Polyanskiy N, Refractive index database, 2015. [Online] Available at: http://refractiveindex.info/?shelf=glass&book=SF11&page=SCHOTT [Accessed 3 Dec. 2015]

[20] P.B. Johnson, R.W. Christy, Optical Constants of the Noble Metals, Phys. Rev. B. 6 (1972) 4370-4379.

[21] M. Bruna, S. Borini, Optical constants of graphene layers in the visible range, Appl. Phys. Lett. 94 (2009) 031901.

[22] R.R. Nair, P. Blake, A.N. Grigorenko, K.S. Novoselov, T.J. Booth, T. Stauber, N.M.R. Peres, A.K. Geim, Fine structure constant defines visual transparency of graphene, Science. 320 (2008) 1308-1308.

[23] L. Dieguez, N. Darwish, M. Mir, E. Martinez, M. Moreno, J. Samitier, Effect of the Refractive Index of Buffer Solutions in Evanescent Optical Biosensors, Sensor Letters. 7 (2009) 851-855.

[24] A. Baba, R.C. Advincula, W. Knoll, In situ investigations on the electrochemical polymerization and properties of polyaniline thin films by surface plasmon optical techniques, J Phys Chem B. 106 (2002) 1581-1587.

[25] Y. Iwasaki, T. Horiuchi, M. Morita, O. Niwa, Time differential surface plasmon resonance measurements applied for electrochemical analysis, Electroanalysis. 9 (1997) 1239-1241.

[26] A. Tadjeddine, D.M. Kolb, R. Kotz, The Study of Single-Crystal Electrode Surfaces by Surface-Plasmon Excitation, Surf. Sci. 101 (1980) 277-285.

[27] Hochstra.Rm, Electric-Field Effects on Oriented Molecules and Molecular-Crystals, Acc. Chem. Res. 6 (1973) 263-269.

[28] T.M. Chinowsky, S.B. Saban, S.S. Yee, Experimental data from a trace metal sensor combining surface plasmon resonance with anodic stripping voltammetry, Sensors and Actuators B-Chemical. 35 (1996) 37-43.

[29] Y. Iwasaki, T. Horiuchi, M. Morita, O. Niwa, Analysis of electrochemical processes using surface plasmon resonance, Sensors and Actuators B-Chemical. 50 (1998) 145-148.

[30] B. Peles-Lemli, D. Kannar, J.C. Nie, H. Li, S. Kunsagi-Mate, Some Unexpected Behavior of the Adsorption of Alkali Metal Ions onto the Graphene Surface under the Effect of External Electric Field, Journal of Physical Chemistry C. 117 (2013) 21509-21515.

[31] W.L. Bond, Measurement of the Refractive Indices of Several Crystals, J. Appl. Phys. 36 (1965) 1674-1677.

[32] T. Voss, G.T. Svacha, E. Mazur, S. Mueller, C. Ronning, D. Konjhodzic, F. Marlow, High-order waveguide modes in ZnO nanowires, Nano Letters. 7 (2007) 3675-3680.

Chapter 7

Conclusions, Contribution and Recommendation

7 Conclusions, Contribution and Recommendation

7.1 Conclusions

A novel evanescent wave based fibre optic sensor was developed using dithizone to detect heavy metal ions. Effects of various environmental variables such as pH, reagent to analyte concentration ratio and simultaneous detection of multi-ions were investigated.

A U-bent sensor geometry was investigated to enhance the optical sensitivity of the sensor through higher evanescent field near the surface. Further, optical field confinement to the surface was investigated through thin film coating to improve the sensitivity. A new inverted trench design based sensor was developed. The sensitivity enhancement was achieved through this novel design and confirmed using modelling work accompanied by experimental results. Bend radius and trench width were found to be the most significant geometric parameters affecting the sensitivity in this novel sensor design, and therefore, optimum parameters were calculated and verified through experimental work.

A very high surface to volume ratio of the nanomaterials, such as ZnO nanowires, can provide enhanced surface interactions leading to higher sensitivity. Wettability of the material plays a crucial role in aqueous environments and therefore, wetting nature of the developed sensor surface modified with nanomaterials was investigated. Surface modified with ZnO nanostructures was found to be hydrophobic and hence, their wettability needs to be tuned to achieve higher sensitivity. A new remote and non-contact method to tune the wettability of the ZnO nanostructures using LEDs was developed. Vital parameters in controlling the wettability transition of the ZnO nanostructures were identified as the spectral overlap between LED emission spectrum and ZnO absorption spectrum which are previously unexploited. Higher sensitivity was achieved by tuning the wettability of ZnO nanowires using the developed method.

Electrochemical sensor was developed in order to understand the potential effects of the electric field on the near surface molecular dynamics and thereby, effects on the optical detection. Effects of parameters such as deposition time, scan frequency, concentration, electrode materials and their surface area were investigated to improve the sensitivity and selectivity. Multi-ions selectivity was achieved by simultaneous detection of copper, mercury and lead ions in buffer solution. Higher sensitivity was obtained by modifying the gold electrode using graphene flakes.

Furthermore, to integrate the optical field with this sensor, in order to develop the hybrid sensor, thickness of the gold electrode has been optimised to allow the penetration of evanescent field into the electrode. Under optimised conditions evanescent field resonantly couples to the surface plasmon of the gold electrode. Investigations have been carried out using computational work on a developed surface plasmon resonance (SPR) based optical sensor (integrated with the electrochemical sensor) to improve their sensitivity using nanomaterials. Sensitivity enhancement of the SPR has been studied using graphene and found that sensitivity of the SPR sensor can be enhanced with increasing the number of graphene layer up to ten. Computational results show that graphene increases the sensitivity of the conventional SPR sensor for an incidence light wavelength in the range of 600-1600 nm. Computational results have also shown that ZnO coating improves the sensitivity of the SPR sensor. Preliminary investigations on the developed hybrid sensor have shown that the electric field complements the optical detection. Investigations have shown that the application of electric field enhances the sensitivity in optical detection by attracting more ions on the electrode and also, provides the multi-ion selectivity. These investigations have opened up new possibilities for the real-time monitoring of highly sensitive and selective molecular interactions and have a lot more potential for a range of applications in the areas of environmental sensing, biosensing and agriculture.

7.2 Contribution to Knowledge

The research work reported in this thesis has made a number of significant contributions in the sensor development. The first contribution is the novel use of dithizone, a well-known chromogenic ligand, in the detection of mercury ions using an evanescent field. Initial results from the work have been published in Fifth Scottish Postgraduate Symposium on Environmental Analytical Chemistry and won the best poster award for the contribution. The second contribution is the extension of the same work for other heavy metal ions detection and development of optical fibre based heavy metal ion sensor using dithizone. Results have been published in the Sensors and their Applications XVII [1].

A novel inverted trench design based sensor was developed to achieve higher sensitivity. Initial results of the research work carried out were presented in 4th EOS Topical Meeting on Blue Photonics - Optics in the Sea (Blue Photonics 4).

For the first time graphene monolayer flakes modified gold electrode has been used to detect copper ions and effects of graphene monolayer flakes on the detection currents has been reported.

A computational study on the effect of wavelength and graphene layers on sensitivity of an angularly interrogated surface plasmon resonance (SPR) sensor has been reported. Results have been presented in Optical wave and Waveguide Theory and Numerical modelling Workshop (OWTNM-2015).

A new remote and non-contact method to tune the wettability of the ZnO nanostructures using LEDs has been developed. Results have been presented in the International Conference on Structural Nano Composites (Nanostruc2014) [2] and published in Nano Reviews [3].

7.3 Future Work

The investigations carried out in the development of novel hybrid sensor have largely been met the primary objectives, but looking forward, there are several recommendations necessary for the future work in the development of integrated hybrid sensor system for environmental monitoring applications.

Although, the modelling work on SPR coated with graphene layers and ZnO has shown the sensitivity enhancements, the work does not include the effect of the non-linearity in the graphene and ZnO surface, practical coating problems and, therefore, needs to be investigated. Also, the use of a combination of graphene and ZnO coatings may enhance the sensitivity further. Also, in the ZnO coated SPR sensor for the sensitivity enhancement assumes a uniform thin layer of ZnO, but, the role of nanostructures instead flat coating requires investigations.

Further work needs to be carried out on developing the uniform and dense ZnO nanowire coating on an optical fibre. Detection of heavy metal ions using dithizone immobilized ZnO nanowire coated fibre needs to be investigated. Also, the wettability tuning of the ZnO nanowire coated on an optical fibre needs to be investigated upon UV light interaction which propagates through the fibre core.

Fluorescence based detection eliminates the need for reference light beam and is more sensitive. Therefore, in order to incorporate the fluorescence based optical sensing along with the developed hybrid approach, FRET based mechanism for copper ion detection have been investigated and results have been discussed in chapter 2. The work carried out can be explored for the hybrid sensing which will improve the sensitivity of the developed hybrid sensor further.

7.4 Reference

[1] K. Bhavsar, R. Prabhu, P. Pollard, Development of dithizone based fibre optic evanescent wave sensor for heavy metal ion detection in aqueous environments, Journal of Physics: Conference Series. 450 (2013) 012011.

[2] K. Bhavsar, R. Prabhu, P. Pollard, Investigations on surface wettability of ZnO nanowires using UV LEDs for biosensing applications, IOP Conf. Ser. : Mater. Sci. Eng. 64 (2014) 012033.

[3] K. Bhavsar, D. Ross, R. Prabhu, P. Pollard, LED-controlled tuning of ZnO nanowires' wettability for biosensing applications. Nano reviews. 6 (2015) 26711-26711.

Appendix

I. Normalized UV/Vis Absorption spectra of dithizone in different solvents

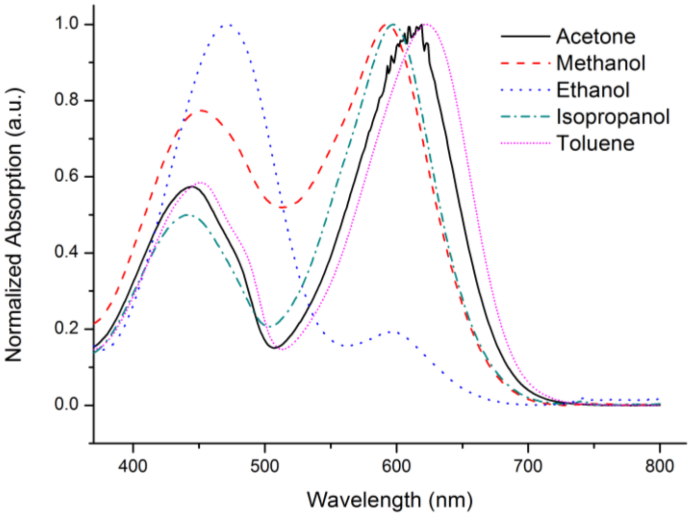

II. Dithizone binding study on the surface of ZnO NPs using absorption spectra

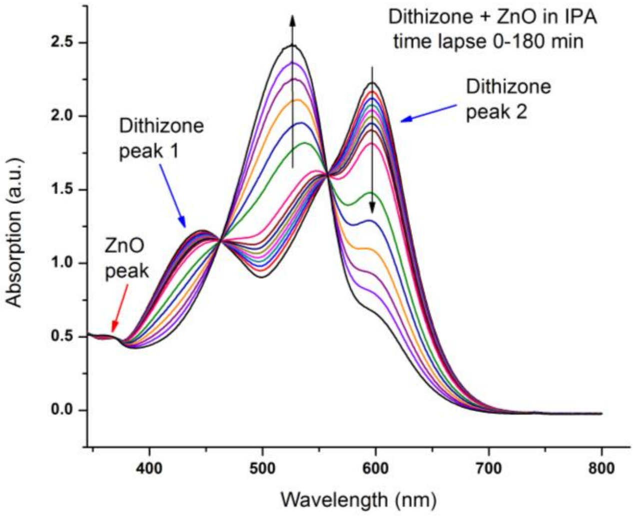

III. Recovery of dithizone from the mercury dithizonate solution by varying the pH of a solution.

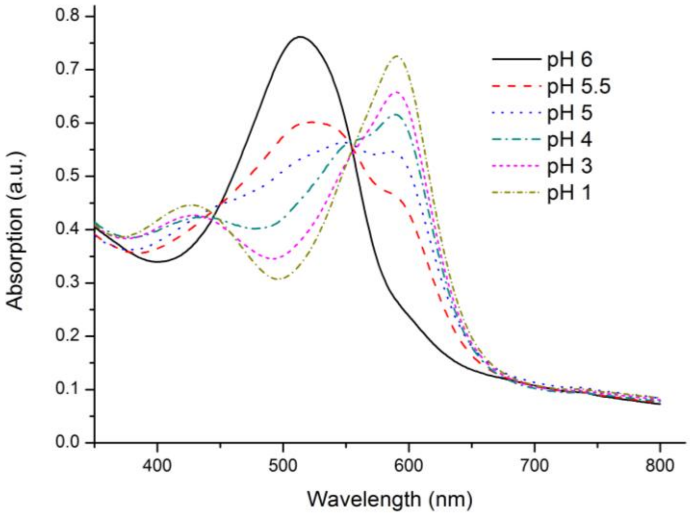

IV. SPR Reflectivity minimum with different gold layer thickness at different wavelengths

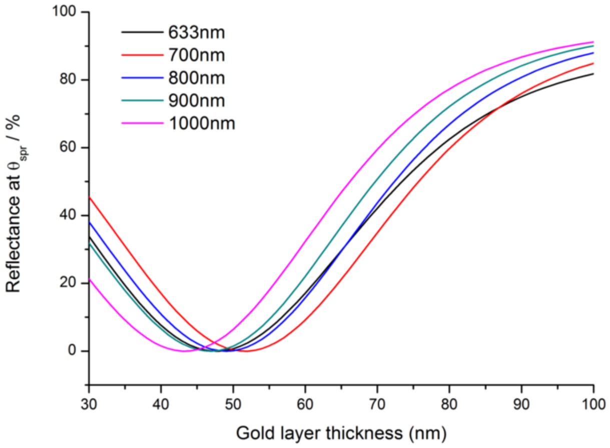

V. SPR fluidic cell design drawings

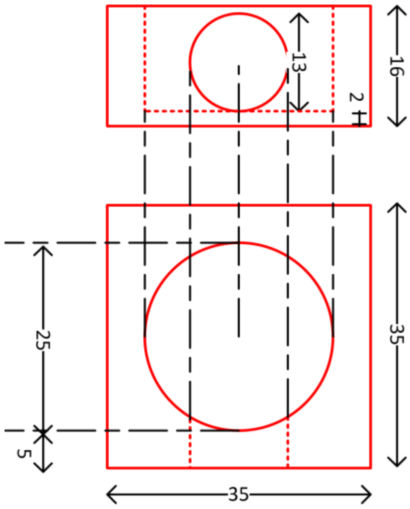

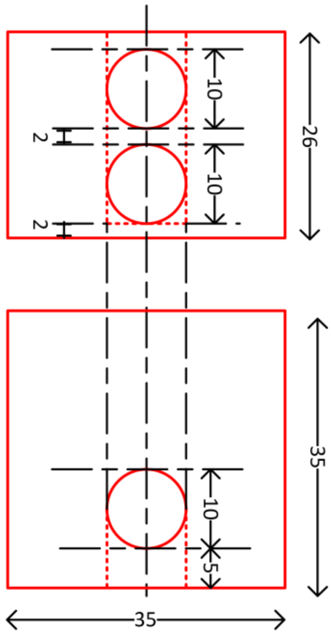

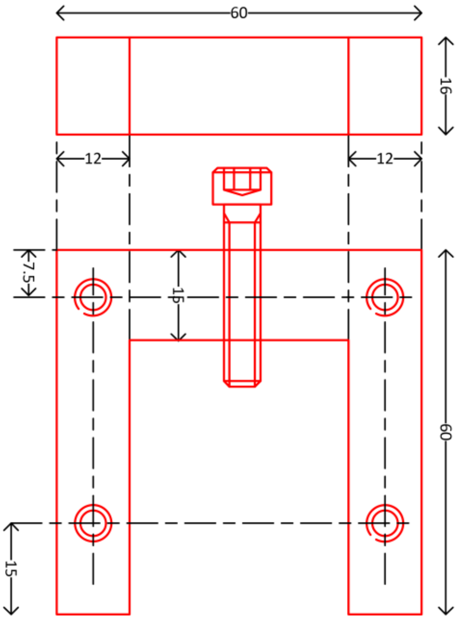

VI. SPR Angle with graphene layers calculated for a BK7 glass at 633 nm in air.

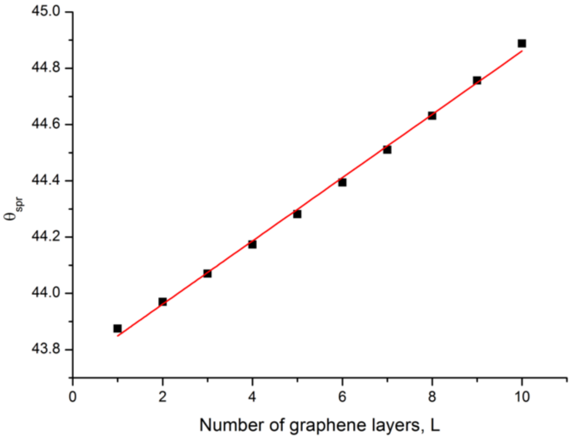

VII. Graphical user interface of the developed hybrid sensor

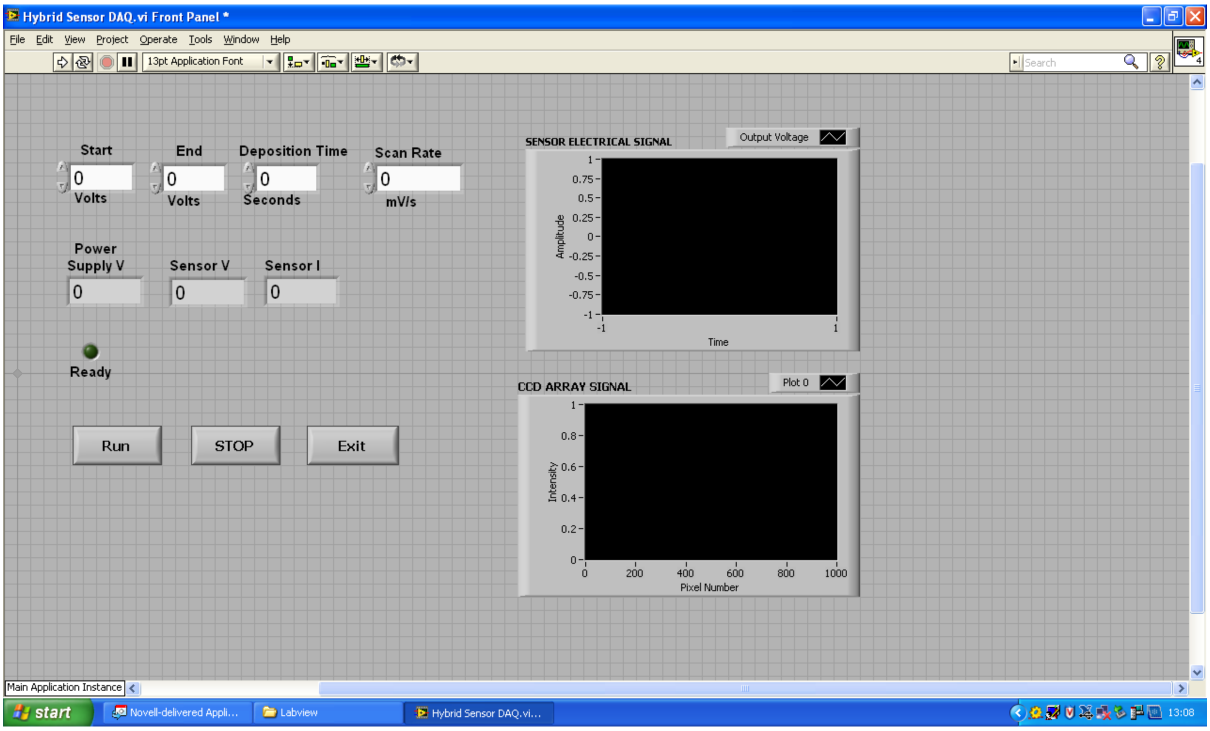

Start 0 Volts

End 0 Volts

Deposition Time 0 Seconds

Scan Rate 0 mV/s

Power Supply V 0

Sensor V 0

Sensor I 0